博士論文

Study on control of electrode / electrolyte interfaces in Li-metal secondary batteries

（金属リチウム二次電池における電極 - 電解質界面制御に関する研究）

越川　裕幸

Hiroyuki Koshikawa

Miyayama Laboratory

Department of Applied Chemistry

Graduate School of Engineering, The University of Tokyo

Contents

Chapter 1

General Introduction

1.1. Energy storage devices in modern society

The demand for energy, especially electrical energy, is considerably growing from the latter half of the 20th century. The wide spread of electric devices with higher performance has been enabled by the appearance of the state-of-the-art energy storage devices. Li-ion batteries, which was commercialized in 1991 by Sony, have dominantly contributed the improvement of our quality of life for the last few decades. In recent years, the fear of global warming and air pollution have accelerated the electrification of vehicles such as electric vehicles and plug-in hybrid vehicles. For the commercialization of these next generation vehicles, batteries with the gravimetric and volumetric energy density higher than 700 Wh/kg are required. However, these values exceed the theoretical upper limit of the energy density of Li-ion batteries, and thus new types of batteries based on different operating principles are highly desired. Li metal secondary batteries in which Li metal is employed as a negative electrode material constitute the major part of these batteries due to their extremely high theoretical energy densities. Nevertheless, safety issues originated from the degradation of Li metal/electrolyte interfaces have hindered their commercialization. Therefore, the control of the interfaces is the core technology indispensable for the development of the next-generation secondary batteries.

1.2. Li-metal secondary batteries

Li metal is one of the promising negative electrode materials composing next-generation secondary batteries due to its high theoretical specific capacity (3860 mAh/g) and the lowest electrochemical potential (-3.04 V vs. standard hydrogen electrode) [1]. Secondary batteries employing Li metal are categorized as Li-metal secondary batteries, and they are largely divided into four: aprotic Li-air batteries, hybrid-type Li-air batteries, Li-sulfur batteries and all-solid-state Li-metal batteries. In this section, the operational principles and the current status of Li-air batteries and all-solid-state Li-metal batteries, which are main concerns in this thesis, were described.

1.2.1. Aprotic Li-air batteries

Li-air batteries exhibited the highest theoretical specific energy density (~3500 Wh/kg) among various types of next-generation batteries, whose concept was first proposed by Abraham in 1996 [2]. Li metal and porous carbon are respectively employed as a negative and a positive electrode. Organic electrolytes such as ethers and sulfoxides are used as Li-ion conducting electrolytes (Fig. 1) [3]. At a negative electrode, Li metal is dissolved into an electrolyte during discharge and deposited on the electrode during charge (eq. 1). At a positive electrode, Li ions in an electrolyte react with O_2 and form Li_2O_2 or Li_2O deposits on a positive electrode during discharge, and then the deposits are decomposed into Li ions and O_2 gas again during charge (eq. 2). Thus total reactions are described as shown in eq. 3.

Reaction at a negative electrode:

$$Li \rightleftharpoons Li^+ + e^- \quad \text{(eq. 1)}$$

Reactions at a positive electrode:

$$2Li^+ + O_2 + 2e^- \rightleftharpoons Li_2O_2 \quad \text{(eq. 2a)}$$

$$4Li^+ + O_2 + 4e^- \rightleftharpoons 2Li_2O \qquad \text{(eq. 2b)}$$

Total reactions:

$$2Li + O_2 \rightleftharpoons Li_2O_2, \qquad E = 2.96\ V \qquad \text{(eq. 3a)}$$

$$4Li + O_2 \rightleftharpoons 2Li_2O, \qquad E = 2.91\ V \qquad \text{(eq. 3b)}$$

Although the theoretical specific energy of the Li-air battery operated based on eq. 3b is larger than that based on eq. 3a (5200 Wh/kg vs. 3505 Wh/kg), the two-electron discharge-charge reaction is preferable in terms of charge-discharge reversibility.

There are several problems to be solved for the practical application of aprotic Li-air batteries, such as low round trip energy efficiency (< 70% vs. > 95% for Li-ion batteries), limited current density (0.1 ~ 1 mA/cm^2 vs. ~ 30 mA/cm^2 for Li-ion batteries) and limited cycle life (< 100 cycles vs. ~ 5000 cycles for Li-ion batteries) [4]. These problems are originated from the fundamental (electro)chemistries proceeded at both a negative electrode/organic electrolyte interface and a positive electrode/organic electrolyte interface. Therefore, the elaborate design of these interfaces are needed for the commercialization of aprotic Li-air batteries.

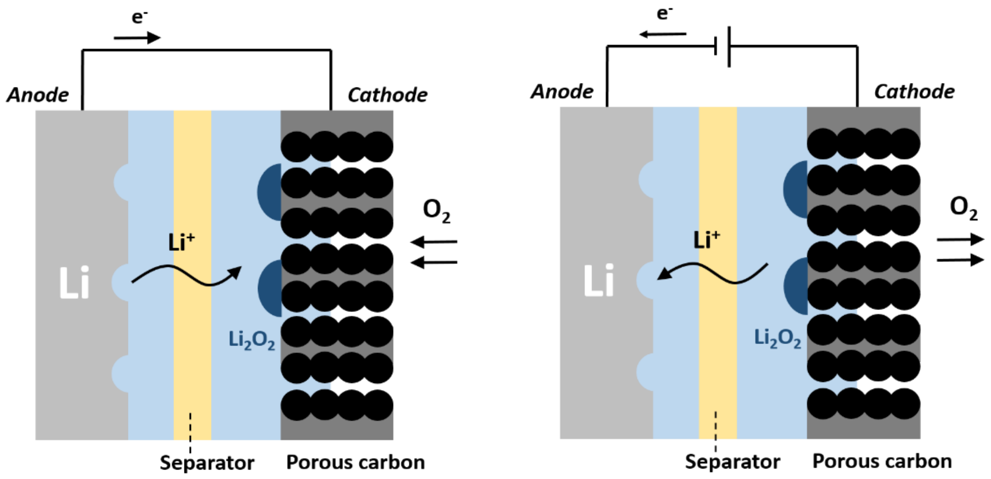

Fig. 1. Schematic illustrations of aprotic Li-air batteries during discharge (left) and charge (right).

1.2.2. Hybrid-type Li-air batteries

The concept of hybrid-type Li-air batteries was first proposed by PolyPlus Battery Company in 2007 and then the cycle test under the realistic conditions was conducted by Zhou's group in 2010 [5-7]. Li deposition-dissolution reactions at a negative electrode proceed in conventional organic electrolytes, whereas O_2 reduction-evolution reactions at a positive electrode proceed in aqueous electrolytes. Two types of electrolyte are separated by a ceramic lithium superionic conductor, LISICON- or garnet-type materials, which is stable against H_2O and prevent the diffusion of air contaminants to a Li metal anode (Fig. 2). The reaction proceeded at a positive electrode and thus the total reaction are different compared to that in conventional aprotic Li-air batteries as follows:

Reactions at a positive electrode:

$$O_2 + 2H_2O + 4e^- \rightleftharpoons 4OH^- \quad \text{(in basic solutions) (eq. 4a)}$$

$$O_2 + 4H+ + 4e^- \rightleftharpoons 2H_2O \quad \text{(in acidic solutions) (eq. 4b)}$$

Total reaction:

$$4Li + O_2 + 2H_2O \rightleftharpoons 4LiOH \quad \text{(eq. 5)}$$

Advanced hybrid-type batteries which do not use organic electrolyte as anolyte have been also proposed to suppress the consumption of Li metal through the reactions with electrolyte and Li dendritic growth [8]. In this case, solid-state Li^+ conductors or polymer electrolytes can be candidate materials as the anolyte directly contacting with Li metal (Fig. 3). The use of polymer electrolytes is beneficial to improve the mechanical stability owning to its flexibility, but several problems exist in view of Li^+ conductivity, stability against Li metal and mechanical strength [9-13]. Related studies will be described in detail in 1.4.1.3.. As solid-state Li^+ conductors for this purpose, garnet-type $Li_7La_3Zr_2O_{12}$ (LLZ) can be listed due to their compatibility with Li metal [14]. Relevant studies will be described in detail in 1.4.3..

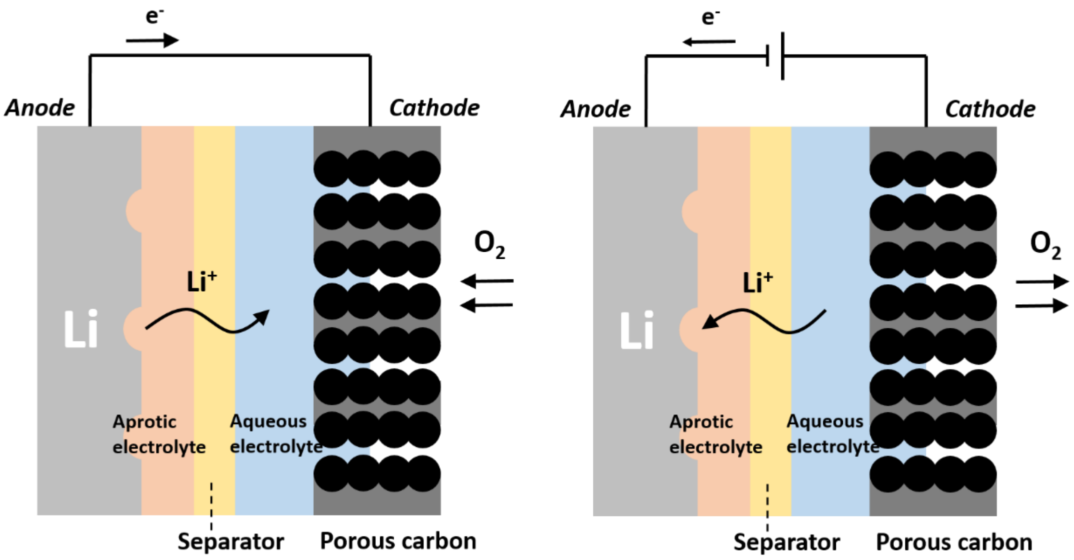

Fig. 2. Schematic illustrations of hybrid-type Li-air batteries during discharge (left) and charge (right).

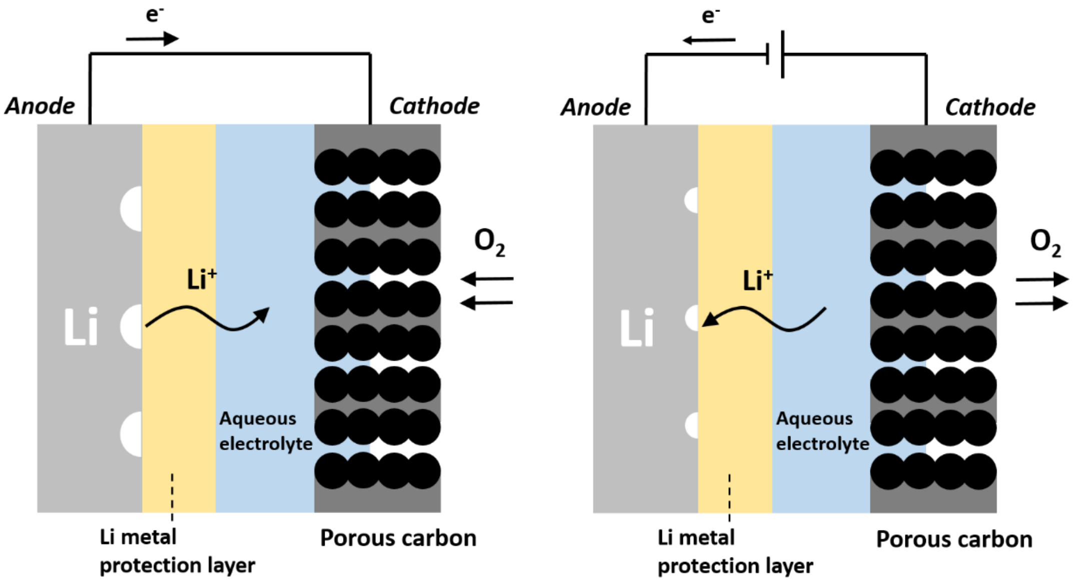

Fig. 3. Schematic illustrations of advanced hybrid-type Li-air batteries during discharge (left) and charge (right).

1.2.3. All-solid-state Li-metal batteries

All-solid-state batteries that use solid electrolytes instead of liquid ones have attracted much attention in terms of safety because they are more stable at elevated temperature and less combustible compared to organic electrolytes [15-17]. Besides, they can offer higher energy density than that of conventional Li-ion batteries by utilizing high-capacity anodes, high-voltage cathodes or making a bipolar stack of cells [15-17]. The schematic illustration of the configuration of the batteries are shown in Fig. 4. A successful integration of a Li metal electrode would offer an increase of up to 70% in energy density [17]. Solid electrolytes are divided into two categories: oxide-type electrolytes and sulfide-type ones [15-17]. The former are generally more air-stable and stiff but, at the same time, brittle, causing mechanical failure through cracking. In contrast, the latter are more ductile and easily form dense electrode composites but suffer from low atmospheric stability. Recent development of sulfides and thiophosphates which exhibit comparable or even higher Li-ion conductivity than organic electrolytes (in the order of 10^{-2} S/cm) has accelerated the commercialization of all-solid-state batteries [18, 19]. Although oxide-type solid electrolytes generally exhibit lower Li-ion conductivity than sulfide-type ones, their commercialization should be also prompted due to their thermodynamic stability especially for the use of Li metal.

Also, in view of the application of Li metal secondary batteries, the use of solid electrolytes is a potential solution to the issues inherent in Li metal such as the consumption of Li metal by side reactions and the short-circuit by the growth of Li dendrites. Among various kinds of solid electrolytes, garnet-type $Li_7La_3Zr_2O_{12}$ (LLZ) is promising in terms of Li-ion conductivity, chemical stability against Li metal and stiffness [15-17, 20-26]. However, it is known that the resistance of the Li/LLZ interface is high because of the nature of solid-solid interfaces is less dynamic relative to that of solid-liquid interfaces, which interferes with the operation of a LLZ-based solid-state battery at a practical rate [15, 16, 23, 25]. Therefore, understanding the fundamental science of Li deposition-dissolution reactions proceeding at the Li/LLZ interface is very important, and this topic will be explained in detail in 1.3.3..

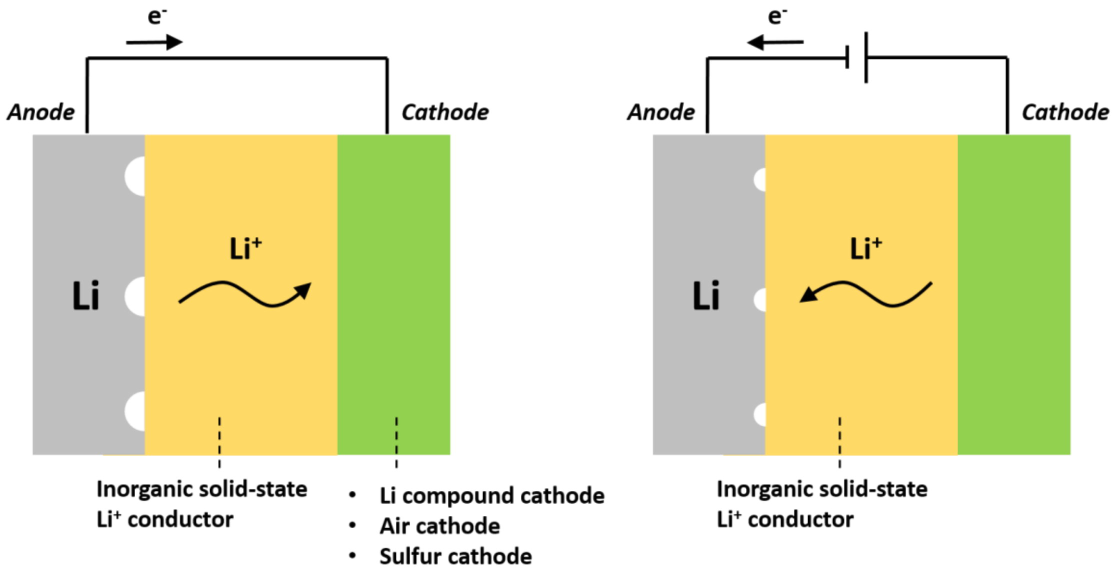

Fig. 4. Schematic illustrations of all-solid-state Li metal batteries during discharge (left) and charge (right).

1.3. Fundamental science at electrode / electrolyte interfaces

There are several problems to be overcome for the real application of Li-metal secondary batteries, and three critical problems inherent in the properties of a Li metal electrode are listed [1]: (1) the low coulombic efficiency (CE) of Li deposition-dissolution reactions, (2) the increase in the charge transfer resistance at Li metal / electrolyte interfaces during repeated cycles, (3) the growth of Li dendrites (Fig. 5). The origin of each problem and how these problems are correlated and cause the cell failure depend on the physicochemical properties of electrode / electrolyte interfaces. In this section, fundamental science at each type of the interface will be explained.

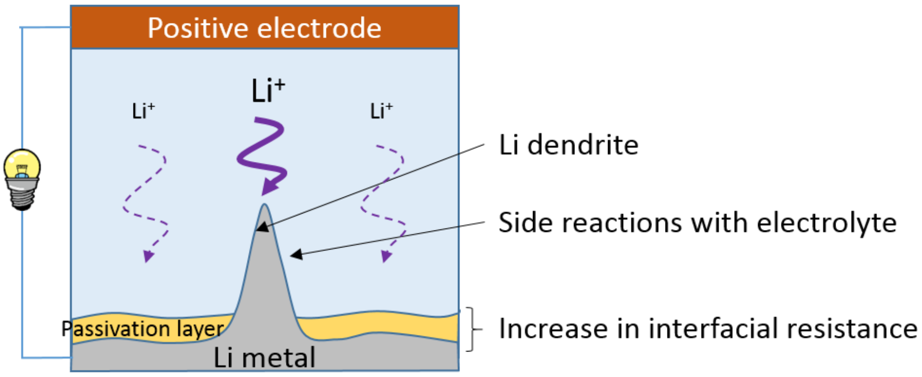

Fig. 5. Problems inherent in a Li metal electrode

1.3.1. Li metal / liquid electrolyte interfaces

As Li metal is highly reactive with almost all of the compounds constituting liquid electrolyte, Li metal is covered by a surface layer which is instantly formed by the reaction of Li metal with the electrolyte [27, 28]. This layer which has the properties of a solid electrolyte was called as solid electrolyte interphase (SEI) by Peled in 1979 [28]. The properties of SEI such as ionic conductivity, electronic conductivity, cationic transport number, density and thickness critically determine the CE of Li deposition-dissolution reactions, the charge transfer resistance at the interfaces and the occurrence of Li dendritic growth. The ionic conductivity of pure solid crystals is generally very low at room temperature; thus the migration of ions through SEI become the rate-determining step. SEI also continues to grow during repeated cycling by the reductive decomposition of anions and solvents in the electrolyte. The former is caused by the migration of electrolyte anions through the SEI which has the cationic transfer number less than unity. The latter is originated from the inhomogeneity of SEI, i.e., the SEI contains cathodic areas in which electrons migrate through the SEI and reduce the solvent. The grain size of Li deposits also significantly affects the degree of SEI growth and hence the CE [29, 30]. Since the passivation of

SEI is not completely hermetic, the SEI massively grows above the Li deposits with smaller grain size, which has larger available surface area the reactions between Li and electrolyte. The inhomogeneity of SEI also induces a non-uniform current distribution of Li deposition-dissolution [27, 31]. Since the SEI in the vicinity of a Li metal electrode is mainly composed of inorganic Li salts, their cohesion and flexibility is very limited. Hence, the SEI cannot properly accommodate the morphological changes of Li metal upon Li deposition-dissolution. The SEI is broken and then both Li dendritic growth and the additional consumption of Li metal and electrolyte are induced, resulting in the cell failure (Fig. 6).

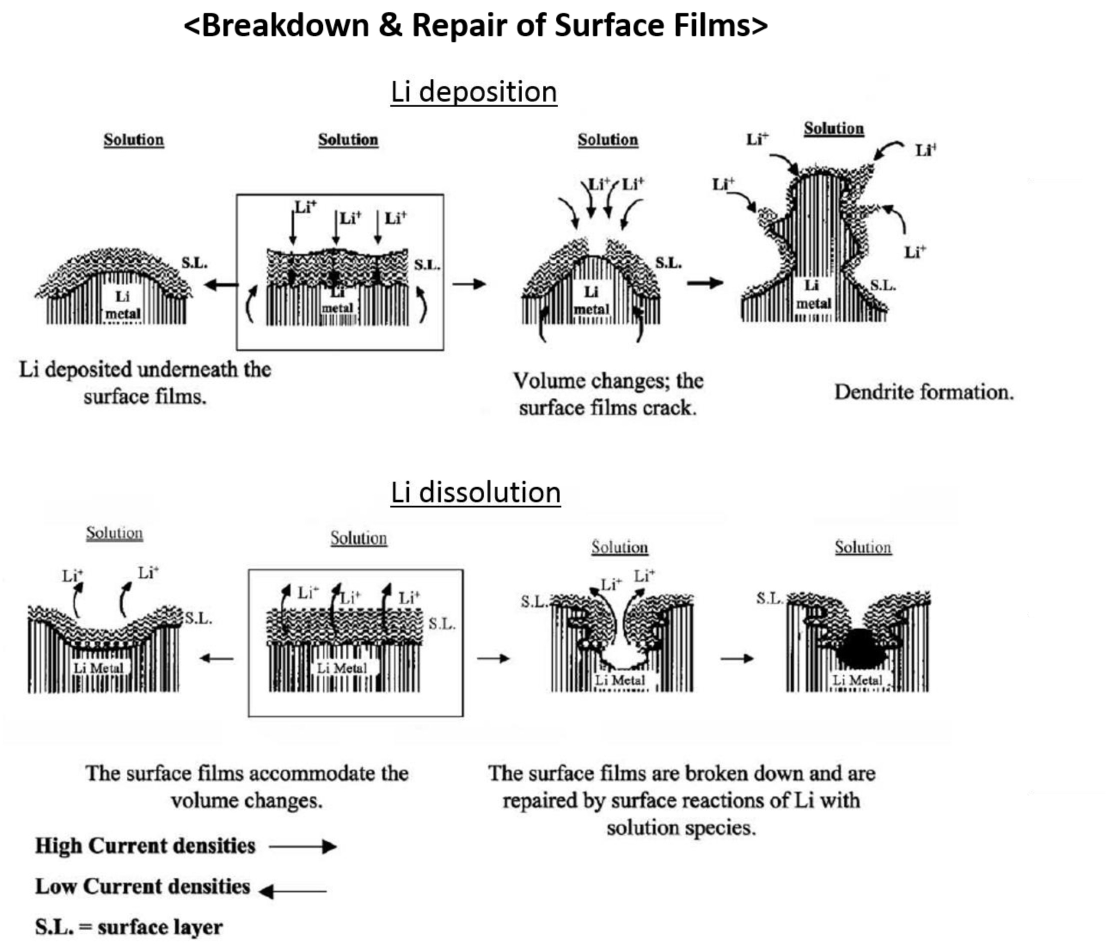

Fig. 6. Schematic illustration of the morphology and failure mechanisms of a Li metal electrode during Li deposition-dissolution reactions (Adapted by permission from ref. 27. Copyright 2002, Elsevier).

The distribution of Li ions in the vicinity of an electrode as well as the properties of SEI should be paid attention to understand and effectively control Li deposition-dissolution reactions. Brissot and Chazalviel *et al.*, described the concentration gradient in a symmetrical Li/PEO/Li cell with a small interelectrode distance (L) as follows [32, 33]:

$$\frac{\partial C(x)}{\partial x} = \frac{J\mu_a}{eD(\mu_a + \mu_{Li+})} \quad \text{(eq. 6)}$$

where C is the concentration of Li^+, J is the effective current density, D is the ambipolar diffusion coefficient, e is the electronic charge, μ_a and μ_{Li+} are the anionic and Li^+ mobilities. If the concentration gradient across the electrolyte is larger than twice the value of the initial Li^+ concentration (C_0) divided by the interelectrode distance (L) ($dC/dx > 2C_0/L$), Li^+ concentration goes to zero at the negative electrode at a time called "Sand's time" τ, which is defined as follows:

$$\tau = \pi D\left(\frac{eC_0}{2Jt_a}\right)^2 \quad \text{(eq. 7)}$$

where t_a is the anionic transfer number. The depletion of Li^+ will result in a local space charge, leading to the nucleation and growth of Li dendrites. dC/dx is proportional to J according to eq. 6, the dendrites grow above the certain current density (i.e., limiting current density) in theory. However, the dendrite growth was indeed observed even when the applied current density was less than the limiting current density, which is due to the local inhomogeneity of the Li/polymer electrolyte interface [33-35]. Although the models described in this paragraph was originally constructed at Li/polymer electrolytes interfaces, they have also been successfully applied to various Li/liquid electrolyte interfaces [36-38].

Several attempts have been made to understand Li deposition-dissolution reactions proceeded at Li metal/liquid electrolyte interfaces in terms of mechanical properties. Yamaki *et al.*, proposed that the morphology of Li deposits (whiskers vs. particles) is determined by the balance between the creep strength of lithium (0.4 MPa) and the internal pressure caused by the surface tension of the protective film [39]. Approaches to control Li deposition-dissolution reactions by the insertion of mechanical block layers were also described in 1.4.1.2..

Considerable amount of knowledge about the Li deposition-dissolution reactions proceeded at Li/liquid electrolyte interfaces has been thus accumulated, which has helped the development of approaches to control the reactions as mentioned in the part 1.4.1.. However, contaminants often induce unexpected changes in the physicochemical properties of the surface film and hence the cycle performance. The influence of contaminants is especially serious in an open cell system like Li-air batteries. Therefore, the effect of contaminants such as H_2O and CO_2 at the Li/liquid electrolyte interfaces is also an important topic. The surface species formed on Li metal in the commonly used non-aqueous solutions are highly hygroscopic, and thereby, water from the solution phase penetrates the surface films, hydrates the surface species, thus diffusing towards the active metal [31]. Thus Li metal should be effectively protected from the attack of contaminants. Togasaki *et al*., reported that the CE remained to be around 85% with increasing H_2O content up to 1000 ppm in a DMSO-based electrolyte when the protective SEI mainly composed of inorganic compounds such as Li_2CO_3, Li_2O and LiF was formed before cycles (Shear modulus: several tens of GPa for inorganic compounds vs. < 1 GPa for organic compounds) (Fig. 7) [40]. Aurbach's group found that Li_2CO_3 formed by the reaction of Li metal with CO_2 decreases the interfacial resistance and increases the cycling efficiency of a Li metal anode (Fig. 8), which is because the less hygroscopic Li_2CO_3 can effectively passivate Li metal in solution [41-43]. However, it is also noteworthy that no simple correlation between the Li anode's performance and its interfacial resistance was observed in their extensive studies [41, 42].

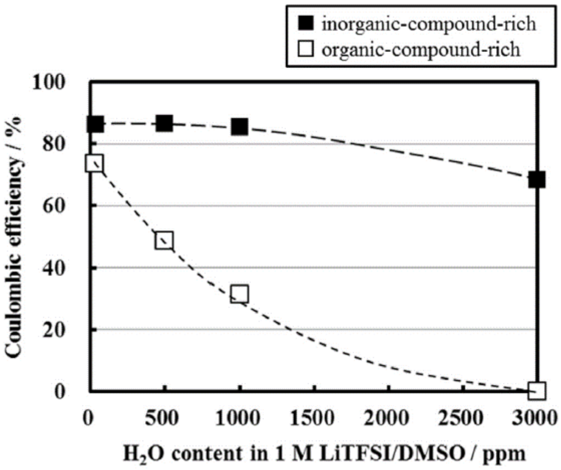

Fig. 7. Dependence of the coulombic efficiency of Li deposition-dissolution reactions on the H_2O concentration in 1 M LiTFSI-DMSO electrolyte. Black and white dots respectively indicate the results obtained when Li metal deposited in 1 M $LiClO_4$-EC/DEC electrolyte with CO_2 bubbling for 3 h and without CO_2 bubbling was used for the cycle tests (Reprinted by permission from ref. 40. Copyright 2015, Elsevier).

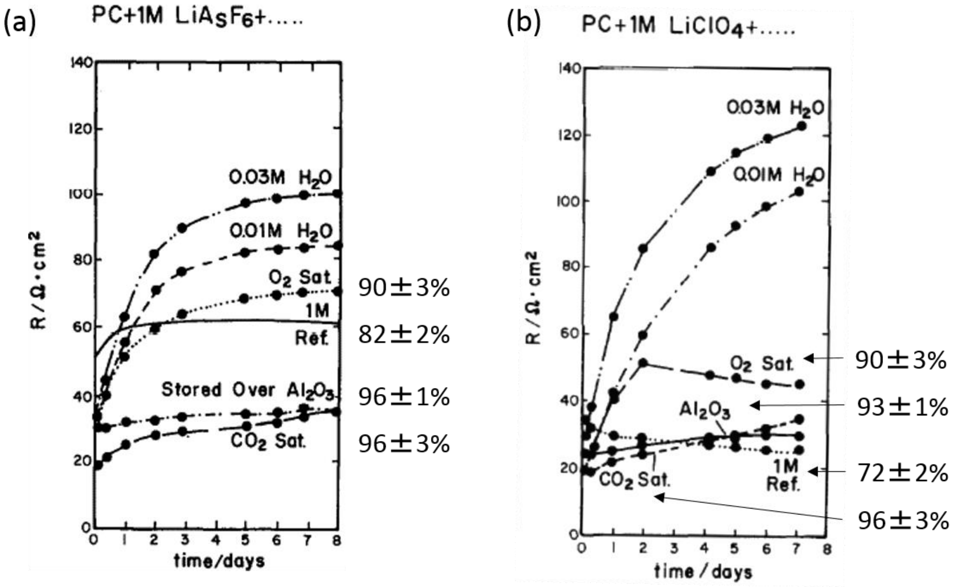

Fig. 8. Li/electrolyte interfacial resistance as a function of storage time obtained when additives or dissolved gas were present in (a) 1 M $LiAsF_6$-PC and (b) 1 M $LiClO_4$-PC based electrolytes. Coulombic efficiency of Li deposition-dissolution reactions obtained for each electrolyte was also shown (Adapted by permission from ref. 42. Copyright 1993, Elsevier).

1.3.2. Air cathode / liquid electrolyte interfaces

There have been plenty of research regarding the influence of the choice of solvents and lithium salts on the performance of an air cathode [44]. Herein, the modulation of the reaction pathway at an air cathode/organic electrolyte interface in the presence of additives were described in detail. Aetukuri *et al.*, discovered that trace amount of electrolyte additives enhances the formation of Li_2O_2 toroids and results in significant improvements in discharge capacity. They show that additives with high donor number or acceptor number which favorably coordinate to Li^+ or O_2^- of a LiO_2 intermediate prompt a solution-based Li_2O_2 formation pathway [45]. The Li_2O_2 formation by a surface electrochemical route and by a solution-mediated route is schematically summarized in Fig. 9.

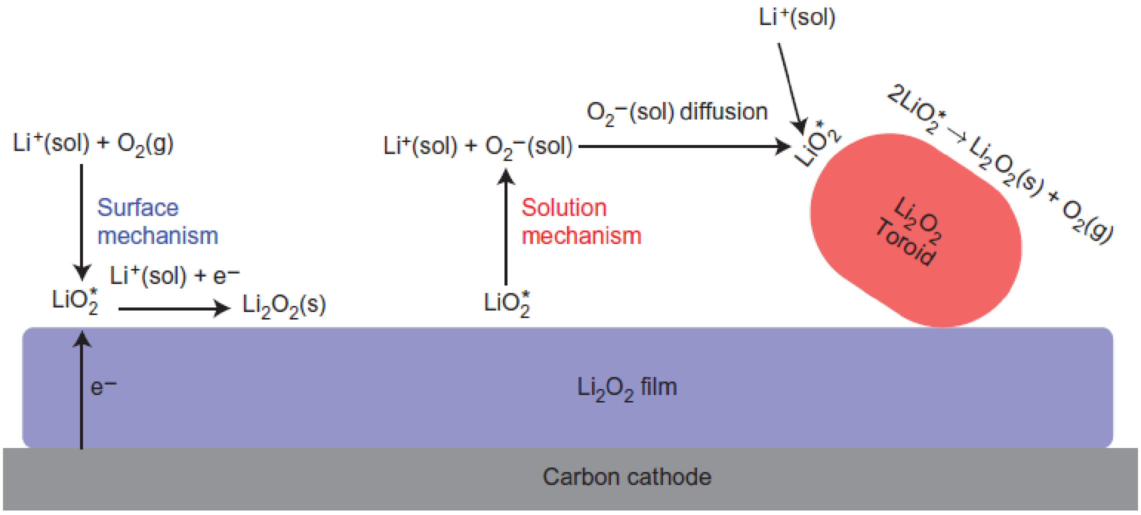

Fig. 9. Two distinct mechanisms, a surface electrochemical route vs. a solution-mediated route, of the growth of Li_2O_2 deposits (Reprinted by permission from ref. 45. Copyright 2015, Nature).

The influence of H_2O contaminated from open air on the reactions proceeded at a cathode / liquid electrolyte interface has been also extensively investigated. Several studies observed the detrimental effects of H_2O on the performance of Li-air or Li-O_2 batteries [46-48]. In these reports, contaminated water caused the side reactions shown below at both electrodes and with electrolyte, resulting in the shorter cell life.

At a positive electrode:

$$2Li^+ + 2e^- + 2H_2O \rightarrow 2LiOH + H_2 \quad \text{(eq. 8a)}$$

$$2Li^+ + 2e^- + Li_2O_2 + 2H_2O \rightarrow 4LiOH \quad \text{(eq. 8b)}$$

$$2Li_2O_2 + 2H_2O \rightarrow 4LiOH + O_2 \quad \text{(eq. 8c)}$$

$$Li_2O_2 + 2H_2O \rightarrow 2LiOH + H_2O_2 \quad \text{(eq. 8d)}$$

At a negative electrode:

$$Li + H_2O \rightarrow LiOH + 1/2H_2 \quad \text{(eq. 9)}$$

However, whether the reactions on a negative or a positive electrode dominantly cause the cell deterioration is ambiguous. Although Wang *et al*., demonstrated that the performance degradation of the cells operated in open air is mainly due to the deactivation of a cathode [46], this type of knowledge, especially quantitative one, is still limited. Schwenke *et al*., investigated the effects of H_2O and protons in an electrolyte on the battery discharge-charge behavior [49]. Although the discharge capacity was increased associated with the formation of toroidal Li_2O_2 crystal in the presence of H_2O and protons, their existence has detrimental influence on the battery performance. Protons are consumed via a reaction: $O_2 + e^- + H^+ \rightarrow HOO^\cdot$, in the beginning of discharge, which leads to the generation of a variety of reactive oxygen species (H_2O_2 and $HO^\cdot$) and thus side reactions with electrolyte and already formed Li_2O_2, resulting in the cell degradation. H_2O might get oxidized to protons during charge, promoting the solubilization of Li_2O_2 according to a reaction: $2H^+ + Li_2O_2 \rightarrow H_2O_2 + 2Li^+$. Protons indeed must have a much stronger influence on discharge capacity and charging behavior compared to H_2O.

The beneficial effects of H_2O on the performance of Li-air or Li-O_2 batteries have been also reported [45, 49-52]. Aetukuri *et al.*, reported that the discharge capacity was extended with increasing the amount of H_2O by inducing a solution-based Li_2O_2 formation pathway (Fig. 9) [45]. However, the charge overpotential increased in the presence of H_2O due to the increased formation of parasitic discharge products. H_2O raised the concentration of O_2- in solution by coordinating with O_2-, and the generated O_2- reacts with electrolyte, discharge products and carbon substrate to form various parasitic products. In contrast, Qiao *et al.*, discovered that the H_2O effectively suppresses the side reactions proceeded on a carbon-based cathode and with organic electrolyte via the attack of superoxide radical [50]. The fundamental reaction pathway of an aprotic Li-O_2 battery can be altered by the formation of hydroperoxide ($O_2 + H_2O + 2e^- \rightarrow HO_2^- + OH^-$ / $E_0 = 2.975$ V (vs. Li/Li$^+$), $\Delta G = 12$ kJ/mol) as the discharge intermediate (Fig. 10a). Moreover, H_2O also triggers Li_2O_2 formation in a solution-based pathway, reducing the voltage hysteresis (Fig. 10b). The reason why the Qiao's study [50] and the Aetukuri's study [45] reported the different charge performance might be derived from the difference in the examined H_2O concentration range (0.5-30% vs. < 0.4%). Considering the theoretical explanation by Aetukuri *et al.* [45], the rate of two competitive reactions, the solvation of O_2^- by H_2O and the H_2O-induced disproportionation of O_2^- into HO_2^- and OH^-, are dependent on H_2O concentration. The increase in the rate of the former reaction is saturated over several thousands of ppm of H_2O in dimethoxyethane (DME)-based electrolytes, whereas the rate of the latter reaction exhibits no saturation behavior at the higher H_2O concentration. With regard to the species of the discharge product, LiOH was also obtained as the main product in the presence of specific electrocatalysts by the conversion of reaction intermediates, and it was reoxidized ($LiOH \rightarrow Li + 1/4O_2 +$

$1/2H_2O$, $E = 3.32\ V + 0.059 \times 1/2 \log[H_2O]$) around 3.0~3.2 V (vs. Li/Li^+) by employing effective LiOH oxidation catalysts [50-52] (Fig. 11).

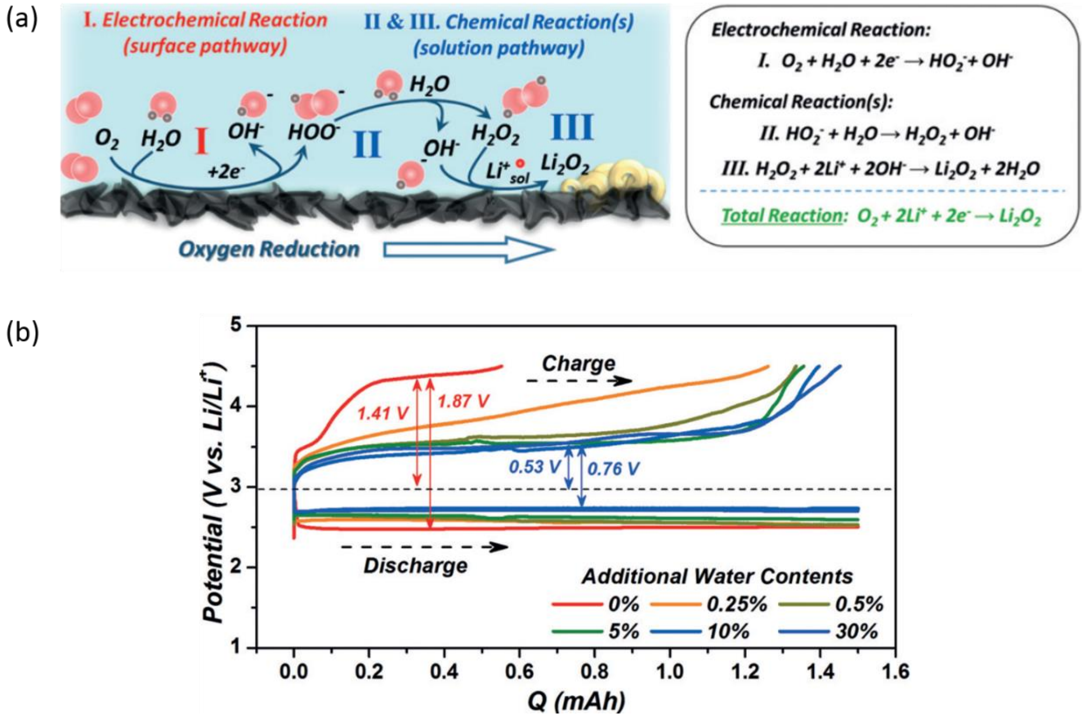

Fig. 10. (a) Schematic illustration of the reaction pathway during discharge in 1 M LiTFSI-TEGDME with additional H_2O. (b) Voltage profiles of $Li\text{-}O_2$ cells using 1 M LiTFSI-TEGDME containing different concentration of H_2O as electrolytes (Reprinted by permission from ref. 50. Copyright 2017, Wiley).

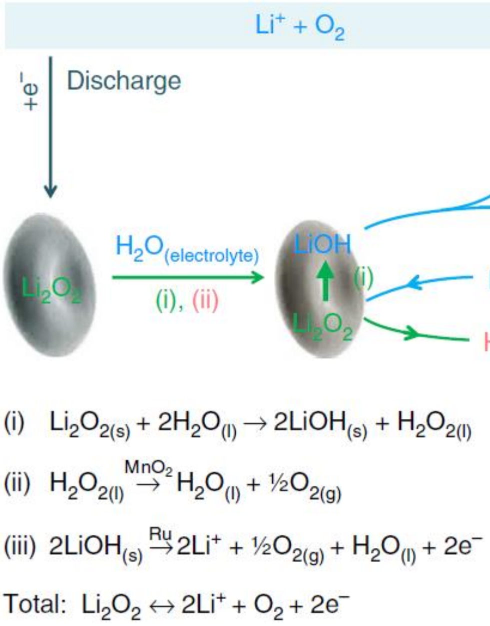

Fig. 11. Schematic illustration of the reaction pathway in 0.5 M $LiClO_4$-DMSO containing optimized amount of H_2O. (i) is a spontaneous process. (ii) is promoted over MnO_2 nanoparticles electrocatalyst. LiOH oxidation in (iii) occurs at lower charge overpotential over Ru nanoparticles electrocatalyst (Reprinted by permission from ref. 52. Copyright 2015, Creative Commons).

The beneficial effects of contaminant H_2O on an air cathode mentioned above were observed in the presence of Li^+ conductive glass ceramic as a Li metal protective layer [49, 50] or by the use of less reactive $LiFePO_4$ as an anode [52]. Thus the knowledge of the influence of H_2O on Li deposition-dissolution reactions at an anode is also required to design Li-air batteries. It should be noted that the effects of H_2O and protons mentioned above were investigated mainly in ether-based electrolytes, which are the higher stability with both a Li metal anode and an air cathode [53-56]. As described in the previous section, the effects of H_2O on the reactions at a Li metal anode were quantitatively examined in carbonate- or DMSO-based electrolytes [40, 57].

However, the reaction mechanism can be altered in electrolytes using different solvents [58]. Therefore, the quantitative knowledge of Li deposition-dissolution reactions on a Li metal anode in ether-based electrolytes are worth investigating.

1.3.3. Li metal / solid electrolyte interfaces

For increasing the energy density of all-solid-state batteries high enough to replace the state-of-the-art Li-ion batteries, the thickness of solid electrolytes has to be reduced, e.g. only 100 μm-thickness for increasing the energy density comparable to that of the Li-ion batteries for EV applications [16]. Considering also the recent discovery of the solid electrolytes with Li-ion conductivity comparable to that of organic electrolytes, the properties of electrode/solid electrolyte interfaces will be increasingly decisive for the cell performance [15, 16]. When Li metal is used as an anode, it is an essential requirement to employ solid electrolytes with high stability against Li metal. However, most of the solid electrolytes are thermodynamically unstable with Li metal [59-61]. Thus, to date, higher-potential anodes such as $Li_4Ti_5O_{12}$ or Li-In are used in batteries with these solid electrolytes. In contrast, garnet-type $Li_7La_3Zr_2O_{12}$ (LLZ) is known to be stable with Li metal [15, 16, 20-26], and hence, the fundamental science at a Li/LLZ interface was described below.

Despite the several strong points LLZ possesses as a solid electrolyte in Li-metal secondary batteries, high resistance of a Li/LLZ interface (R_{int}) and Li dendritic growth through LLZ are the crucial problems to be solved. Previous studies have revealed that various factors determine R_{int}, including the segregation of impurities (e.g. Li_2CO_3) at the interface [62-64], poor physical contact between Li and LLZ [25, 65-67], and slow interfacial charge transfer [16, 62, 65, 68, 69].

For the first point, LLZ favorably reacts with CO_2 and Li_2CO_3 is formed on the surface of LLZ (the thickness of Li_2CO_3 layer is in the order of several tens of nm). Cheng *et al.*, reported that R_{int} obtained when LLZ was exposed to ambient air and thus Li_2CO_3 was formed was almost an order of magnitude higher than that obtained when LLZ was treated under dry Ar atmosphere [62]. They also demonstrated the cell with LLZ exposed to air short-circuited in much shorter time compared to the cell with LLZ without exposure to air.

Concerning the second point, making intimate contact at Li/solid electrolyte interfaces is generally difficult due to their rigid nature and the interfaces easily lose the contact during repeated cycling, which results in the increase in the charge transfer resistance at the interfaces [25, 66, 65, 67, 70-73]. The detailed picture has been also proposed as follows: Metal vacancies are generated at the interface during metal dissolution, and then these vacancies coalesce into voids if the supply of Li atoms from Li bulk to the interface is not fast enough to fill the generating vacancies (Fig. 12a) [70-73]. The extent of voids formation is larger than expected from the applied current density because metal is actually dissolved at limited points at the effective current density higher than the applied one, which is derived from the surface roughness and crystalline inhomogeneity of solid electrolytes (Fig. 12b) [73]. Furthermore, the concentration of electric field during cycling on decreased contact areas will induce the growth of Li dendrites. This mechanical problem is especially serious when using LLZ, which has relatively higher Young’s modulus (LLZ: 150 GPa vs. sulfide-type: several tens of GPa) [15].

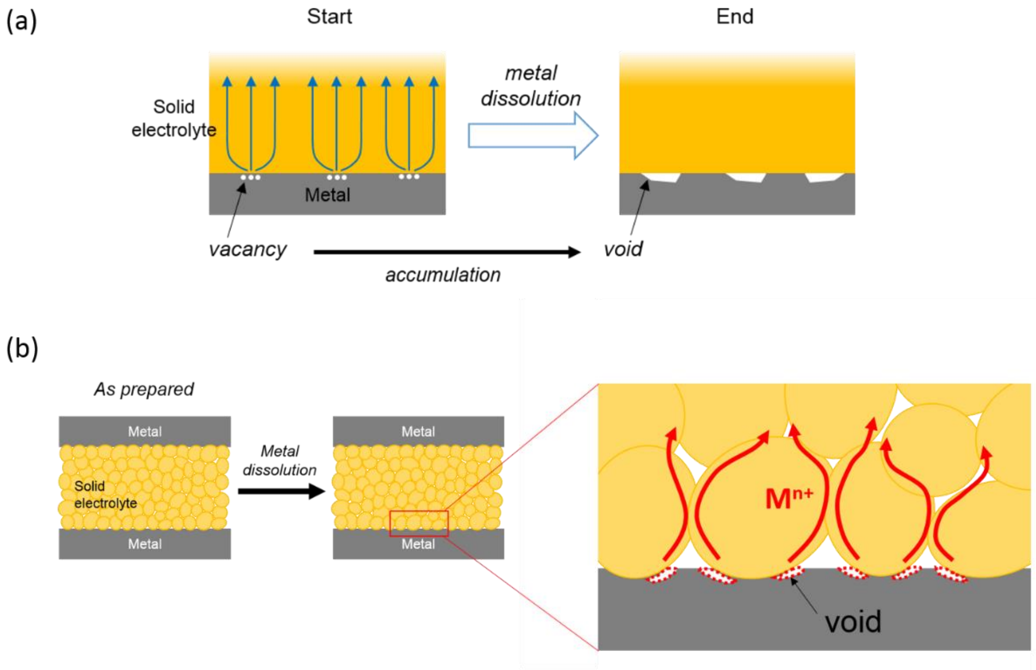

Fig. 12. Schematic illustrations of voids formation at a metal electrode/solid electrolyte interface during metal dissolution in different scales.

The third point is related to the differences in the way that solids and liquids screen the electric fields at the interfaces [16]. In liquid electrolyte filled battery, the double layer and potential drop at each electrode occur both due to concentrating the mobile ions (cations and anions) and due to alignment of solvent dipoles at the surface of electrodes. In contrast, for the typical Li-conductive solid electrolytes, a single conducting species (e.g., Li^+ vacancies) contribute to the double layer and screening of the potential through their accumulation at one electrode and depletion at the other electrode (Fig. 13). As a result, exchange current densities may be inherently smaller and charge-transfer resistances higher than those in conventional Li-ion batteries, even at the ideal Li/solid electrolyte interfaces.

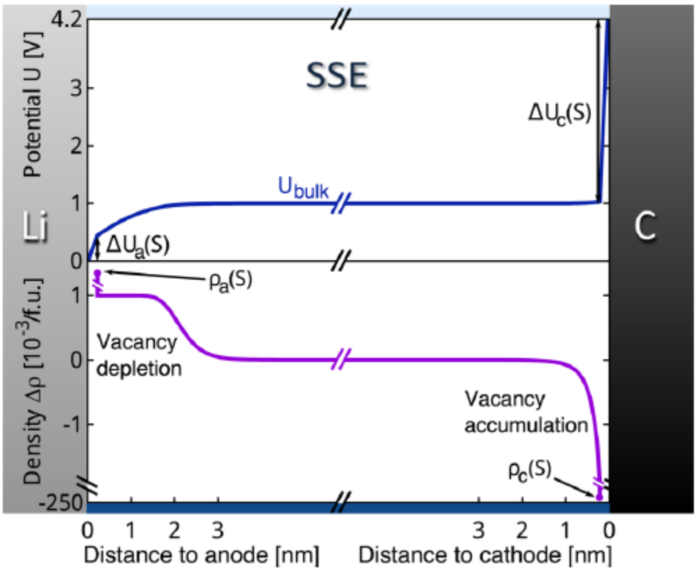

Fig. 13. Schematic illustration of the spatially dependent potential variation *U* (top) and charge distribution $\Delta\rho$ (bottom) in a prototypical Li/solid electrolyte (SSE)/C battery with Li$^+$ vacancies as the mobile species in the SSE (Reprinted by permission from ref. 16. Copyright 2015, American Chemical Society).

Solid electrolytes are expected to prevent the penetration of Li dendrites due to its sufficiently high elastic modulus compared to that of Li metal; however, cell short-circuit occurred even by the use of the solid electrolytes including LLZ. A lot of studies have elucidated that Li dendrites grow inside LLZ along the grain boundaries [74-76] and/or through the propagation of pre-existing interfacial defects [77, 78]. Cheng *et al*., observed that Li metal was preferentially deposited along grain boundaries for the short-circuited LLZ (Fig. 14) [74]. The driving forces of the former mechanism is the lower mechanical strength of grain boundaries and the higher Li$^+$ conductivity along grain boundaries compared to that in the grains. The latter mechanism has been also discussed in terms of the elasticity and toughness of solid electrolytes [77, 78]. Schmidt *et al*., demonstrated that the crack initiation and extension by the growth of Li dendrites occurs inside LLZ prior to complete cell failure by observing the decrease in the stiffness of LLZ in the minutes prior to the failure, making use of *in situ* non-destructive acoustic pulse-echo technique [77]. Porz *et al.*, reported that Li plating penetrates/infiltrates at defects only above a critical current density (Fig. 15) [78]. Importantly, the possibility of Li infiltration is independent of the shear modulus of the solid electrolytes.

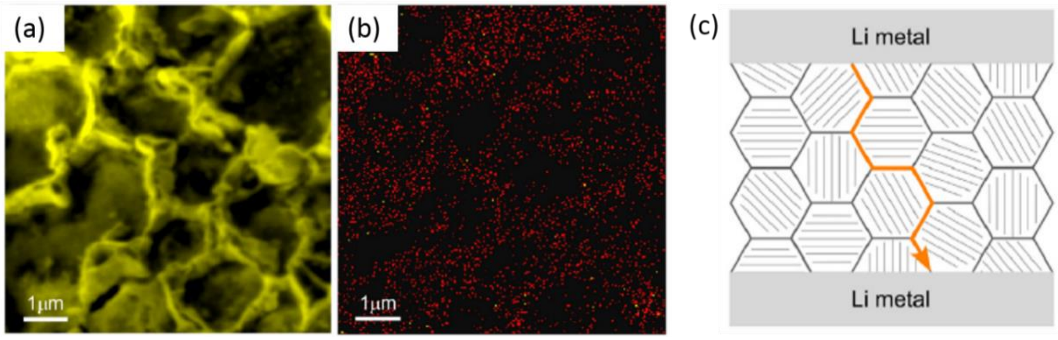

Fig. 14. (a) SEM image and (b) corresponding Li mapping obtained for the auger analysis of grains and grain boundaries. (c) Schematic illustration of Li metal propagation through the grain boundaries of LLZ (Adapted by permission from ref. 74. Copyright 2017, Elsevier).

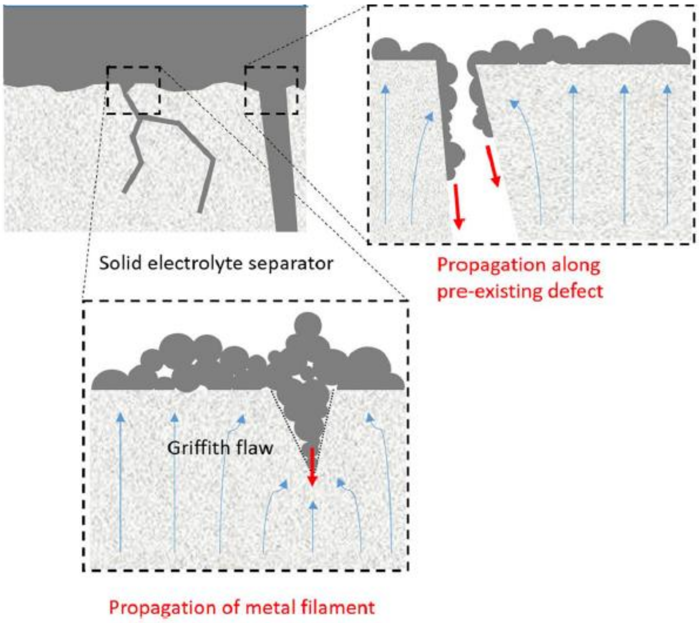

Fig. 15. Schematic illustration of Li metal propagation along pre-existing defects (Adapted by permission from ref. 15. Copyright 2017, Creative Commons).

Several studies have been also conducted to understand the fundamental mechanism of Li deposition-dissolution reactions at electrode/solid electrolyte interfaces [79-83]. Motoyama *et al.*, examined Li deposition-dissolution reactions at metal current collector/LIPON interfaces in view of mechanical properties [79]. It was found that both the Li nucleation overpotential and the achievable Li particle size increased with increasing the Young's modulus of the current collector (Fig. 16a-c). The puncture of a current collector by growing Li nuclei is also effectively suppressed by using a current collector with higher Young's modulus (Fig. 16d). However, LIPON employed in these studies is an amorphous material with no grain boundaries while LLZ is a polycrystalline material with grain boundaries. The mechanism of Li nucleation and growth in LLZ-based systems is assumed to be considerably different. Thus these kinds of fundamental studies have to be conducted more intensively at Li or non-Li current collector/LLZ interfaces as well.

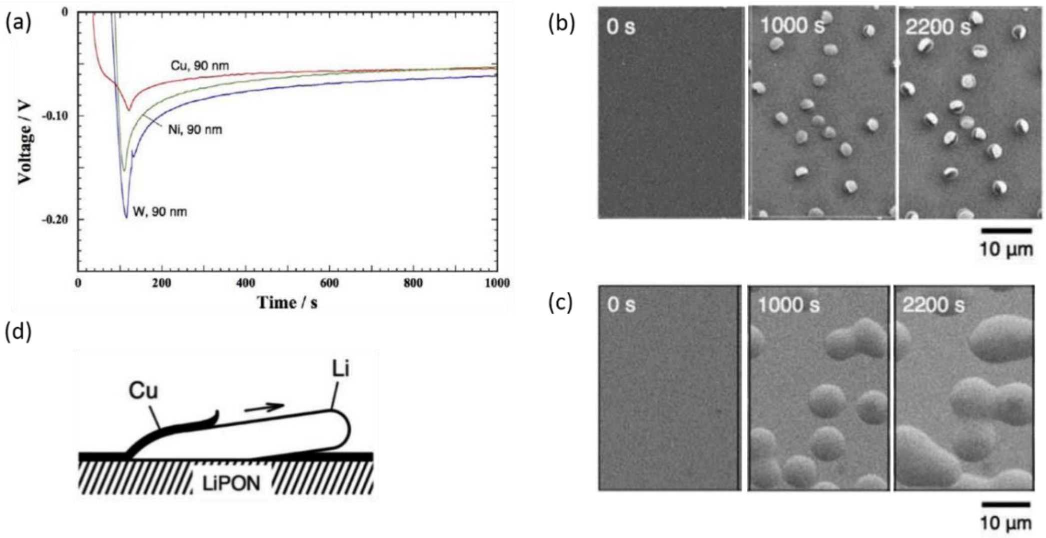

Fig. 16. (a) Voltage transients during Li deposition on Cu, Ni and W current collectors. (b, c) SEM images of Cu (Young's modulus: 130 GPa) and W (Young's modulus: 411 GPa) current collectors during Li deposition. (d) schematic illustration of the puncture of Cu current collector by the growth of a Li rod (Adapted by permission from ref. 79. Copyright 2015, Electrochemical Society).

1.4. Approaches for controlling of electrode / electrolyte interfaces

Since the physicochemical properties of electrode / electrolyte interfaces are different among various types of battery systems, approaches to control the reactions proceeded at these interfaces should be also varied based on their properties. In this section, several approaches which have been adopted during the last 40 years will be described for each type of the interface.

1.4.1. Li metal / liquid electrolyte interfaces

1.4.1.1. Optimization of electrolyte components and SEI formation additives

As described in the previous section, the physicochemical properties of SEI critically determine the performance of Li-metal secondary batteries employing liquid electrolyte. The elasticity is one of the important properties because it determines the resistance of SEI against Li penetration and the ability of SEI to accommodate the volume change of Li metal during cycling. Monroe *et al.*, proposed that materials with roughly twice the shear modulus of lithium can suppress Li dendrites at Li/solid polymer interfaces [84]. This knowledge has been extensively applied to various types of Li/electrolyte interfaces, and much effort has been made to improve the mechanical stability of SEI through the optimization of electrolyte components and SEI formation additives. For example, Aurbach *et al.*, reported that the SEI containing elastomers formed in 1, 3-dioxolane solvent with $LiAsF_6$ as a salt and tributylamine as a stabilizer enabled the reversible Li deposition-dissolution over 100 cycles [27, 31, 85, 86].

Contaminants from air such as H_2O and CO_2 can also work as functional additives for Li deposition-dissolution reactions. Togasaki *et al.*, reported the CE reached a maximum of 88.9% by increasing the H_2O content up to 35 ppm in CO_2-dissolved 1 M $LiPF_6$-EC/DEC [57]. Qian *et al.*, discovered that dendrite-free Li metal deposition could be achieved by adding a controlled amount of H_2O (25~50 ppm) in $LiPF_6$-based electrolytes [87]. Osaka *et al.*, observed the decrease in the interfacial resistance and superior cyclability in the presence of dissolved CO_2 in PC-based electrolytes, which coincides with the results obtained in Aurbach's group [88-90]. These studies indicate the importance of the formation of thin (in the order of tens of nm) and highly elastic SEI (> tens of GPa in Young's modulus or shear modulus), which enables faster Li^+ transport and suppresses the further reaction of Li metal with electrolyte at the same time.

1.4.1.2. Introduction of artificial protective layer

Covering Li metal with an ex situ-formed protective layer before conducting cycles is another approach to control Li deposition-dissolution reactions. Umeda *et al.*, reported that the formation of silica films on Li metal by immersing Li in tetraethoxysilane enabled stable plating and stripping of Li for 100 cycles without significant growth of Li dendrites and notable change in the cell impedance [91]. Interestingly, the periodic oscillation of the cell impedance during cycles was also observed when TEOS-treatment was conducted (Fig. 17). Although they did not provide a clear answer to this phenomenon, it might be derived from the subtle change (loss and recovery) of the contact area between Li metal and the protective layer, which is analogous to the case of Li/solid electrolyte interfaces. Yan *et al.*, modified the surface of a Cu current collector with 2D hexagonal BN (h-BN) ultrathin layer, corresponding to one to ten atomic layers, by chemical vapor deposition (Fig. 18) [92]. Owing to the much higher Young's modulus of h-BN (approaching 1 TPa) relative to that for common inorganic components in native SEI (around 100 GPa), stable Li deposition-dissolution could be realized for more than 50 cycles at 1 mA/cm^2 with coulombic efficiency ~ 97%. Stable cycling with dramatic suppression of side reactions with electrolyte can be realized by adopting these methods. In addition, the formation of a protective layer on Li by chemical reactions, instead of by physical attachment, generally leads to better adhesion to a Li metal electrode, which is beneficial for decreasing the interfacial resistance. However, there is always a risk that the cell failure suddenly occurs once the protective layer suffers serious damage and the reactions between Li metal and electrolyte starts, which is because the protective layer is incapable of self-remedying.

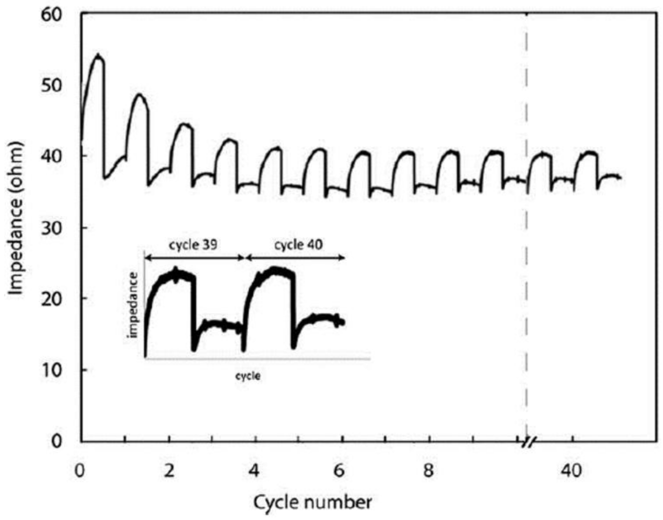

Fig. 17. Time variation of the cell impedance during Li deposition-dissolution cycles when TEOS-treatment was conducted for a Li metal electrode (Reprinted by permission from ref. 91. Copyright 2011, Royal Chemical Society).

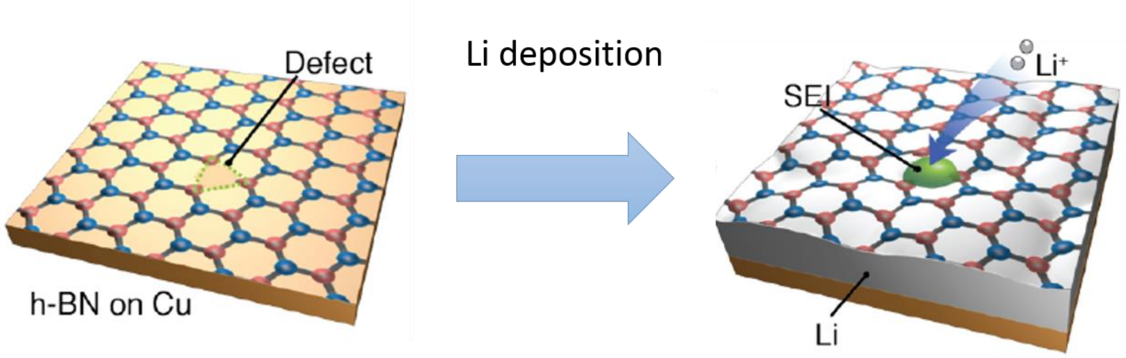

Fig. 18. Schematic illustration of Li deposition on a h-BN modified Cu current collector (Adapted by permission from ref. 92. Copyright 2014, American Chemical Society).

1.4.1.3. Replacement of organic electrolytes with polymer electrolytes

The use of polymer electrolytes instead of non-aqueous electrolytes is one solution. The consumption of Li metal by the reactions with electrolyte and the growth of Li dendrites are expected to be suppressed because of its higher stability against Li metal and higher shear modulus compared to those of organic electrolytes. However, batteries using polymer electrolytes need to be operated at elevated temperature (50~100 °C in general) to obtain the acceptable the Li^+ conductivity (~ 10^{-6} S/cm). The mechanical strength decreases at higher temperature and thus it is actually difficult to effectively block the growth of Li dendrites. Thus several attempts have been made to strengthen the electrolyte without sacrifying Li^+ conductivity and stability against Li metal by optimizing the polymer composition and structure and by introducing plasticizers or inorganic fillers [12, 13, 93-98]. Liu *et al.*, reported that the onset time of Li dendrite formation can be extended more than twice by decreasing the Li/polymer electrolyte interfacial resistance (from several hundreds of Ω cm^2 to several tens of Ω cm^2) through adding nano-silica fillers and/or ionic liquids [12, 13, 98]. In addition, they claimed that the modification of the surface of the nano-silica fillers with Lewis acid groups can prevent side reactions with contaminated H_2O by scavenging it. The idea of polymeric single ion conductors is worth paying attention to for suppressing Li dendritic growth (The transference number of Li^+ is around 0.3 in typical PEO-based polymer electrolytes). Concentration gradient of ions does not appear in the electrolytes with the Li^+ transference number of unity and hence Li dendritic growth can be prevented according to the theory proposed by Chazalviel [32]. Bouchet *et al.*, succeeded in synthesizing a polymer electrolyte based on polyanionic block copolymers comprising polystyrene segments associated with a connection block comprising PEO segments (Fig. 19) [99]. This polymer exhibits Li^+ transference number exceeding 0.85, and also the tensile strength (~ 10 MPa @40 °C) much higher than that of conventional PEO due to the incorporation of rigid polystyrene blocks.

The Li metal battery using this electrolyte showed excellent cycling performance at the higher rate (up to 2C).

It should be mentioned that despite enormous amount of work, the dilemma between durability against Li dendrites and realization of the intimate interfacial contact still exists (Fig. 20). For mechanical blocking and the stability with Li metal, inorganic solid-state Li-ion conductors have the advantage although they also suffer from the construction of flexible interface with an electrode. Several strategies to solve this problem will be explained in detail in 1.4.3..

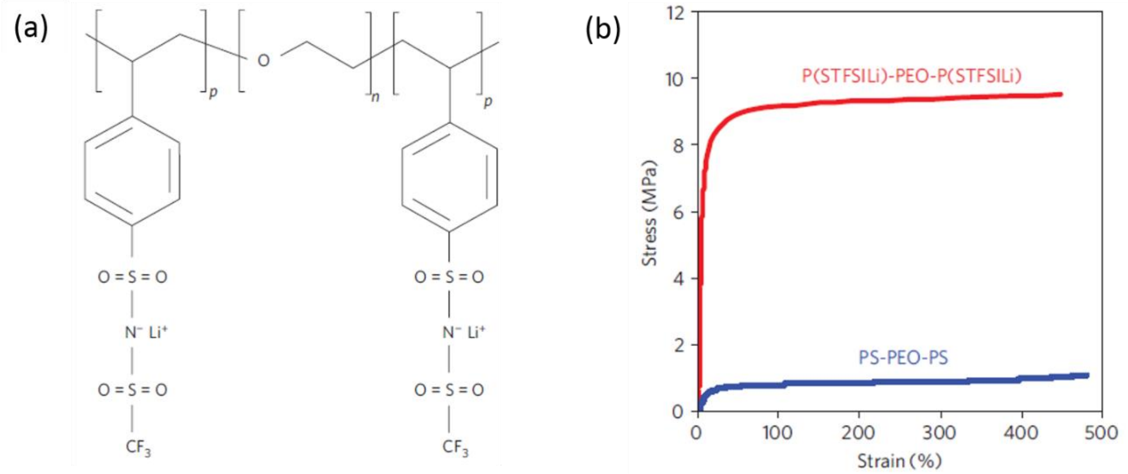

Fig. 19. (a) Chemical structure of the synthesized single-ion conducting copolymer and (b) comparison of the tensile strength obtained at 40 °C (Adapted by permission from ref. 99. Copyright 2013, Nature).

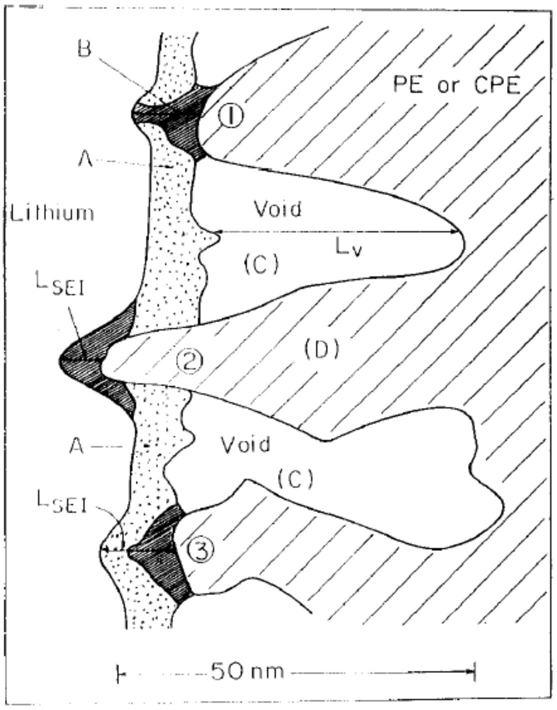

Fig. 20. Schematic illustration of a Li metal/polymer electrolyte interface. (A) native oxide film, (B) freshly formed SEI, (C) void, (D) polymer electrolyte. 1 and 3: softer contact between Li and polymer electrolyte, 2: spikes in polymer electrolyte (Reprinted by permission from ref. 94. Copyright 1995, Elsevier).

1.4.2. Air cathode / liquid electrolyte interfaces

The influence of cathode materials and their structure and morphology on the performance of Li-air batteries has been extensively investigated [44]. The development of efficient ORR and OER catalysts is a critical factor because the larger overpotential during both discharge and charge directly reduces the energy efficiency of the batteries. Moreover, the larger overpotential, especially during charge, induces the parasitic reactions and the corrosion of cathode substrates, which increasingly shorten the cycle life of Li-air batteries. Functional carbon materials, N-doped carbon materials, precious or transition metal oxides and metal-carbon composite materials have been explored as an electrocatalyst utilized at an air cathode. Among them, the compounds with transition metals coordinated to heterocyclic N comprise one group of metal-carbon composite materials, and they are attracting more attention because they have intrinsically high ORR and/or OER activity as revealed in the field of electrocatalysts for fuel cells [100, 101]. In addition, this group of materials possess relatively higher design flexibility than bulk materials, which is advantageous especially when a solution-mediated Li_2O_2 formation pathway is induced and hence the covering of the catalyst surface by Li_2O_2 deposits is suppressed. Shui *et al.*, demonstrated the atomically dispersed Fe/N/C composite exhibited low overpotential especially during charge (less than 4.0 V) accompanied with the exclusive production of O_2 as the charge product (Fig. 21) [102]. Trahan *et al.*, obtained Li_2O as one of the discharge products on CoPc-containing carbon, which forms a complex with superoxide, lowering the activation energy of O_2 [103]. Zhang *et al.*, indicated that the heat-treated FeCuPc supported on carbon black can also catalyze the chemical disproportionation of Li_2O_2 to Li_2O and O_2 [104]. Some catalysts were also developed for hybrid-type Li-air batteries in which ORR and OER proceed in aqueous media in analogy to the electrocatalysts for fuel cells [105].

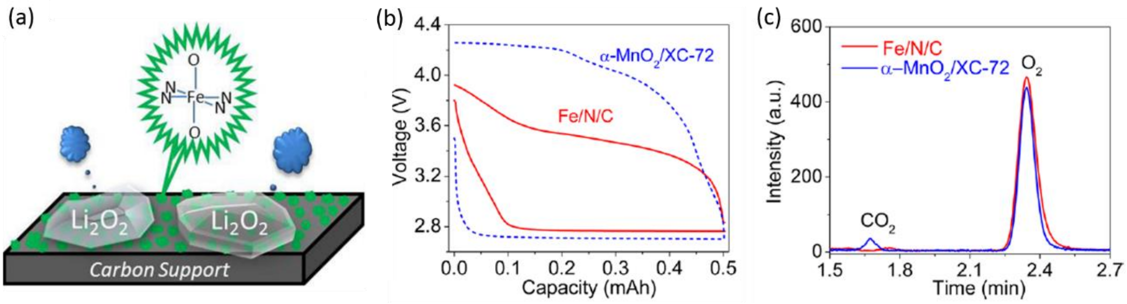

Fig. 21. (a) Schematic illustration of the reactions proceeded on a proposed Fe/N/C cathode catalyst (b) Voltage profiles of Li-O_2 cells using the well-studied α-MnO_2/XC-72 carbon or the Fe/N/C as a cathode catalyst, (c) GC signals for the gas effluents collected at the end of charge (Adapted by permission from ref. 102. Copyright 2012, American Chemical Society).

The effects of H_2O on the performance of Li-air batteries in the presence of electrocatalysts are also of great importance for the following reasons: (i) H_2O is one of the representative contaminants and thus the knowledge about its effects is highly required for designing the batteries; (ii) the chemistry of ORR and OER has been originally well studied in aqueous systems and hence the knowledge can be applied especially in the presence of H_2O although the reaction mechanism is somewhat different between aqueous and nonaqueous systems; (iii) the kinetics of ORR and OER are known to be faster in aqueous systems than those in nonaqueous ones due to the higher solubility of O_2 in aqueous media [106], which suggests the possibility of the use of H_2O as an additive in organic electrolytes which facilitates ORR and OER. Giordani *et al*., reported that there is an inverse linear relationship between the rate constant for H_2O_2 decomposition and the charging voltage of Li_2O_2 (Fig. 22) [107]. Despite the importance of these topics, the knowledge about the influence of H_2O on the performance of catalysts on air cathodes is still relatively limited.

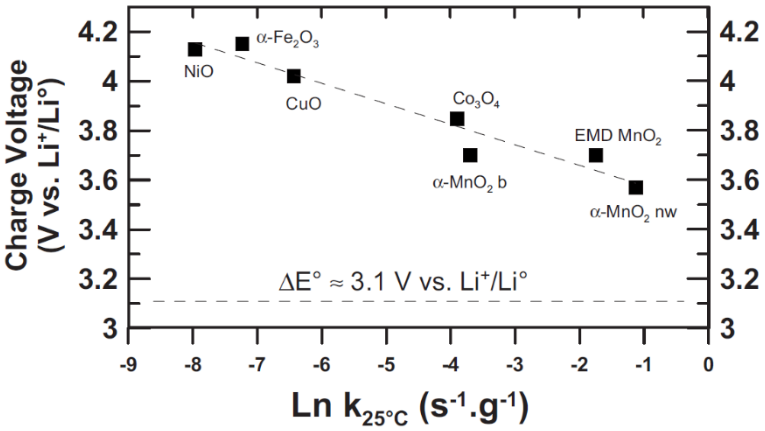

Fig. 22. Relationship between the Li_2O_2 decomposition charge voltage of Li-O_2 cells and H_2O_2 decomposition rate constant at 25 °C (Ln $k_{25\,°C}$) (Reprinted by permission from ref. 107. Copyright 2010, Electrochemical Society).

1.4.3. Li metal / solid electrolyte interfaces

As mentioned in 1.3.3., decreasing R_{int} is an urgent problem for the real application of all-solid-state batteries with high energy density and power density. Thus several attempts have been made to reduce R_{int}: application of high external pressure [14, 65] and temperature [66, 108], tuning the chemical composition of LLZ [68], modification of the surface morphology of LLZ by optimization of the particle and grain sizes [63, 64, 67, 69, 109], and the insertion of a lithiophilic layer between Li and LLZ [110-116].

Increasing the cell pressure is known to be a general method to suppress the voids growth during metal dissolution at a metal/solid electrolyte interface [71]. Indeed, Basappa *et al*., obtained lower R_{int} compared to the reported values when a symmetrical Li/LLZ/Li cell was assembled under the higher cell pressure (1.4 MPa) [14]. Sharafi *et al*., reported that R_{int} decreased from 5822 Ω cm^2 to 514 Ω cm^2 by improving the Li/LLZ interfacial contact through ten cycles of Li deposition-dissolution at 175 °C [108]. Yonemoto *et al*., demonstrated that the similar preconditioning of a Li/LLZ interface is effective to improve cycling stability when the increased amount of Li is deposited and dissolved repetitively [66].

Cheng *et al*., demonstrated that a LLZ pellet can be more air-stable by decreasing the grain size from ~ 150 μm to ~ 20 μm [64]. The formation of resistive Li_2CO_3 on the LLZ surface is suppressed for a smaller-grained LLZ pellet because Al, which is the substituting element in LLZ and effective to delay the reactions of Li_2CO_3 formation, is retained in the grains for a smaller-grain sample by preventing the extensive grain growth. The same group also reported that decreasing the grain size (20 ~ 40 μm) is effective to reduce R_{int} (37 Ω cm^2) and to suppress Li dendritic growth [69]. Since the resistivity is different between the surface grains and grain boundaries, the distribution of Li^+ flux is inhomogeneous at a Li/LLZ interface. This non-uniformity is mitigated for a smaller-grained sample because the low resistive grain boundaries distribute at the higher density (Fig. 23). Thus the improved electrochemical performance was obtained for a smaller-grained LLZ.

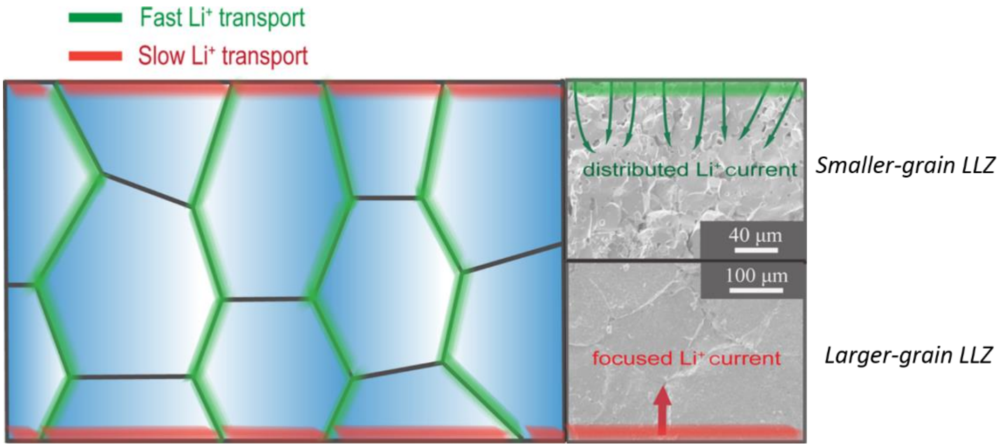

Fig. 23. Schematic illustration of the distribution of ionic current for LLZ with smaller (20 ~ 40 µm) and larger (100 ~ 200 µm) grain size (Adapted by permission from ref. 69. Copyright 2015, American Chemical Society).

In recent years, several kinds of metal (Au, Al, Si, Ge, Zn) which can form alloys with Li have been introduced as a buffer layer (5 ~ 100 nm thickness) between Li and LLZ (Fig. 24a) [110-116]. R_{int} was decreased by a factor of more than 10 when the buffer layers were inserted (Fig. 24b). Moreover, the buffer layer was effective to improve the capacity and power characteristics of the cell (Fig. 24c). It is suggested that the Li-alloy at the interface helps to maintain the Li/LLZ interfacial contact by increasing the lithiophilicity of the LLZ surface. However, the distribution of the alloy and its function during prolonged cycle are still unclear.

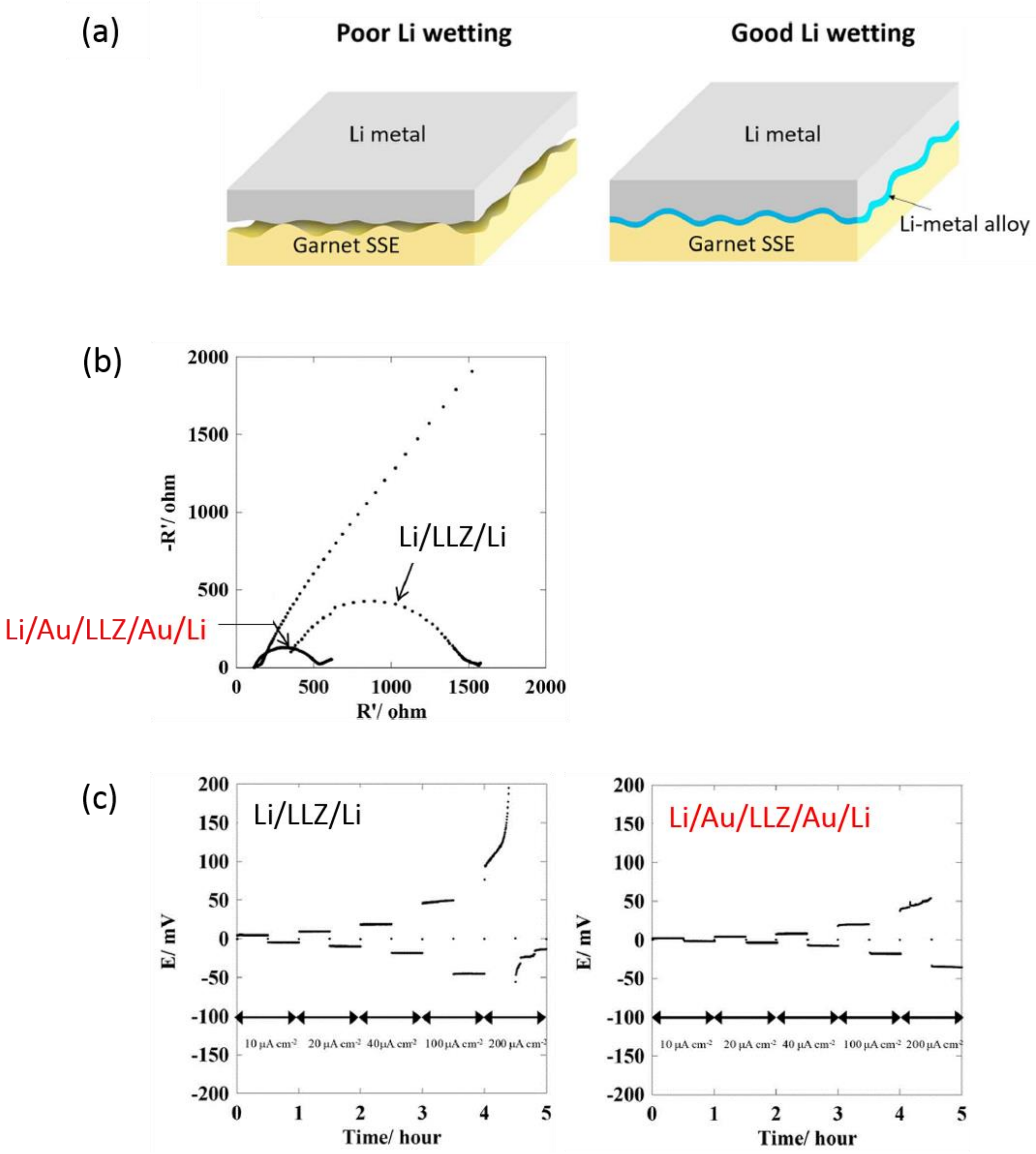

Fig. 24. (a) Schematic illustration of improved wettability of solid electrolyte (SSE) against Li metal by the introduction of Li-metal alloy layer (Adapted by permission from ref. 115. Copyright 2017, Creative Commons), (b) Nyquist plots of symmetrical cells with the configuration of Li/LLZ/Li and Li/Au/LLZ/Au/Li, (c) Li deposition-dissolution cycle test conducted at 60 °C for a Li/LLZ/Li and a Li/Au/LLZ/Au/Li cell (Adapted by permission from ref. 114. Copyright 2017, Electrochemical Society).

1.5. Background and objective of this thesis

For the real application of Li metal secondary batteries, both the decrement of the charge-discharge efficiency by the reactions of Li metal with electrolyte and the cell short-circuit caused by the growth of Li dendrite should be prevented. Currently, there are two principal approaches to solve these problems inherent in the use of a Li metal electrode: (1) the formation of passivation layer with high Li-ion conductivity, high elasticity and no electrical conductivity, named as solid electrolyte interface (SEI), at Li/electrolyte interfaces, and (2) the use of solid-state Li-ion conductors with high stability against Li metal as electrolytes instead of conventional organic electrolytes. As for the former, although numerous kinds of electrolyte and additive have been developed to improve the physicochemical properties of SEI, the batteries with acceptable performance for commercialization in view of charge-discharge efficiency, operating current density and capacity have not appeared yet. With regard to the latter, the comprehensive understanding of Li deposition-dissolution (charge-discharge) reactions proceeded at Li/solid electrolyte interfaces is still lacking due to the distinct properties of solid/solid interfaces relative to those of solid/liquid interfaces, which interferes with the successful utilization of solid electrolytes.

In the present thesis, studies were conducted to deepen the understanding of Li deposition-dissolution reactions proceeded at Li/organic electrolyte interfaces and Li/solid electrolyte interfaces, and then to obtain the design principles of the interfaces indispensable to the real application of Li metal secondary batteries.

1.6. Overview of this thesis

In chapter 2, the author examined the effects of contaminated water on reactions proceeded at negative (chapter 2-1) and positive (chapter 2-2) electrodes in Li-air batteries to understand the influence of contaminant water on the charge-discharge efficiency and energy efficiency. Even though the elaborate design of electrolyte is conducted, contaminants cause the unexpected change on the properties of SEI and hence have significant influence on the battery performance, especially for batteries exposed to air like Li-air batteries. Thus knowing the allowable concentration range of contaminants is indispensable to design Li-air batteries. However, this quantitative knowledge has not still accumulated enough, especially for a Li negative electrode. Based on these considerations, the author investigated the relationship between the concentration of contaminant water and the coulombic efficiency of Li deposition-dissolution reactions. It was revealed that the coulombic efficiency reaches maximum at 80% with increasing water concentration up to 1000 ppm, associated with the formation of a Li_2O-rich passivation layer. Based on this result, the author also attempted to investigate the possibility of the utilization of water as the additive which enhances the charge-discharge performance in Li-air batteries. For the effective use of water at a positive electrode, electrocatalysts for oxygen reduction reaction (ORR) in aqueous media was first synthesized, and then the catalysts was employed as the positive electrode material. The Li-air battery performance was maintained even when the electrolyte contained several thousands ppm of water; however, the beneficial effects of water in the presence of the electrocatalyst were not significantly observed. The electrocatalysts have to be designed in a more sophisticated way to efficiently break and reform the double bond of molecular oxygen.

In chapter 3, the author analyzed the dynamic changes of charge transfer resistance at a Li/$Li_7La_3Zr_2O_{12}$ (LLZ) solid electrolyte interface during Li deposition-dissolution reactions to obtain the design principle of the interface which can endure during prolonged cycle at the practical current density. LLZ is advantageous due to its high stability against Li metal; however, the higher charge transfer resistance at a Li/LLZ interface compared to that at conventional Li/organic electrolyte interfaces hinders the operation of LLZ-based solid-state batteries at a practical rate. The direct observation of the Li/LLZ interfaces is difficult due to the strong attachment of Li metal to LLZ, which is an obstacle to solve the problems originated from the interface. Based on these considerations, the author attempted to individually trace the dynamic change in the Li/LLZ interfacial resistance during Li deposition and dissolution reactions through the use of the three-electrode AC impedance technique. It was revealed that the resistance respectively increases and decreases during Li dissolution and deposition, associated with the formation and disappearance of voids at the Li/LLZ interface. These results indicate the importance to prevent the voids formation at the Li/LLZ interface, particularly during Li dissolution.

In chapter 4, the author examined the function of a Au layer introduced at the Li/LLZ interface during Li deposition-dissolution reactions to gain knowledge for controlling the dynamic change in the charge transfer resistance at the interface. The insertion of a metal layer which can form alloys with Li (e.g. Au, Al and Si) at the interface is known to be effective to decrease the interfacial resistance and to improve the battery performance. However, its function on Li deposition and dissolution reactions are still unclear. Based on these considerations, the author attempted to clarify the function of the introduced Au during Li dissolution and deposition reactions by applying the three-electrode AC impedance technique established in chapter 3. It was demonstrated that the Au introduced at the interface was diffused into the bulk of Li foil attached afterwards, leading to the formation of the interface with lower charge transfer resistance. It was revealed that the increase in the electrode/LLZ interfacial contact area by inserting Au using a deposition method should considerably contribute to the decreased interfacial resistance. In addition, the formation of Li-Au solid solution through the diffusion of Au into Li might also affect the interfacial resistance and hence the electrochemical performance. These results stress the importance of considering the influence of the introduced buffer layer on the interfacial contact area as well as its physicochemical properties for designing the interface.

In chapter 5, the research contents described in this thesis were briefly overviewed. In addition, the future prospects of Li metal secondary batteries were discussed.

References

[1] W. Xu, J. Wang, F. Ding, X. Chen, E. Nasybulin, Y. Zhang, J.-G. Zhang, *Energy Environ. Sci.,* **2014**, *7*, 513.

[2] K. M. Abraham, Z. Jiang, *J. Electrochem. Soc*., **1996**, *143*, 1.

[3] B. D. McCloskey, C. M. Burke, J. E. Nichols, S. E. Renfrew, *Chem. Commun*., **2015**, *51*, 12701.

[4] Y.-C. Lu, B. M. Gallant, D. G. Kwabi, J. R. Harding, R. R. Mitchell, M. S. Whittingham, Y. Shao-Horn, *Energy Environ. Sci*., **2013**, *6*, 750.

[5] S. J. Visco, B. D. Katz, Y. S. Nimon, L. D. Dejonghe, U.S. patent 7,282,295, **2007**

[6] I. Kowalczk, J. Read, M. Salomon, *Pure Appl. Chem*., **2007**, *79*, 851.

[7] Y. Wang, H. Zhou, *J. Power Sources*, **2010**, *195*, 358.

[8] P. He, T. Zhang, J. Jiang, H. Zhou, *J. Phys. Chem. Lett*., **2016**, *7*, 1267.

[9] T. Zhang, N. Imanishi, S. Hasegawa, A. Hirano, J. Xie, Y. Takeda, O. Yamamoto, N. Sammes, *J. Electrochem. Soc*., **2008**, *155*, A965.

[10] T. Zhang, N. Imanishi, S. Hasegawa, A. Hirano, J. Xie, Y. Takeda, O. Yamamoto, N. Sammes, *Electrochem. Solid-State Lett*., **2009**, *12*, A132.

[11] T. Zhang, N. Imanishi, A. Hirano, Y. Takeda, O. Yamamoto, *Electrochem. Solid-State Lett.*, **2011**, *14*, A45.

[12] S. Liu, N. Imanishi, T. Zhang, A. Hirano, Y. Takeda, O. Yamamoto, J. Yang, *J. Electrochem. Soc*., **2010**, *157*, A1092.

[13] S. Liu, H. Wang, N. Imanishi, T. Zhang, A. Hirano, Y. Takeda, O. Yamamoto, J. Yang, *J. Power Sources*, **2011**, *196*, 7681.

[14] K. Ishiguro, H. Nemori, S. Sunahiro, Y. Nakata, R. Sudo, M. Matsui, Y. Takeda, O. Yamamoto, N. Imanishi, *J. Electrochem. Soc*., **2014**, *161*, A668.

[15] K. Kerman, A. Luntz, V. Viswanathan, Y.-M. Chiang, Z. Chen, *J. Electrochem. Soc.*, **2017**, *164*, A1731.

[16] A.C. Luntz, J. Voss, K. Reuter, *J. Phys. Chem. Lett.*, **2015**, *6*, 4599.

[17] J. Janek, W. G. Zeier, *Nat. Energy,* **2016**, *1*, 16141.

[18] N. Kamaya, K. Homma, Y. Yamakawa, M. Hirayama, R. Kanno, M. Yonemura, T. Kamiyama, Y. Kato, S. Hama, K. Kawamoto, *Nat. Mater.*, **2011**, *10*, 682.

[19] Y. Kato, S. Hori, T. Saito, K. Suzuki, M. Hirayama, A. Mitsui, M. Yonemura, H. Iba, R. Kanno, *Nat. Energy*, **2016**, *1*, 16030.

[20] W. D. Richards, L. J. Miara, Y. Wang, J. C. Kim, G. Ceder, *Chem. Mater*., **2016**, *28*, 266.

[21] Y. Zhu, X. He, Y. Mo, *ACS Appl. Mater. Interfaces*, **2015**, *7*, 23685.

[22] R. Murugan, V. Thangadurai, W. Weppner, *Angew. Chem. Int. Ed*., **2007**, *46*, 7778.

[23] S. Ramakumar, C. Deviannapoorani, L. Dhivya, L. S. Shankar, R. Murugan, *Prog. Mater. Sci*., **2017**, *88*, 325.

[24] C. Ma, Y. Cheng, K. Yin, J. Luo, A. Sharafi, J. Sakamoto, J. Li, K. L. More, N. J. Dudney, M. Chi, *Nano Lett*., **2016**, *16*, 7030.

[25] F. Han, Y. Zhu, X. He, Y. Mo, C. Wang, *Adv. Energy Mater.*, **2016**, *6*, 1501590.

[26] M. Nakayama, M. Kotobuki, H. Munakata, M. Nogami, K. Kanamura, *Phys. Chem. Chem. Phys*., **2014**, *14*, 10008.

[27] D. Aurbach, E. Zinigrad, Y. Cohen, H. Teller, *Solid State Ionics*, **2002**, *148*, 405.

[28] E. Peled, *J. Electrochem. Soc*., **1979**, *126*, 2047.

[29] D. Aurbach, E. Zinigrad, H. Teller, P. Dan, *J. Electrochem. Soc*., **2000**, *147*, 1274.

[30] B. L. Mehdi, A. Stevens, J. Qian, C. Park, W. Xu, W. A. Henderson, J.-G. Zhang, K. T. Mueller, N. D. Browning, *Sci. Rep*., **2016**, *6*, 34267.

[31] D. Aurbach, *J. Power Sources*, **2000**, *89*, 206.

[32] J. N. Chazalviel, *Phys. Rev. A*, **1990**, *42*, 7355.

[33] C. Brissot, M. Rosso, J. N. Chazalviel, S. Lascaud, *J. Power Sources*, **1999**, *81-82*, 925.

[34] M. Rosso, C. Brissot, A. Teyssot, M. Dolle, L. Sannier, J.-M. Tarascon, R. Bouchet, S. Lascaud, *Electrochim. Acta*, **2006**, *51*, 5334.

[35] M. Rosso, T. Gobron, C. Brissot, J. N. Chazalviel, S. Lascaud, *J. Power Sources*, **2001**, *97-98*, 804.

[36] C. Monroe, J. Newman, *J. Electrochem. Soc*., **2003**, *150*, A1377.

[37] K. Nishikawa, E. Chassaing, M. Rosso, *Electrochim. Acta*, **2011**, *56*, 5464.

[38] K. Nishikawa, T. Mori, T. Nishida, Y. Fukunaka, M. Rosso, *J. Electroanal. Chem*., **2011**, *661*, 84.

[39] J. Yamaki, S. Tobishima, K. Hayashi, K. Saito, Y. Nemoto, M. Arakawa, *J. Power Sources*, **1998**, *74*, 219.

[40] N. Togasaki, T. Momma, T. Osaka, *J. Power Sources*, **2015**, *294*, 588.

[41] D. Aurbach, I. Weissman, A. Zaban, O. Chusid, *Electrochim. Acta*, **1994**, *39*, 51.

[42] D. Aurbach, A. Zaban, *J. Electroanal. Chem*., **1993**, *348*, 155.

[43] D. Aurbach, A. Zaban, Y. Gofer, Y. E. Ely, I. Weissman, O. Chusid, O. Abramson, *J. Power Sources*, **1995**, *54*, 76.

[44] Z. Ma, X. Yuan, L. Li, Z.-F. Ma, D. P. Wilkinson, L. Zhang, J. Zhang, *Energy Environ. Sci*., **2015**, *8*, 2144.

[45] N. B. Aetukuri, B. D. McCloskey, J. M. García, L. E. Krupp, V. Viswanathan, A. C. Luntz, *Nat. Chem*., **2015**, *7*, 50.

[46] G. Wang, L. Huang, S. Liu, J. Xie, S. Zhang, P. Zhu, G. Cao, X. Zhao, *ACS Appl. Mater. Interfaces*, **2015**, *7*, 23876.

[47] M. H. Cho, J. Trottier, C. Gagnon, P. Hovington, D. Clement, A. Vijh, C.-S. Kim, A. Guerfi, R. Black, L. Nazar, K. Zaghib, *J. Power Sources*, **2014**, *268*, 565.

[48] Z. Guo, X. Dong, Y. Wang, Y. Xia, *Chem. Commun*., **2015**, *51*, 676.

[49] K. U. Schwenke, M. Metzger, T. Restle, M. Piana, H. A. Gasteiger, *J. Electrochem. Soc*., **2015**, *162*. A573.

[50] Y. Qiao, S. Wu, J. Yi, Y. Sun, S. Guo, S. Yang, P. He, H. Zhou, *Angew. Chem. Int. Ed*., **2017**, *56*, 4960.

[51] T. Liu, M. Leskes, W. Yu, A. J. Moore, L. Zhou, P. M. Bayley, G. Kim, C. P. Grey, *Science*, **2015**, *350*, 530.

[52] F. Li, S. Wu, D. Li, T. Zhang, P. He, A. Yamada, H. Zhou, *Nat. Commun*., **2015**, *6*, 8843.

[53] Y. Yang, G. Zheng, Y. Cui, *Chem. Soc. Rev*., **2013**, *42*, 3018.

[54] H. Moon, T. Mandai, R. Tatara, K. Ueno, A. Yamazaki, K. Yoshida, S. Seki, K. Dokko, M. Watanabe, *J. Phys. Chem. C*, **2015**, *119*, 3957.

[55] R. Black, S. H. Oh, J. Lee, T. Yim, B. Adams, L. F. Nazar, *J. Am. Chem. Soc*., **2012**, *134*, 2902.

[56] Y. Okamoto, Y. Kubo, *J. Phys. Chem. C*, **2013**, *117*, 15940.

[57] N. Togasaki, T. Momma, T. Osaka, *J. Power Sources*, **2014**, *261*, 23.

[58] D. G. Kwabi, T. P. Batcho, S. Feng, L. Giordano, C. V. Thompson, Y, Shao-Horn, *Phys. Chem. Chem. Phys*., **2016**, *18*, 24944.

[59] P. Hartmann, T. Leichtweiss, M. R. Busche, M. Schneider, M. Reich, J. Sann, P. Adelhelm, J. Janek, *J. Phys. Chem. C*, **2013**, *117*, 21064.

[60] S. Wenzel, T. Leichtweiss, D. Krüger, J. Sann, J. Janek, *Solid State Ionics*, **2015**, *278*, 98.

[61] S. Wenzel, S. Randau, T. Leichtweiß, D. A. Weber, J. Sann, W. G. Zeier, J. Janek, *Chem. Mater*., **2016**, *28*, 2400.

[62] L. Cheng, E.J. Crumlin, W. Chen, R. Qiao, H. Hou, S.F. Lux, V. Zorba, R. Russo, R. Kostecki, Z. Liu, K. Persson, W. Yang, J. Cabana, T. Richardson, G. Chen, M. Doeff, *Phys. Chem. Chem. Phys*., **2014**, *16*, 18294.

[63] L. Cheng, J. S. Park, H. Hou, V. Zorba, G. Chen, T. Richardson, J. Cabana, R. Russo, M. Doeff, *J. Mater. Chem. A*, **2014**, *2*, 172.

[64] L. Cheng, C. H. Wu, A. Jarry, W. Chen, Y. Ye, J. Zhu, R. Kostecki, K. Persson, J. Guo, M. Salmeron, G. Chen, M. Doeff, *ACS Appl. Mater. Interfaces*, **2015**, *7*, 17649.

[65] R.H. Basappa, T. Ito, H. Yamada, *J. Electrochem. Soc*., **2017**, *164*, A666.

[66] F. Yonemoto, A. Nishimura, M. Motoyama, N. Tsuchimine, S. Kobayashi, Y. Iriyama, *J. Power Sources*, **2017**, *343*, 207.

[67] M. Botros, R. Djenadic, O. Clemens, M. Möller, H. Hahn, *J. Power Sources*, **2016**, *309*, 108.

[68] H. Buschmann, S. Berendts, B. Mogwitz, J. Janek, *J. Power Sources*, **2012**, *206*, 236.

[69] L. Cheng, W. Chen, M. Kunz, K. Persson, N. Tamura, G. Chen, M. Doeff, *ACS Appl. Mater. Interfaces*, **2015**, *7*, 2073.

[70] T. R. Jow, C. C. Liang, *J. Electrochem. Soc*., **1983**, *130*, 737.

[71] T. R. Jow, C. C. Liang, *Solid State Ionics*, **1983**, *9–10*, 695.

[72] J. Janek, *Solid State Ionics*, **2000**, *131*, 129.

[73] M. Meyer, H. Rickert, U. Schwaitzer, *Solid State Ionics*, **1983**, *9-10*, 689.

[74] E. J. Cheng, A. Sharafi, J. Sakamoto, *Electrochim. Acta*, **2017**, *223*, 85.

[75] Y. Ren, Y. Shen, Y. Lin, C.-W. Nan, *Electrochem. Commun*., **2015**, *57*, 27.

[76] F. Aguesse, W. Manalastas, L. Buannic, J. M. L. Amo, G. Singh, A. Llordes, J. Kilner, *ACS Appl. Mater. Interfaces*, **2017**, *9*, 3808.

[77] R. D. Schmidt, J. Sakamoto, *J. Power Sources*, **2016**, *324*, 126.

[78] L. Porz, T. Swamy, B. W. Sheldon, D. Rettenwander, T. Frömling, H. L. Thaman, S. Berendts, R. Uecker, W. C. Carter, Y.-M. Chiang, *Adv. Energy Mater*., **2017**, *7*, 1701003.

[79] M. Motoyama, M. Ejiri, Y. Iriyama, *J. Electrochem. Soc*., **2015**, *162*, A7067.

[80] M. Motoyama, M. Ejiri, Y. Iriyama, *Electrochemistry*, **2014**, *82*, 364.

[81] F. Sagane, R. Shimokawa, H. Sano, H. Sakaebe, Y. Iriyama, *J. Power Sources*, **2013**, *225*, 245.

[82] F. Sagane, K. Ikeda, K. Okita, H. Sano, H. Sakaebe, Y. Iriyama, *J. Power Sources*, **2013**, *233*, 34.

[83] K. Okita, K. Ikeda, H. Sano, Y. Iriyama, H. Sakaebe, *J. Power Sources*, **2011**, *196*, 2135.

[84] C. Monroe, J. Newman, *J. Electrochem. Soc*., **2005**, *152*, A396.

[85] P. Dan, E. Mengeritsky, D. Aurbach, I. Weissman, E. Zinigrad, *J. Power Sources*, **1997**, *68*, 443.

[86] Y. Gofer, M. Ben-Zion, D. Aurbach, *J. Power Sources*, **1992**, *39*, 163.

[87] J. Qian, W. Xu, P. Bhattacharya, M. Engelhard, W. A. Henderson, Y. Zhang, J.-G. Zhang, *Nano Energy*, **2015**, *15*, 135.

[88] T. Osaka, T. Momma, Y. Matsumoto, Y. Uchida, *J. Power Sources*, **1997**, *68*, 497.

[89] T. Osaka, T. Momma, Y. Matsumoto, Y. Uchida, *J. Electrochem. Soc*., **1997**, *144*, 1709.

[90] T. Osaka, T. Momma, T. Tajima, Y. Matsumoto, *J. Electrochem. Soc*., **1995**, *142*, 1057.

[91] G. A. Umeda, E. Menke, M. Richard, K. L. Stamm, F. Wudl, B. Dunn, *J. Mater. Chem*., **2011**, *21*, 1593.

[92] K. Yan, H.-W. Lee, T. Gao, G. Zheng, H. Yao, H. Wang, Z. Lu, Y. Zhou, Z. Liang, Z. Liu, S. Chu, Y. Cui, *Nano. Lett*., **2014**, *14*, 6016.

[93] B. Scrosati, A. Selvaggi, F. Croce, W. Gang, *J. Power Sources*, **1988**, *24*, 287.

[94] E. Peled, D. Golodnitsky, G. Ardel, V. Eshkenazy, *Electrochim. Acta*, **1995**, *40*, 2197.

[95] T. Matsui, K. Takeyama, *Electrochim. Acta*, **1995**, *40*, 2165.

[96] N. S. Choi, B. Koo, J. T. Yeon, K. T. Lee, D. W. Kim, *Electrochim. Acta*, **2011**, *56*, 7249.

[97] T. Tatsuma, M. Taguchi, N. Oyama, *Electrochim. Acta*, **2001**, *46*, 1201.

[98] S. Liu, N. Imanishi, T. Zhang, A. Hirano, Y. Takeda, O. Yamamoto, J. Yang, *J. Power Sources*, **2010**, *195*, 6847.

[99] R. Bouchet, S. Maria, R. Meziane, A. Aboulaich, L. Lienafa, J.-P. Bonnet, T. N. T. Phan, D. Bertin, D. Gigmes, D. Devaux, R. Denoyel, M. Armand, *Nat. Mater*., **2013**, *12*, 452.

[100] M. Lefèvre, E. Proietti, F. Jaouen, J.-P. Dodelet, *Science*, **2009**, *324*, 71.

[101] G. Wu, K. L. More, C. M. Johnston, P. Zelenay, *Science*, **2011**, *332*, 443.

[102] J.-L. Shui, N. K. Karan, M. Balasubramanian, S.-Y. Li, D.-J. Liu, *J. Am. Chem. Soc*., **2012**, *134*, 16654.

[103] M. J. Trahan, Q. Jia, S. Mukerjee, E. J. Plichta, M. A. Hendrickson, K. M. Abraham, *J. Electrochem. Soc*., **2013**, *160*, A1577.

[104] S. S. Zhang, X. Ren, J. Read, *Electrochim. Acta*, **2011**, *56*, 4544.

[105] E. Yoo, H. Zhou, *J. Power Sources*, **2013**, *244*, 429.

[106] S. H. Lee, R. A. DeMayo, K. J. Takeuchi, E. S. Takeuchi, A. C. Marschilok, *J. Electrochem. Soc*., **2015**, *162*, A69.

[107] V. Giordani, S. A. Freunberger, P. G. Bruce, J.-M. Tarascon, D. Larcher, *Electrochem. Solid-State Lett*., **2010**, *13*, A180.

[108] A. Sharafi, H. M. Meyer, J. Nanda, J. Wolfenstine, J. Sakamoto, *J. Power Sources*, **2016**, *302*, 135.

[109] E. Rangasamy, J. Wolfenstine, J. Sakamoto, *Solid State Ionics*, **2012**, *206*, 28.

[110] C.-L. Tsai, V. Roddatis, C. V. Chandran, Q. Ma, S. Uhlenbruck, M. Bram, P. Heitjans, O. Guillon, *ACS Appl. Mater. Interfaces*, **2016**, *8*, 10617.

[111] X. Han, Y. Gong, K. K. Fu, X. He, G. T. Hitz, J. Dai, A. Pearse, B. Liu, H. Wang, G. Rubloff, Y. Mo, V. Thangadurai, E. D. Wachsman, L. Hu, *Nat. Mater*., **2017**, *16*, 572.

[112] W. Luo, Y. Gong, Y. Zhu, K. K. Fu, J. Dai, S. D. Lacey, C. Wang, B. Liu, X. Han, Y. Mo, E. D. Wachsman, L. Hu, *J. Am. Chem. Soc*., **2016**, *138*, 12258.

[113] W. Luo, Y. Gong, Y. Zhu, Y. Li, Y. Yao, Y. Zhang, K. K. Fu, G. Pastel, C.-F. Lin, Y. Mo, E. D. Wachsman, L. Hu, *Adv. Mater*., **2017**, *29*, 1606042.

[114] J. Wakasugi, H. Munakata, K. Kanamura, *J. Electrochem. Soc*., **2017**, *164*, A1022.

[115] K. K. Fu, Y. Gong, B. Liu, Y. Zhu, S. Xu, Y. Yao, W. Luo, C. Wang, S. D. Lacey, J. Dai, Y. Chen, Y. Mo, E. Wachsman, L. Hu, *Sci. Adv*., **2017**, *3*, e1601659.

[116] C. Wang, Y. Gong, B. Liu, K. Fu, Y. Yao, E. Hitz, Y. Li, J. Dai, S. Xu, W. Luo, E. D. Wachsman, L. Hu, *Nano Lett*., **2017**, *17*, 565.

Chapter 2

Effects of contaminant water on reactions proceeded at negative and positive electrodes in Li-air batteries

2.1. Effects of contaminant water on reactions proceeded at a negative electrode in Li-air batteries

2.1.1. Introduction

Lithium (Li)–air batteries have the potential to achieve significantly higher energy densities (> 3500 Wh/kg, including oxygen) than current state-of-the-art Li-ion batteries, and are therefore promising devices for use in sustainable energy management systems [1]. Despite the practical potential of Li-air batteries, they are limited by several issues to be solved. One of them is the low coulombic efficiency (CE) of Li metal deposition/dissolution reactions, which may occur due to moisture contamination from the air cathode [1-6]. In contrast, the performance of current Li-air batteries reported is improved in the presence of optimized amount of water (H_2O) [6-11]. Considering this background, the knowledge about the effects of H_2O concentration (C_{H2O}) on Li-anode reactions is critically important for the cell design of Li-air batteries; however, only a few studies have quantitatively examined this point [12, 13].

Recently, Togasaki et al. [12, 13] investigated the effects of H_2O on the CE of Li deposition/dissolution. They have revealed that a marked increase in the CE was observed at C_{H2O} of $\leq$ 35 ppm (up to a maximum of 88.9%) in carbonate-based electrolytes with dissolved carbon dioxide gas [12]. Further, the CE was shown to exceed 85% in C_{H2O} < 1000 ppm in dimethylsulfoxide (DMSO)-based electrolytes when the solid electrolyte interface (SEI) composed of inorganic compounds, such as lithium carbonate (Li_2CO_3), lithium oxide (Li_2O) and lithium fluoride (LiF), was formed [13]. Although these works are significant for the practical use of a Li-metal anode, the effects of H_2O on CE were investigated using carbonate- and DMSO-based electrolytes, which are easily decomposed by nucleophilic attack of reactive oxygen species generated at the air cathode and by contact with the Li-metal anode [14, 15].

Ether-based electrolytes have attracted considerable attention for use in Li-air batteries due to the higher stability of these solvents against reactive oxygen species and their greater compatibility with metallic Li [16-18]. In the present work, we therefore examined the C_{H2O} dependence of CE in a tetraglyme-based electrolyte, which is a representative ether solvent employed in Li-air batteries, with the aim of determining the integrated allowable range of C_{H2O} for Li deposition/dissolution reactions in ether-based electrolytes.

2.1.2. Experimental

2.1.2.1. Materials

Lithium bis(fluorosulfonyl)imide (LiFSI), lithium bis(trifluoromethanesulfonyl)imide (LiTFSI) and tetraethylene glycol dimethylether (TEGDME) were purchased from Kishida Chemical Co., Ltd. The Li salts were used as received without further purification and were dissolved in TEGDME, which had been dehydrated with molecular sieve 3A 1/8 (Wako Pure Chemical Industries, Ltd.), to prepare 1 M LiFSI-TEGDME and 1 M LiTFSI-TEGDME as electrolytes under a dry atmosphere (unavoidable $C_{\mathrm{H2O}} \approx 0.1$ ppm, which was estimated from the dew-point of the humidity-controlled room where the experiments were conducted). Various concentrations of H_2O (approximately from 500 ppm to 50000 ppm) were then introduced into the as-prepared electrolytes. The H_2O content of the electrolytes was determined by Karl Fischer titration (CA-21, Mitsubishi Chemical Analytech).

2.1.2.2. Electrochemical measurements

R2032 coin-type cells were assembled under a dry atmosphere. Nickel (Ni) foil (30-μm thickness, Nilaco Corp.) and metallic-Li foil (200-μm thickness, Honjo Metal Co., Ltd.) were used as working and counter electrodes, respectively. Porous polypropylene (PP, Celgard 2325) and glass filter (GF/A, Whatman) separators were dried at 60 °C for 15 h under vacuum. Then, two layers of PP/glass filter separators, with PP facing towards the Ni foil side of the cell, were used to improve the uptake of the highly viscous TEGDME solvent and to facilitate recovery of the electrode during the disassembly of cells. A total of 150 μl of each electrolyte with various C_{H2O} was introduced into each coin-type cell. Upon assembly of the coin-type cells, H_2O present in the system inevitably reacts with the Li counter electrode; however, we confirmed that a significant amount of H_2O was not consumed by the Li counter electrode by comparing the C_{H2O} change in the electrolyte during a 24-h storage at room temperature in the presence and absence of metallic-Li foil by Karl Fischer titration (Table 1).

CE was evaluated based on the Li deposition-dissolution cycle test proposed by Koch *et al.*, [19]. Briefly, 2 mAh/cm^2 of Li was initially electrodeposited onto the Ni foil substrate at 0.1 mA/cm^2 for 20 h. During each subsequent cycle, 0.2 mAh/cm^2 of Li was dissolved and deposited at 0.1 mA/cm^2 for 2 h. The cycle tests were terminated when the cell potential exceeded 1 V vs. Li/Li$^+$. CE was calculated using the equation: CE (%) = $[Q\mathrm{s} - (Q\mathrm{ex}/N)]/Q\mathrm{s}$, where Qs is the charge that passed during each deposition/dissolution process, Qex is the charge corresponding to the excess amount of Li deposited during the initial deposition process and N is the total number of cycles.

2.1.2.3. Characterizations

Field-emission SEM (FE-SEM; JSM-7800F, JEOL or Keysight8500, Agilent Tech.) was used to observe the surface morphology of the Ni working electrode after the first cycle of Li deposition. The measurement was conducted at an acceleration voltage of 1 or 5 kV under an ambient pressure of less than 10^{-4} Pa. X-ray photoelectron spectroscopy (XPS; VersaProbe 2, ULVAC-PHI) with monochromated Al Kα X-rays at hν = 1486.6 eV and 100 μm-spot size was used for investigating the chemical composition of the Li deposits. The measurement was conducted under an ambient pressure of 1~2 x 10^{-7} Pa. Ar^+ ion etching performed at an acceleration voltage of 2 kV and an ion beam current of 20 μA (etching rate: 7.7 nm/min for SiO_2 substrate) was used to obtain depth profiles. The spectra were shifted using carbon peak at 285.0 eV as a reference binding energy. The XPS peak-fitting was conducted using Shirley background subtraction and 70% Gaussian-30% Lorentzian peak shape. Peak position and full width at half maximum were fixed during the fitting process (Table 2).

After cycle tests, electrode samples were immediately removed, rinsed with 2 ml of dimethoxyethane and then dried in a glove box overnight. The samples were transferred from the glove box to the SEM and XPS instruments in purchased sealed vessels filled with Ar gas even without quick exposure to air.

2.1.3. Results and discussion

Fig. 1(a)-(c) show representative voltage vs. time curves for Li deposition/dissolution reactions in 1 M LiFSI-TEGDME containing C_{H2O} ranging from 14 to 3770 ppm. LiFSI-TEGDME was used as an electrolyte unless otherwise stated, as LiFSI salt has the potential to promote the reversible cycling of Li-anode reactions [20-22]. Notably, no significant decreases in C_{H2O} were observed after a 24-h storage of LiFSI-TEGDME without Li metal, confirming that the electrolyte is relatively stable against H_2O, as was previously reported [23]. At a C_{H2O} of 14 ppm, the total cycle number achieved until the cell potential exceeded 1 V vs. Li/Li^+ was 17, but reached 63 when C_{H2O} was increased to 766 ppm; however, as the C_{H2O} was further increased to 3770 ppm, the cycle number decreased to 23. Notably, when the C_{H2O} was set at ~1% (10000 ppm), a few cells exhibited a sharp increment in cell voltage, even during the initial stages of Li deposition, suggesting that Li metal was rapidly consumed in reactions with the excessive H_2O (data not shown) [20].

The estimated CEs in the experiments conducted with coin-type cells and 1 M LiFSI-TEGDME as an electrolyte were plotted against the C_{H2O} (Fig. 2, red circles). Error bars were presented based on four to six repetitive experiments. Although the CE ranged between 40% and 60% for the as-prepared electrolyte (unavoidable $C_{H2O} < 30$ ppm), the CE increased with increasing C_{H2O} until reaching 80% at a C_{H2O} of ~1000 ppm. The CE decreased at C_{H2O} values above 1000 ppm. A similar tendency was observed when 1 M LiTFSI-TEGDME was used as an electrolyte (Fig. 2, blue circles).

XPS analyses of the Ni working electrodes were conducted to investigate the effects of contaminant H_2O on the chemical composition of Li deposits. The chemical properties of the Li deposits formed during the initial Li deposition in the Li deposition-dissolution cycling protocol, in which an excessive amount of Li is first plated, largely influence the cycling performance [12, 13, 24-26]. For this reason, the chemical composition of the Li deposits formed during the first 20 h of operation at 0.1mA/cm^2 was examined. The average thickness of the Li layer after 20 h was calculated to be ~10 μm. To examine changes in the compositional depth profile of the Li deposits, Ar-ion sputtering was applied for 5, 10, 15, and 20 min. As the Li deposits are etched faster compared to the standard SiO_2 substrate (etching rate of 7.7 nm/min), the XPS spectra obtained after Ar-ion sputtering for 20 min corresponded to the layer located greater than 154 nm (7.7 nm/min x 20 min) from the surface. In the depth profile, the relative amounts of O and Li were clearly increased and decreased, respectively, as the C_{H2O} increased (Fig. 3).

The Li-1s and O-1s XPS spectra in 1 M LiFSI-TEGDME with various C_{H2O} are shown in Fig. 4. Although the spectrum of the sample before Ar-ion sputtering was also obtained (Fig. 5), it is highly possible that artifacts, such as the adsorption of impurities, produced during the sample transfer process might have affected the spectra of the upper surface. Therefore, here we discuss the XPS spectra only for the Ar-ion sputtered samples, in which the surface newly obtained after sputtering was only briefly exposed to high vacuum condition before the measurements. For both the Li-1s and O-1s spectra, the intensity of the peaks assignable to Li_2O and LiOH (and/or Li_2CO_3) increased with increasing C_{H2O}. In the Li-1s spectrum, the peak corresponding to metallic Li decreased with the increase of C_{H2O}. The dependence of the Li composition on C_{H2O} was further investigated by deconvoluting the O-1s spectra. Specifically, the O-1s spectrum was analyzed, as the peaks assignable to Li_2O and LiOH (and/or Li_2CO_3) in the O-1s spectra were more clearly separated compared to those in the Li-1s spectra. Fig. 6(a) and (b) show the depth profiles of Li_2O and LiOH (and/or Li_2CO_3) at various C_{H2O}. When the C_{H2O} was increased from 14 to 786 ppm, Li_2O was the main product. In contrast, the formation of LiOH (and/or Li_2CO_3) was predominant when the C_{H2O} was further increased to 3770 ppm. To separate the contribution from LiOH and Li_2CO_3, the depth profile of Li_2CO_3 at various C_{H2O} was also obtained by deconvoluting C-1s

XPS spectra (Fig. 7). When C_{H2O} was increased beyond 1000 ppm, the amount of Li_2CO_3 increased less steeply compared to that of LiOH (and/or Li_2CO_3) shown in Fig. 6(b). It should be also noted that the composition ratio of LiOH, which was estimated by subtracting the contribution of Li_2CO_3, was more than three times larger than that of Li_2CO_3 in the whole depth range measured. Considering these results, LiOH was considered to be the dominant reaction product in $C_{H2O} > 1000$ ppm. Thus, the XPS results indicated that metallic Li was converted to Li_2O and LiOH in the presence of H_2O in the electrolyte, and that the formation of LiOH was dominant when the C_{H2O} exceeded 1000 ppm. It was confirmed that the tendency was reproducible in three repetitive experiments.

In general, the morphology of electrodeposits is closely correlated with the effective surface area that physically contacts the electrolyte. In addition, decomposition of the electrolyte induced by physical contact with Li deposits can be detrimental to cycle performance [1, 2, 21, 27, 28]. Therefore, subsequent morphological examination of the Li deposits formed in LiFSI-TEGDME was performed by SEM (Fig. 8). On average, seven to ten images were acquired per sample. Angular Li deposits that ranged in size from a few μm to a few tens of μm were observed for the sample prepared in electrolyte with a C_{H2O} of 26 ppm (Fig. 8(a) and (b)). As the C_{H2O} increased to ~1000 ppm, the deposits adopted a spherical shape with an average diameter of 5 μm (Fig. 8(c)). Li dendrites were also observed at this concentration range of contaminant H_2O (Fig. 8(d)). When the C_{H2O} exceeded 1000 ppm, larger aggregates were formed, and the aggregates appeared to be physically compressed by a PP separator (Fig. 8(e)-(g)). In general, Li nucleation and growth can occur progressively throughout the electrode surface at different rates on individual nuclei [29-31]. In addition, due to the heterogeneity of the thickness and the chemical composition of SEI, the concentration of Li-ion flux occurs in several nuclei [1, 27]. For these reasons, we speculated that Li deposits with quite different morphologies and sizes were observed even in the presence of the same amount of H_2O. It should be also noted that the results were reproducible in three to four repetitive experiments.

The effects of C_{H2O} on the CE of Li deposition/dissolution reactions are schematically summarized in Fig. 9. At C_{H2O} values of <1000 ppm, the CE increased to ~80%, suggesting that the formation of Li_2O is a key factor for the increase in CE at this C_{H2O} range. Consistent with this speculation, several reports have revealed that Li_2O partially contributes to the reversibility of Li deposition and dissolution [13, 27, 32-34]. Notably, however, the CE decreased at C_{H2O} > 1000 ppm. As the formation of LiOH, which is a reaction product between Li and H_2O, also markedly increased at this C_{H2O} range, the CE appears to decrease with increased formation of LiOH. This finding is consistent with the fact that LiOH is an unfavorable component due to the high resistivity of LiOH for Li ion conduction [1, 2, 5, 35]. The present SEM analysis also confirmed that local Li deposition was significantly accelerated at C_{H2O} > 1000 ppm, an observation that may also be attributable to the formation of excessive LiOH within the SEI. The existence of a resistive LiOH layer is predicted to hinder the homogeneous distribution of Li-ion flux followed by local Li deposition, leading to the breakdown of the SEI layer. This process would also promote the growth of Li dendrites accompanied with the further consumption of Li metal through contact with the electrolyte, resulting in the lower CE [1, 27].

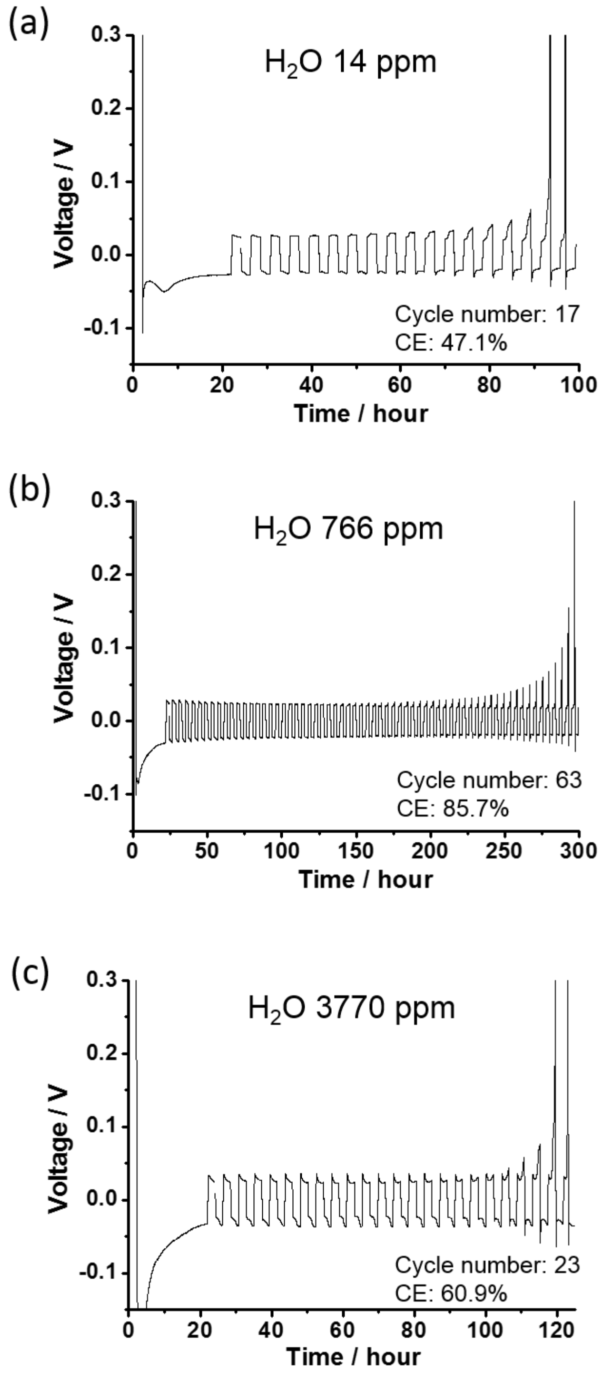

Fig. 1. Voltage vs. time profiles for 1 M LiFSI-TEGDME containing C_{H2O} of (a) 14 ppm, (b) 766 ppm and (c) 3770 ppm.

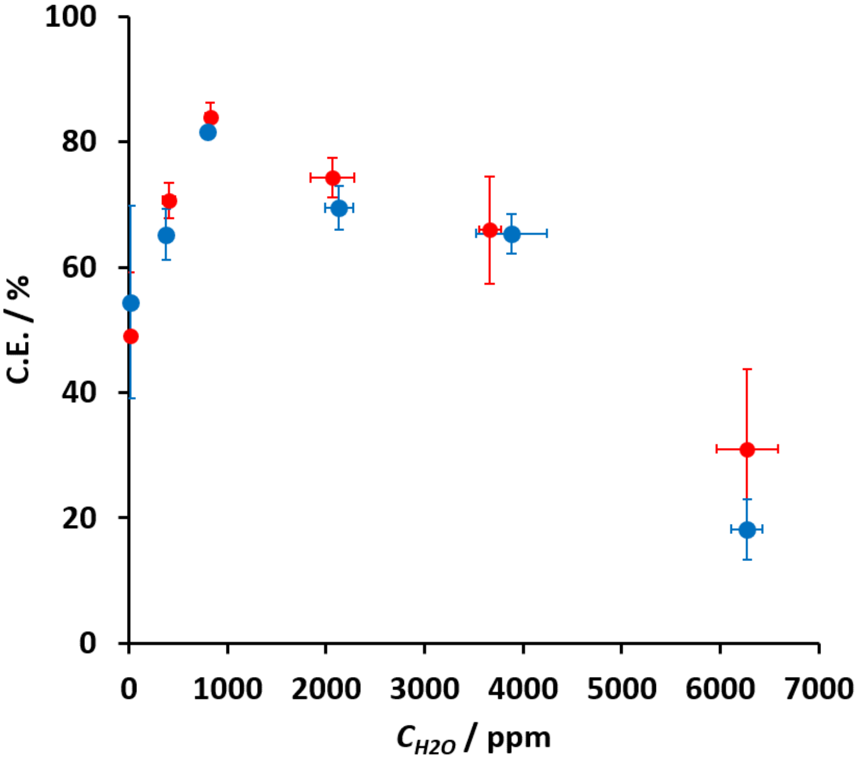

Fig. 2. Relationships between the CE and C_{H2O} obtained from a series of 1 M LiFSI-TEGDME (red circles) and 1 M LiTFSI-TEGDME (blue circles).

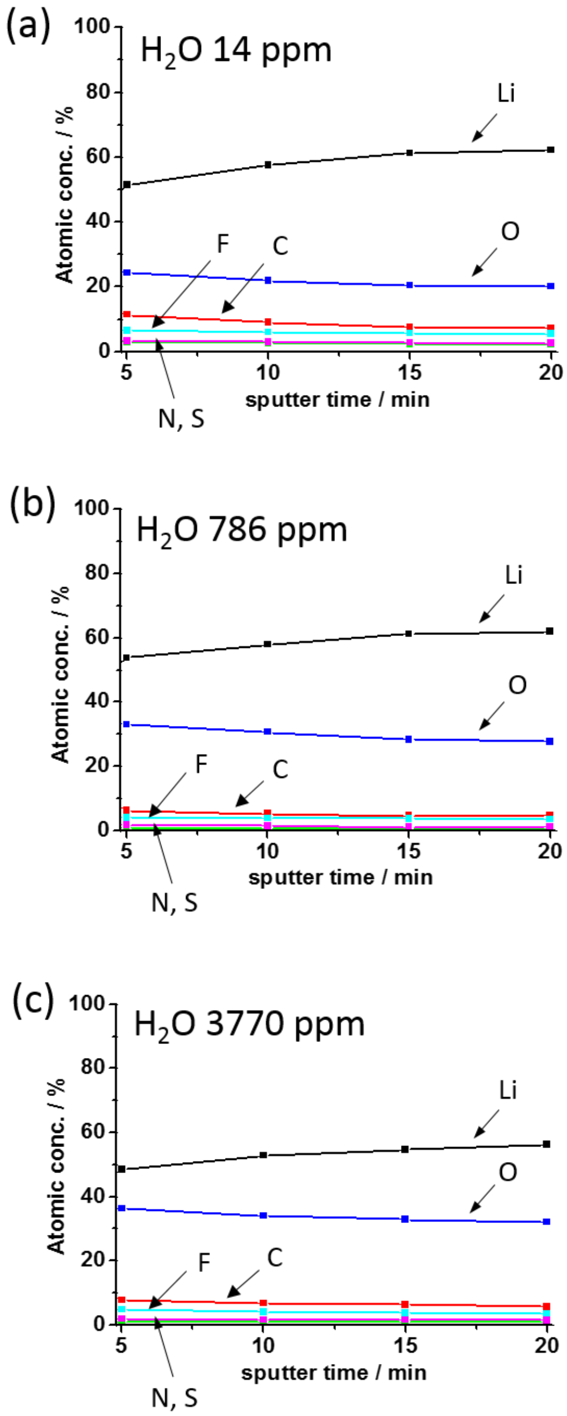

Fig. 3. Depth profiles of the element ratio for electrodeposited lithium obtained in 1 M LiFSI-TEGDME with C_{H2O} of (a) 14 ppm, (b) 786 ppm and (c) 3770 ppm. All data were obtained after the initial Li deposition.

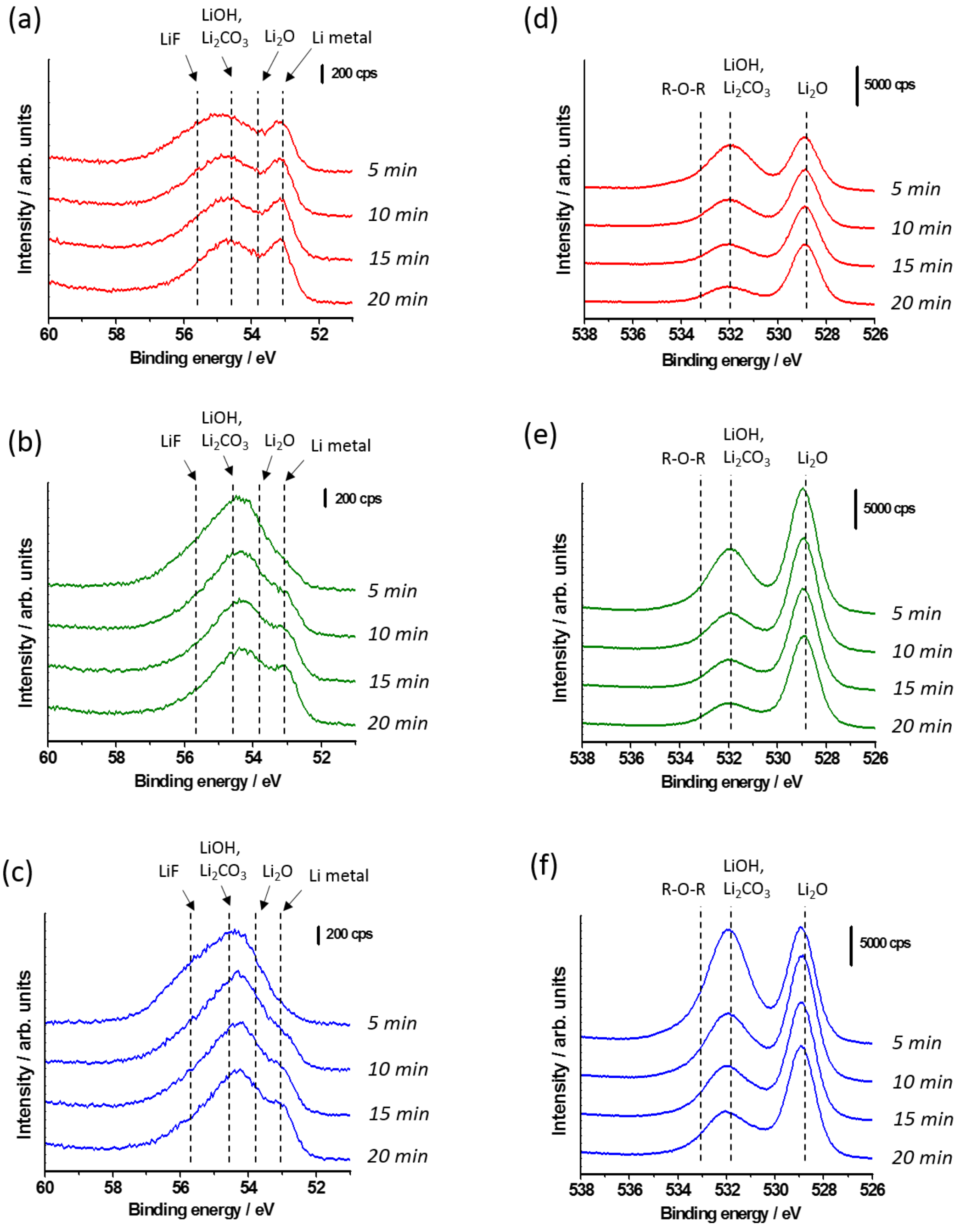

Fig. 4. (a)-(c) Li-1s XPS spectra and (d)-(f) O-1s XPS spectra obtained for 1 M LiFSI-TEGDME with 14, 786 and 3770 ppm C_{H2O}. All data were obtained after the initial Li deposition.

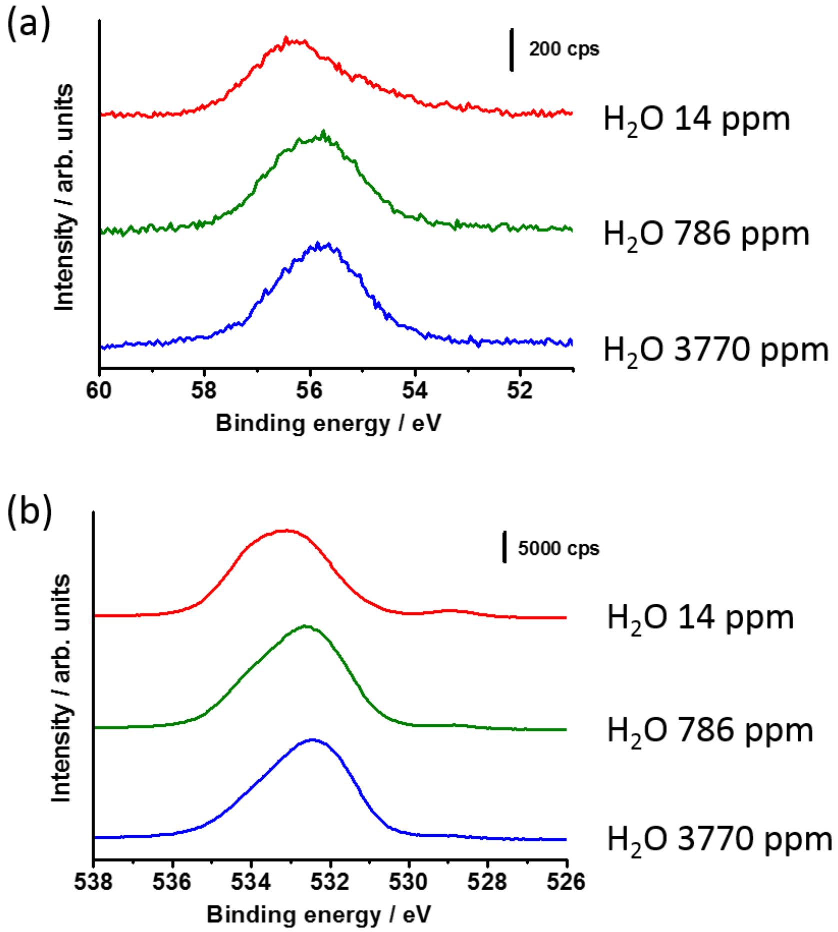

Fig. 5. (a) Li-1s and (b) O-1s XPS spectra in 1 M LiFSI-TEGDME with 14, 786 and 3770 ppm C_{H2O} obtained before Ar-ion sputtering. All data were obtained after the initial Li deposition.

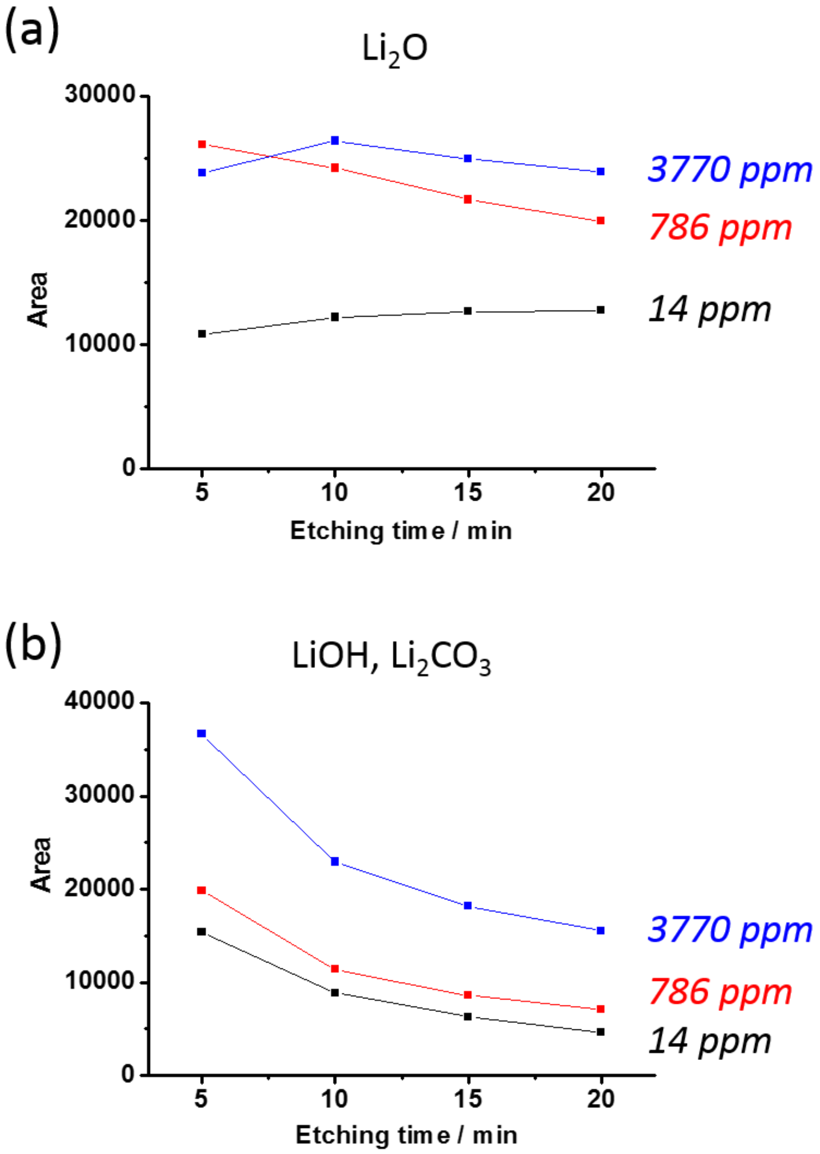

Fig. 6. C_{H2O} dependence of depth profiles of the peak areas assigned to (a) Li_2O and (b) LiOH and/or Li_2CO_3. Both profiles were obtained from the O 1s XPS spectra.

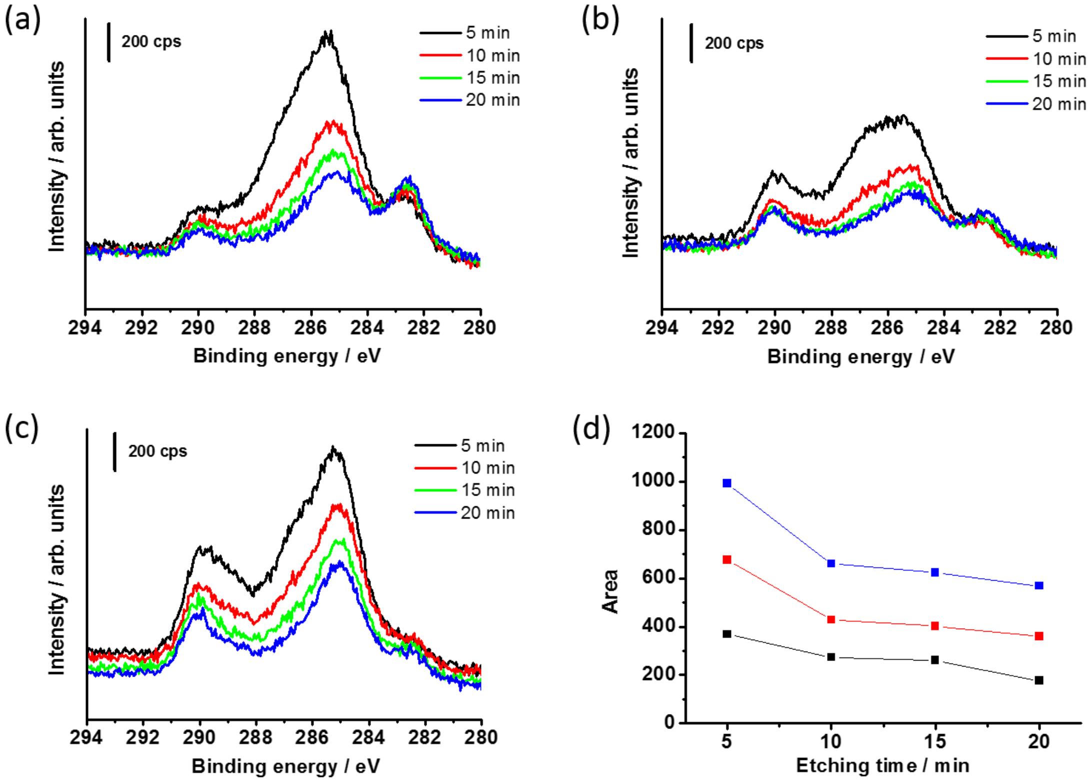

Fig. 7. C-1s XPS spectra in 1 M LiFSI-TEGDME with C_{H2O} of (a) 14 ppm, (b) 786 ppm and (c) 3770 ppm. (d) C_{H2O} dependence of the depth profile of the peak area assigned to Li_2CO_3, which was obtained from the C 1s XPS spectra. All data were obtained after the initial Li deposition.

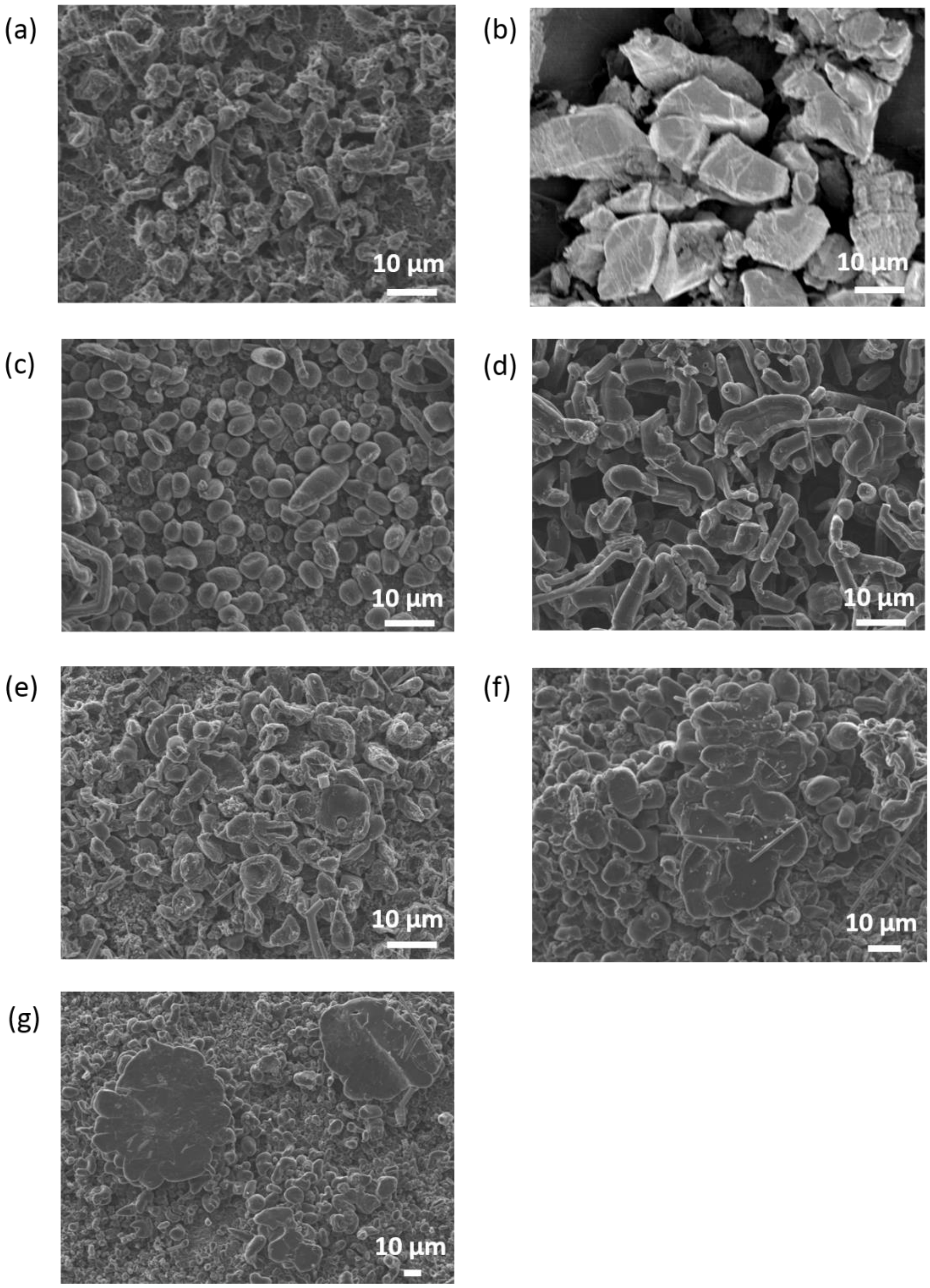

Fig. 8. SEM images of Li deposits on Ni substrates obtained for 1 M LiFSI-TEGDME with C_{H2O} at (a)-(b) 26 ppm, (c)-(d) 786 ppm, (e) 3780 ppm and (f)-(g) 6270 ppm. All images were captured after the initial Li deposition.

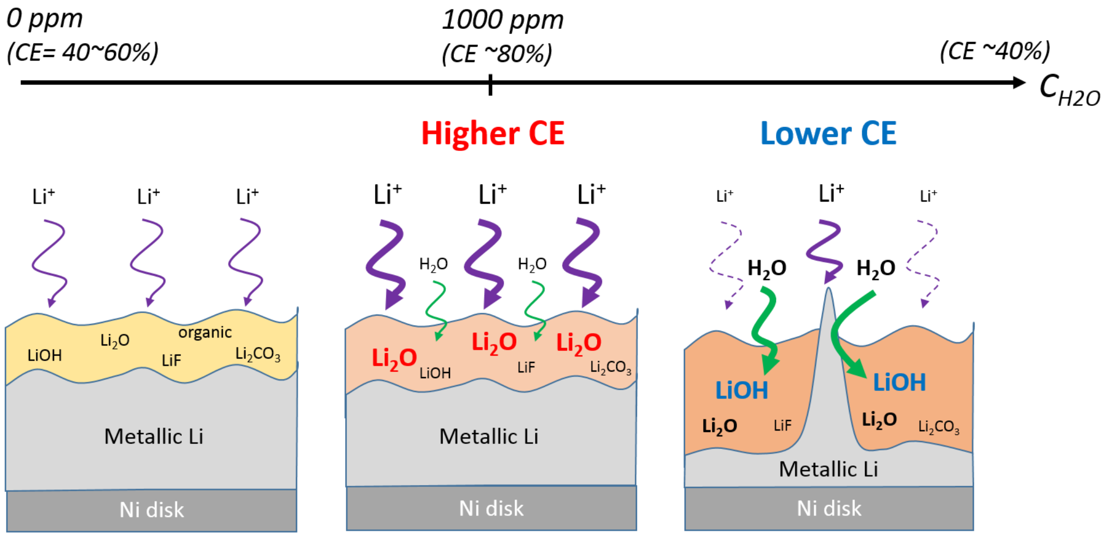

Fig. 9. Schematic illustration of the C_{H2O} dependence of the CE associated with the chemical composition of Li deposits.

	As prepared	After 24-h storage
with Li metal	776 ppm	764 ppm
without Li metal	776 ppm	732 ppm

Table 1. The C_{H2O} change in 1 M LiFSI-TEGDME during a 24-h storage at room temperature in the presence and absence of metallic-Li foil. The H_2O content was determined by Karl Fischer titration.

	Li 1s	O 1s	C 1s
Li metal	53.0 ± 0.2	-	-
Li_2O	53.7 ± 0.2	528.8 ± 0.2	-
LiOH	54.6 ± 0.2	531.8 ± 0.2	-
Li_2CO_3	54.6 ± 0.2	531.8 ± 0.2	290.1 ± 0.2
LiF	55.6 ± 0.2	-	-

(The unit is eV)

Table 2. Peak positions of lithium compounds used for the XPS peak-fitting. Full width at half maximum was also fixed in the range of 0.6~1.2 eV for metallic Li and 1.0~2.3 eV for other compounds.

2.1.4. Conclusion

In an attempt to compare the characteristics for the half-cell Li deposition/dissolution reactions, we examined the C_{H2O} dependence of the CE of Li deposition/dissolution reactions in tetraglyme-based electrolytes. The CE ranged between 40% and 60% in 1 M LiFSI-TEGDME in the presence of unavoidable contaminant H_2O (~30 ppm), but increased to ~80% as the C_{H2O} was increased to 1000 ppm. The increase in CE was associated with a sharp increase in the amount of Li_2O in the Li deposits. Notably, however, when the C_{H2O} in the electrolyte exceeded 1000 ppm, the CE decreased and the proportion of LiOH in the Li deposits drastically increased. In addition, the Li deposits formed aggregates and were locally distributed in this C_{H2O} range. Taken together, these findings suggest that the formation of a resistive LiOH layer induced local Li deposition, which was followed by the breakdown of the SEI and the further consumption of Li, resulting in the lower CE. The bifurcation point at which the CE began to fall occurred at a C_{H2O} of ~1000 ppm in the present system. Although this point may shift depending on the surface roughness of the electrode, the qualitative relationship observed here between CE and C_{H2O} is expected to be universal for closed cell systems.

2.2. Utilization of contaminant water as the additive enhancing the charge/discharge performance in Li-air batteries

2.2.1. Introduction

The results obtained in 2.1. mean that optimized amount of water can be used as an additive enhancing the reversibility of Li deposition-dissolution reactions at a Li negative electrode. This knowledge is useful to reduce the cost of designing Li-air batteries because the requirement for the equipment which prevents the contamination of air components, such as a separator, can be relaxed. In the next step, the applicability of this knowledge to an air cathode (a positive electrode) is of great importance.

Several attempts have been made to examine the influence of water on the charge-discharge reactions at an air cathode [2-11]. These studies reveal that the battery performance in the presence of water is highly dependent on the electrocatalysts as well as the concentration of water (C_{H2O}). Notably, if the electrocatalysts and water synergistically function, batteries with surprisingly high round trip energy efficiency (around 90%) can be realized, associated with the formation of LiOH instead of Li_2O_2 as the main discharge product [9-11]. However, novel metals or high cost elements are employed as electrocatalysts in these studies. One promising strategy to develop cost-effective catalysts for an air cathode in the presence of water is to learn from the catalysts for oxygen reduction or oxygen evolution reactions (ORR or OER) in aqueous media. The breakage and the formation of double bonds of molecular oxygen can be efficiently proceeded on the ORR and OER catalysts, which is indispensable to realize the reversible discharge-charge reactions via the formation and the decomposition of LiOH. Indeed, Lee *et al*., reported that the electron number for ORR in non-aqueous media was increased from one to four on the efficient aqueous ORR electrocatalyst (carbon-conductive polymer-silver) by increasing the water content up to 5000 ppm [36].

Natural systems are appropriate to learn the design principle of the cost-effective ORR catalysts. In living cells, Cu-containing enzymes, such as laccase and bilirubin oxidase, catalyze the four-electron ORR for respiration with lower overpotential than Pt [37–39]. In these enzymes, modulation of the electronic state of the central Cu by coordination with N atoms is believed to be a key factor for the high catalytic activity [40, 41]. For this reason, numerous studies have described the synthesis of Cu- based complexes with N-ligation that mimic Cu-enzymes [42-48]. For example, a dinuclear Cu complex of 3,5-diamino-1,2,4-triazole (Cu-DAT) supported on carbon black exhibited an onset potential of 0.73 V (vs. RHE) at pH 7 for the ORR, which is the highest value among Cu-based catalysts reported to date [43, 49]. Although Cu-DAT is therefore a promising platform for the development of low-cost ORR catalysts, its half-wave potential for the ORR decreased by about 140 mV after 100 cycles of cyclic voltammograms (CVs) [43]. Thus, for the practical application of this catalyst, it is necessary to improve its stability. We recently reported that stable graphene materials with Fe-N coordination bonds can be synthesized by the short-duration heat treatment (< 60 s) of graphene oxides in the presence of an Fe–pentaethylenehexamine complex [50, 51]. Notably, the use of the short-duration heat treatment improved the stability of the prepared catalyst while maintaining Fe-N coordination. For these reasons, it is worth investigating whether this synthesis method can be applied to Cu-DAT, which exhibits the highest performance among Cu-based complexes [43], and also the applicability of the catalyst to an air cathode material in aprotic Li-air batteries.

2.2.2. Experimental

2.2.2.1. Synthesis of electrocatalysts for aqueous ORR

Reduced graphene oxides (r-GOs) were synthesized through the heat treatment (900 °C) of graphene oxides under an inert atmosphere, as detailed in our previous report [52]. It should be noted here that no metal residue was observed in the resulting r-GOs from X-ray photoelectron spectra. $CuCl_2 \cdot 2H_2O$ (114 mg; Wako) and 3,5-diamino-1,2,4-triazole (132 mg; TCI) were dissolved in 10 ml ultra pure water to form Cu-DAT complex in solution. A total of 200 mg r-GOs was added to 9.14 ml of the Cu-containing aqueous solution, and the resulting mixture was dried. The obtained material was placed at the bottom of a half-closed quartz tube filled with argon and quickly inserted into a muffle furnace preheated to 900 °C. After heat treatment for 45 s, the tube was quickly removed from the furnace and immediately cooled under argon flow. The synthesized material was washed with 2 M H_2SO_4 at 60 °C for 3 h. The resulting catalyst was designated HT/Cu-DAT (HT: Heat treatment). The Cu-DAT complex supported on r-GOs (non-HT/Cu-DAT) was prepared on the basis of previous paper [43], except for the use of r-GOs as carbon supports. 20wt% Pt/C (Fuel Cell Earth) was also used as a reference sample.

2.2.2.2. Electrochemical measurements for aqueous ORR

Oxygen reduction activities were evaluated using a rotating ring-disk electrode (RRDE) in a 0.1 M phosphate-buffer solution containing 0.5 M $NaClO_4$ (pH 7.0). The counter electrode was a titanium wire. A Ag/AgCl/KCl sat. was used as the reference electrode and was calibrated with respect to a reversible hydrogen electrode (RHE = Ag/AgCl/KCl sat. + 0.198 V + 0.0591 x pH at 25 °C). Working electrodes were first prepared by dispersing 5 mg of each catalyst in 437.5 μl ethanol and 47.5 μl of 5 wt% Nafion solution (Aldrich). The resulting catalyst inks were dropped in 2.5-μl aliquots onto a glassy carbon electrode (0.196 cm^2). Therefore, the amounts of loaded catalyst and Nafion were controlled to be approximately 0.13 mg/cm^2 and 0.06 mg/cm^2, respectively. The number of electrons was evaluated by using a RRDE and calculated based on the Eq. (1) [50].

$$n = \frac{4 \times I_d}{I_d + I_r/N} \qquad (1)$$

in which N (= 0.41), Id and Ir are the collection efficiency, disk current and ring current, respectively. The poisoned potential on the Pt ring was 1.2 V versus RHE. We also estimated the number of electrons from the Koutecky-Levich equation as follows:

$$\frac{1}{j} = \frac{1}{j_k} + \frac{1}{B\omega^{1/2}} \qquad (2)$$

where j is the measured current, jk is the kinetic-limiting current and ϖ is the electrode rotation rate. The theoretical value of the Levich slope (B) was evaluated from the following relationship:

$$B = 0.62nFCD^{2/3}v^{-1/6} \qquad (3)$$

where n is the number of electrons, F is the Faradic constant (96485 C/mol), C is the bulk concentration of oxygen (1.13 x 10^{-6} mol/cm^3), D is the diffusion coefficient of oxygen (1.8 x 10^{-5} cm^2/s), and v is the viscosity of the electrolyte (0.01 cm^2/s). The stability of catalysts was also evaluated using a rotating disk electrode (RDE). Rotation speed and scan rate were set at 1500 rpm and 250 mV/s, respectively, during 1000 CVs.

2.2.2.3. Preparation of electrolytes and an air cathode for aprotic Li-air batteries

Lithium bis(trifluoro methanesulfonyl)imide (LiTFSI; Kishida Chemical Co., Ltd.) was dissolved in tetraethylene glycol dimethyl ether (TEGDME; Kishida Chemical Co., Ltd.) to prepare 1 M LiTFSI-TEGDME under a dry atmosphere. LiTFSI was used as received without further purification and TEGDME had been dehydrated with molecular sieve 3A 1/8 (Wako Pure Chemical Industries, Ltd.). Various concentration of water was also introduced into the as-prepared electrolyte to obtain the electrolyte with contaminant water. The water content of the electrolytes was determined by Karl Fischer titration (CA-21, Mitsubishi Chemical Analytech).

For the preparation of an air cathode, the carbon substrate of HT/Cu-DAT was replaced with Ketchen Black EC600JD (KB; Lion Corp.) to minimize the difference in the specific surface area between the studied catalyst (HT/Cu-DAT_KB) and the KB-only material (as a control sample). Both materials were intimately mixed with polytetrafluoroethylene (PTFE, 60 wt %) in a polyvinylpyrrolidone (PVP, 5 wt %) solution, and the resulting slurry was coated on carbon paper (TGP-H-060, Torray) with a material loading density of 1.0 mg/cm^2. The coated electrode was dried for 12 h at 110 °C under vacuum to remove residual solvent and then used as an electrode.

2.2.2.4. Electrochemical measurements for aprotic Li-air batteries

The batteries were assembled in an Ar-filled glovebox with a water content of less than 1 ppm. The cell consisted of metallic Li foil (19.5 mm diameter, 0.4 mm thickness; Honjo Metal Co., Ltd.) and an catalyst-loaded carbon paper as a gas diffusion electrode (19.5 mm diameter). Glass fiber (Whatman GF-A, 24 mm diameter) was used to separate the negative and positive electrode. 300 μL solution of 1 M LiTFSI-TEGDME or 1 M LiTFSI-TEGDME with contaminant water was used as an electrolyte. A gas tank filled with oxygen gas at the pressure of 0.2 MPa was mounted to the cathode side of the cell to supply enough amount of oxygen during the cycles. Charging and discharging of batteries was conducted using VMP3 Biologic Instrument in a current-controlled mode.

2.2.2.5. Characterization

Hard X-ray absorption measurements (XAFS) were performed using the hard X-ray beam line 01B01 at SPring-8, Japan. Transmission yield spectra were acquired using a double-crystal Si (111) monochrometer. X-ray photoelectron spectroscopy (XPS) analyses (Axis Ultra, Kratos Analytical Co.) were obtained using monochromated Al Kα X-rays at hν = 1486.6 eV.

2.2.3. Results and discussion

2.2.3.1. Characterization and evaluation of aqueous ORR electrocatalysts

Cu K-edge extended X-ray absorption fine structure (EXAFS) analyses were first conducted to confirm that Cu-N coordination bonds remained in HT/Cu-DAT. Fig. 1 shows the Fourier transformation of k^3-weighted EXAFS oscillation for HT/Cu-DAT, Cu phthalocyanine and Cu foil. The EXAFS spectra for HT/Cu-DAT and Cu phthalocyanine displayed peaks derived from the first coordination sphere at R = 1.43 Å and 1.50 Å, respectively, which were assignable to Cu-N bonds. The coordination number for N atoms was estimated to be 1.7 in HT/Cu-DAT. Cu foil had a peak corresponding to the first coordination sphere at R = 2.16 Å, which was ascribed to Cu-Cu bonds. Importantly, this peak was not observed for HT/Cu-DAT. In contrast, the EXAFS spectrum for the heat treated sample without the acid treatment (Fig. 2) shows both the Cu-N and Cu-Cu peaks. These results indicate that a certain portion of Cu-N bonds in Cu-DAT precursors indeed kept intact after the short-duration heat treatment, although the other Cu-N bonds were broken and aggregated as metallic Cu nanoparticles, which were removed through the acid treatment.

The catalytic activity of HT/Cu-DAT was compared to those of non-HT/Cu-DAT and 20wt% Pt/C by measuring current density (*j*) vs. potential (*U*) relationships in neutral solutions (Fig. 3: the curves in oxygen and argon, Fig. 4(a): the subtracted curves). From the curves, it was determined that HT/Cu-DAT generated a cathodic current with an onset potential (Uonset: the potential value corresponding to a cathodic current of -10 μA/cm^2) of 0.79 V and exhibited the catalytic activity comparable to that of non-HT/Cu-DAT. Note that the *U*onset of non-HT/Cu-DAT is essentially identical to the value which was previously reported [43]. To our knowledge, although the ORR activity is still lower than that of Pt/C (*U*onset for Pt/C was 1.02 V vs RHE), the onset potential (0.79 V) of HT/Cu-DAT is the highest value reported to date among Cu-based ORR catalysts in neutral solutions. The number of electrons for HT/ Cu-DAT was estimated from the yield of H_2O_2 to be approximately four over the entire potential range (Fig. 4(b)), which essentially coincides with the results of the Koutecky-Levich plots (Fig. 5). These results indicate that most dioxygen molecules would be reduced to water via a four-electron transfer pathway. We also measured the ORR activities in 0.5 M $NaClO_4$ without phosphate buffer as shown in Fig. 6, which shows that the slopes of the *j* vs *U* curves near the onset potential were much gentler than those in buffer solutions. This is likely because the local pH at electrode surfaces increased due to the consumption of proton by the ORR [53].

To evaluate the stability of HT/Cu-DAT, *j* vs. *U* curves were measured before and after 1000 CVs and compared with those of non-HT/Cu-DAT (Figs. 7(a) and (b)). Although the absolute current density value in the kinetic region (0.6 V vs. RHE) [54] after the CV cycling decreased by 81% (-0.72 to -0.14 mA/cm^2) for non-HT/Cu- DAT, it decreased only by 6% (-0.87 to -0.82 mA/cm^2) for HT/Cu- DAT (Fig. 7(c)). These results indicate that the stability of HT/Cu-DAT was enhanced by the heat treatment.

The elemental compositions of both catalysts before and after 1000 CV cycles were estimated by XPS analyses. Cu/C and N/C ratios before performing the CV cycles are presented in Table 1. After 1000CV cycles, the Cu and N contents of non-HT/Cu-DAT decreased by 75% and 67%, respectively, whereas those of HT/Cu-DAT decreased only by 10% and 4%, respectively, as shown in Figs. 7(d) and (e). This finding clearly demonstrates that the desorption of Cu and N atoms was reduced in HT/Cu-DAT compared to non-HT/Cu-DAT. Thus, the observed deterioration of ORR activity (kinetic current densities) after 1000 CV cycles (Figs. 7(a) and (b)) corresponds to the decreased Cu and N content, indicating that the suppression of Cu and N atom desorption improves the stability of HT/Cu-DAT. Trial to achieve further improvement of the catalytic stability for practical use is under progress.

To investigate why the desorption of Cu and N was suppressed in HT/Cu-DAT, the electronic states of N atoms in HT/Cu-DAT and non-HT/Cu-DAT determined from N-1s XPS spectra were characterized and compared (Fig. 8). The N-1s XPS spectrum of HT/Cu-DAT can be deconvoluted into five peaks: pyridine-like N at 398.5 ± 0.2 eV, N atoms in the triazole ring or pyrrole-like N at 399.7 ± 0.2 eV, amine N bonded to the triazole ring at 400.4 ± 0.2 eV, graphite-like N at 401.0 ± 0.2 eV, and nitrogen oxide at 404.0 ± 0.2 eV [55–59]. The ratios of these components in HT/Cu-DAT were determined and are presented in Table 2(a). The total amount of pyridine-like N, pyrrole-like N and graphite-like N exceeded at least 65% of all N atoms in HT/Cu-DAT. Taken together, the XPS and EXAFS results suggest that N atoms coordinated to Cu atoms were doped into the graphene network during the heat treatment (Fig. 9(a)). Thus, the anchoring of active Cu-sites into the graphene substrate through the covalent and coordination bonds resulted in the suppression of desorption of the active sites from electrodes [60]. In contrast, for non-HT/Cu-DAT, the peaks corresponding to N atoms in the triazole ring and amine N bonded to the triazole ring were observed at 399.5 ± 0.2 eV and 400.4 ± 0.2 eV, respectively [61–64]. The ratios of these components in non-HT/Cu-DAT are presented in Table 2(b). The XPS result suggests that Cu-DAT was only physically adsorbed onto r-GOs (Fig. 9(b)).

Let us discuss the ORR activity of HT/Cu-DAT. Thorum and colleagues reported that the closely spaced Cu centers in non-HT/Cu-DAT were essential for its high catalytic activity [43].

Kato *et al*. also suggested that the dinuclear Cu centers in non-HT/Cu-DAT activated dioxygen molecules [49]. Considering that molecular structures of precursors are retained in the resultant catalyst by the short-duration heat treatment, as demonstrated in our previous paper [50], we can speculate that the closely spaced Cu centers of non-HT/Cu-DAT remained in HT/Cu-DAT to some extent and worked as the active sites for the ORR. Another possible explanation for the high ORR activity of HT/Cu-DAT is that the heat treatment improved the electronic interaction between the active sites and the graphene substrate due to the introduction of active sites into graphene sp2 networks. This assumption was supported by the N-1s XPS spectrum in Fig. 8 (doping of N atoms) and was reported in a number of previous reports [65, 66]. Further studies for identifying the molecular structure and the ORR mechanism are now in progress in our laboratory.

2.2.3.2. Application of the electrocatalyst for aqueous ORR to an air cathode material of aprotic Li-air batteries

Fig. 10 shows the discharge-charge curves obtained when KB or HT/Cu-DAT_KB was used as a cathode material and 1 M LITFSI-TEGDME with or without additional water was used as an electrolyte. The curves obtained for both cathode materials were also compared in Fig. 11. The water content of the electrolyte without adding water was calculated to be 25 ppm by Karl Fischer titration. The cell without the catalyst and additional water (the cell for a control experiment) cycled without significant deterioration for less than 20 cycles, which coincides with the reported results. Regardless of the water content, the cells with HT/Cu-DAT_KB catalyst exhibited the lower overvoltage during the charge in the first few cycles. However, this effect diminished after 5th cycle and all the four cells started to degrade significantly after 20th cycle. Although additional water did not affect the battery performance considerably, some distinctive behavior was observed during the discharge only in the presence of additional water (Fig. 12).

From 2nd to 6th cycle, the cell voltage drastically decreased around 2.6 ~ 2.7 V in the beginning of the discharge, and then it gradually increased until the end of the discharge, but this characteristic disappeared after 7th cycle. This phenomena is supposed to be originated from the reactions involving water. The formation of LiOH by the reactions between Li_2O_2 and H_2O is thermodynamically unfavorable ($Li_2O_2 + 2H_2O \rightarrow 2LiOH + H_2O_2 \quad \Delta G = +41$ kJ/mol). Indeed, it has been reported that LiOH can be considerably formed only in the presence of the proper electrocatalysts [9-11]. Thus, it is difficult to identify the main discharge product only from these electrochemical data. It is also possible that the solution-mediated growth of Li_2O_2 was induced in the presence of water. Aetukuri *et al.*, reported that the Li_2O_2 formation by the solution-mediated pathway proceeds at lower voltage compared to that by the surface electrochemical pathway in a voltage range of 2.4 ~ 2.7 V [7]. The possibility that H_2O_2 was formed simply by a parasitic electrochemical/chemical reaction, $O_2- + H_2O + e- \rightleftharpoons O_2H- + OH-$ ($U_{H2O2} = 2.6$ V), cannot be also denied [7]. The disappearance of these characteristics with increasing cycle number is thought to be derived from the consumption of water through the reactions with both electrodes and the electrolyte. The reason why the cycle life of all the four batteries was almost the same despite the observation of the distinct features for each catalyst is at present unclear. Further studies such as the investigation of the water-content dependency and the identification of the discharge product may clarify the detailed mechanism.

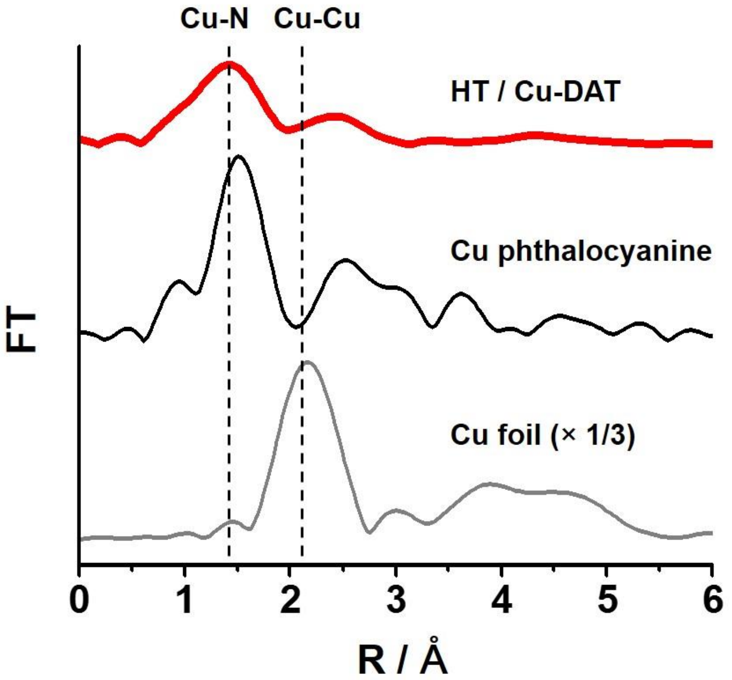

Fig. 1. Fourier transformation (FT) of k^3-weighted EXAFS oscillation for heat-treated (HT)/Cu-DAT after the acid treatment (red), Cu phthalocyanine (black) and Cu foil (gray).

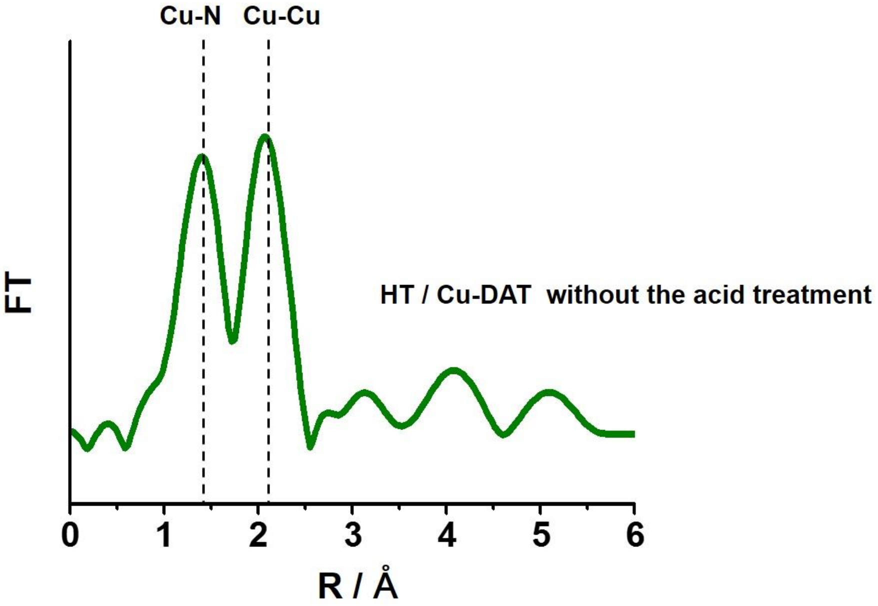

Fig. 2. Fourier transformation (FT) of k^3-weighted EXAFS oscillation for HT/Cu-DAT without the acid treatment.

(a) HT/Cu-DAT

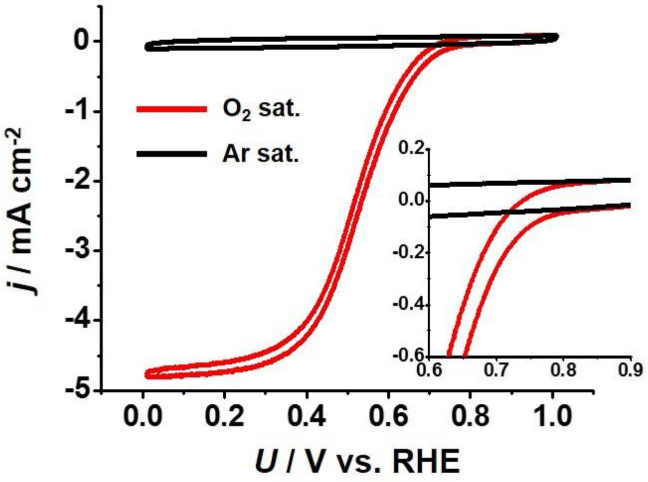

(b) non-HT/Cu-DAT

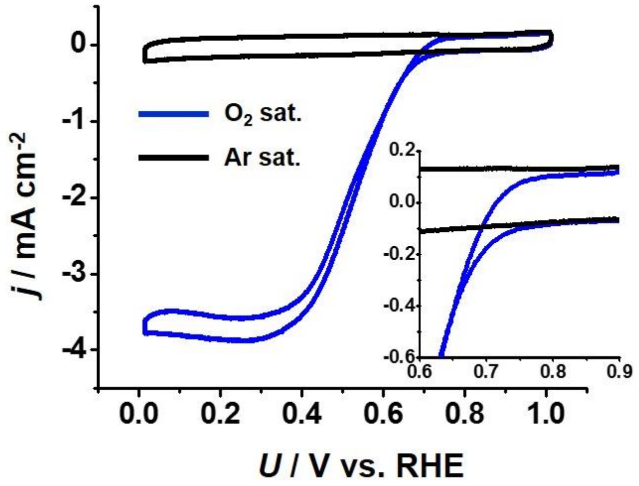

Fig. 3. j vs. U curves for (a) HT/Cu-DAT and (b) non-HT/Cu-DAT in 0.1 M phosphate buffer solution (pH = 7.0) saturated with oxygen ((a) red, (b) blue) or with argon (black). Rotation rate: 1500 rpm; scan rate: 10 mV/s. The insets show magnified curves.

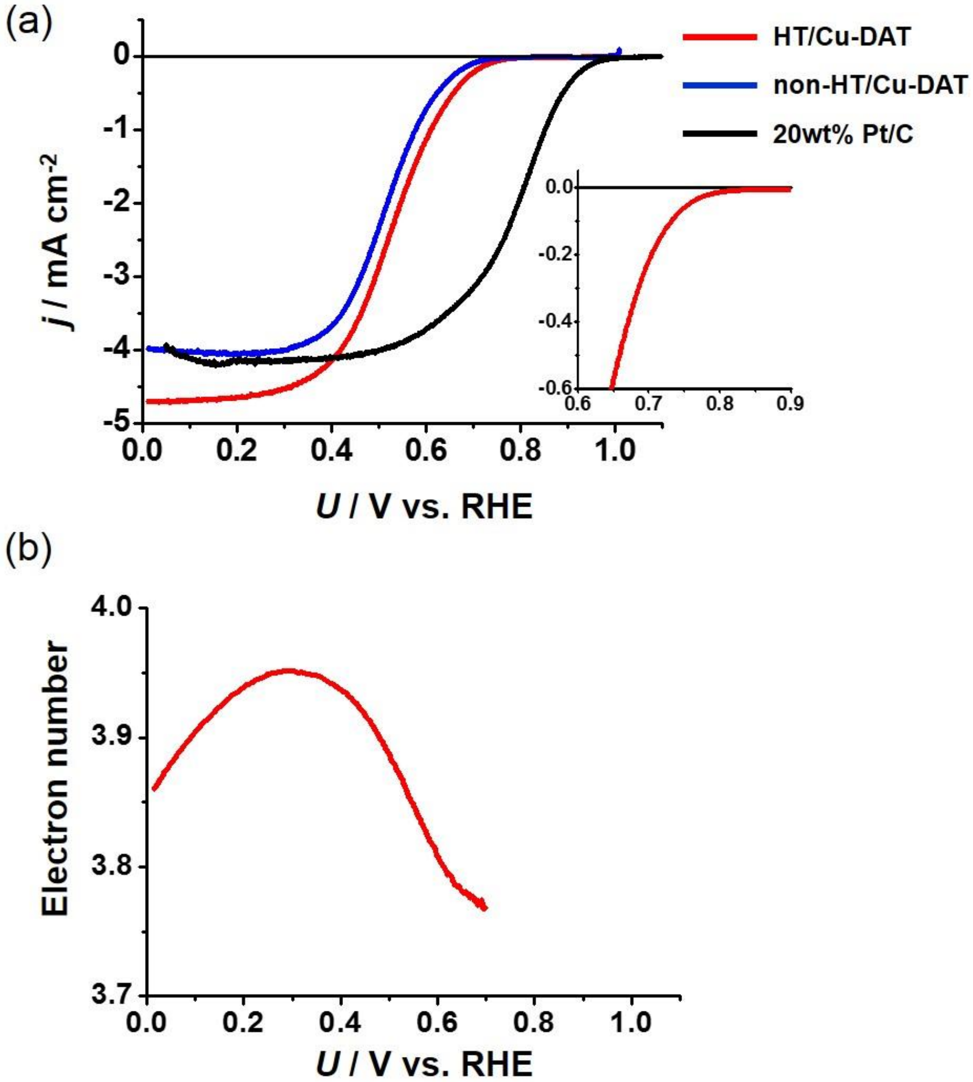

Fig. 4. (a) *j* vs. *U* curves for HT/Cu-DAT (red) and non-HT/Cu-DAT (blue) in 0.1 M phosphate buffer solution (pH = 7.0). The inset shows the magnified curve for HT/ Cu-DAT. These curves were obtained by subtracting the cyclic voltammetries (CVs) in argon-saturated electrolyte solution from those obtained in O_2-saturated electrolyte solution. (b) Electron number for HT/Cu-DAT. Rotation rate: 1500 rpm; scan rate: 10 mV/s.

(a) HT/Cu-DAT

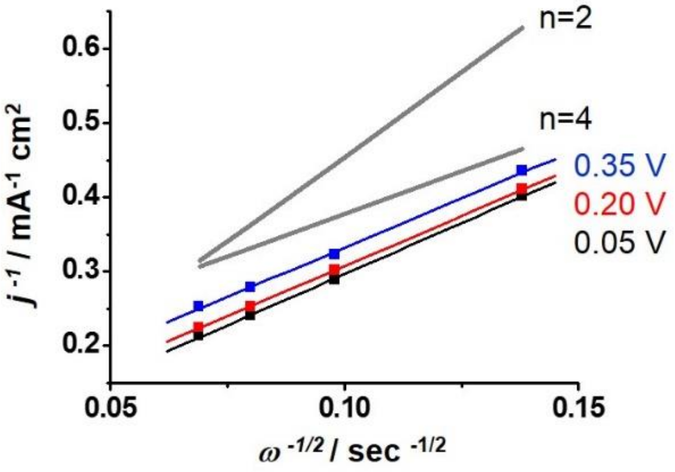

(b) non-HT/Cu-DAT

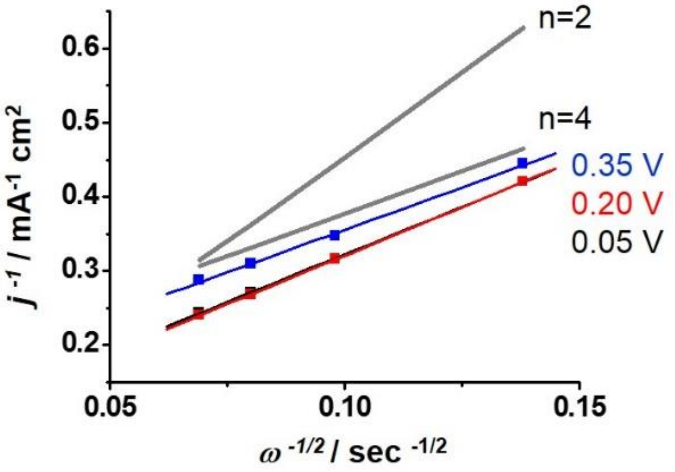

Fig. 5. Koutecky-Levich plots for (a) HT/Cu-DAT and (b) non-HT/Cu-DAT at 0.05 V (black), 0.20 V (red) and 0.35 V (blue) vs. RHE. For comparison, the theoretical slopes (gray line) for the ORR with two- and four-electron transfers are also shown.

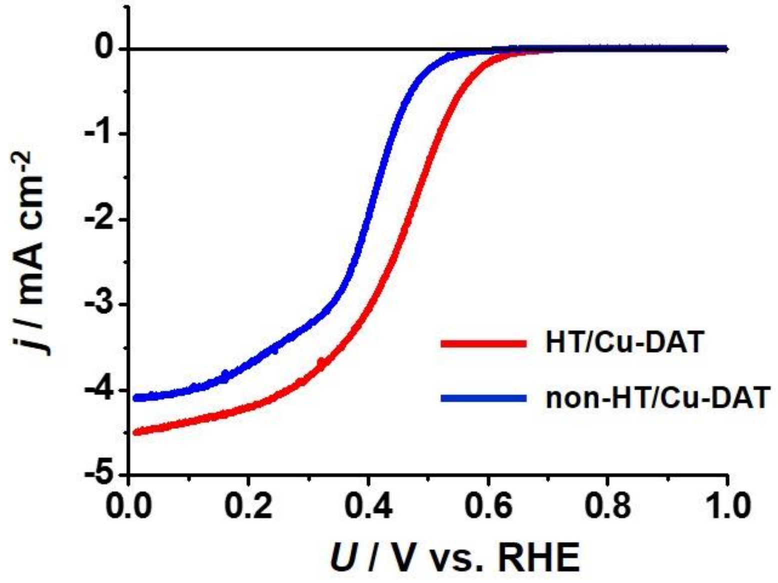

Fig. 6. *j* vs. *U* curves for HT/Cu-DAT (red) and non-HT/Cu-DAT (blue) in 0.5 M $NaClO_4$ solution (pH = 7.1). Rotation rate: 1500 rpm; scan rate: 10 mV/s.

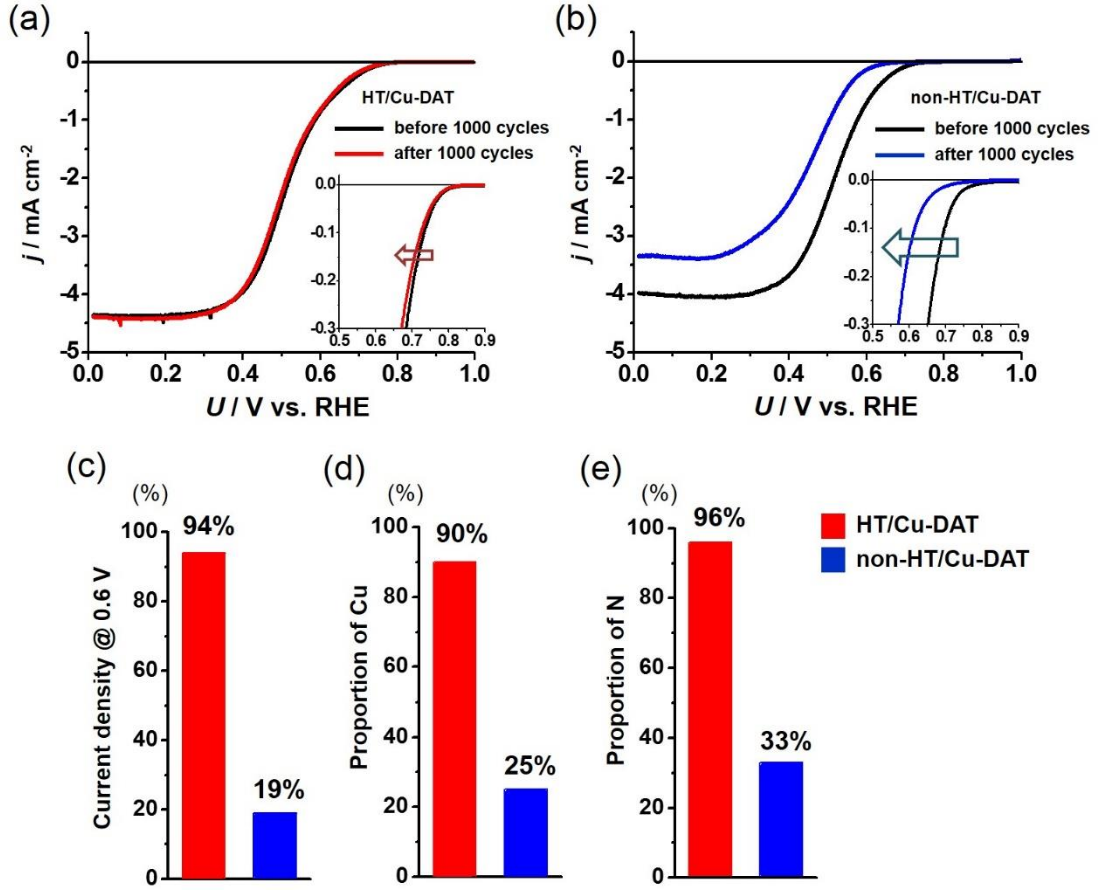

Fig. 7. j vs. U curves for (a) HT/Cu-DAT and (b) non-HT/Cu-DAT before (black) and after ((a) red, (b) blue) 1000 CV cycles in 0.1 M phosphate buffer solution (pH 7.0). Rotation rate: 1500 rpm; scan rate: 10 mV/s. The insets show magnified curves, and the arrows indicate the shift during 1000 CV cycles. Relative values of (c) current density at 0.6 V and the concentrations of (d) Cu and (e) N atoms after 1000 cycles of CV compared to the absolute values of each factor before the CV.

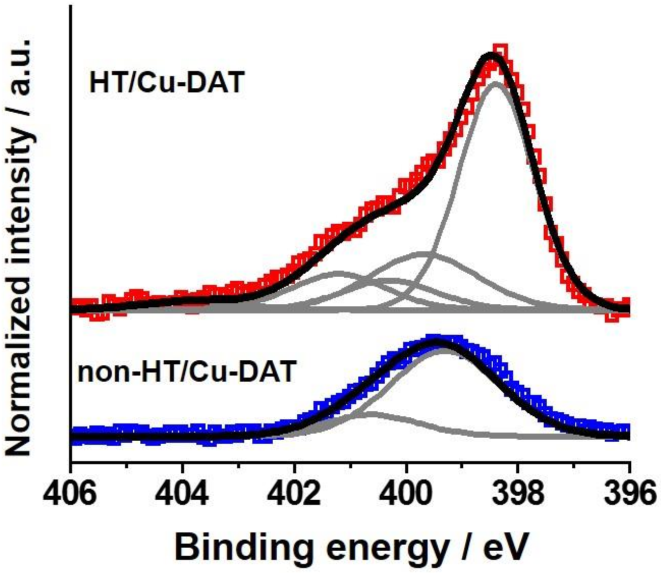

Fig. 8. N-1s XPS spectra for HT/Cu-DAT (upper) and non-HT/Cu-DAT (lower). Measured data (open colored squares), fitted curve (black line) and deconvoluted curves (gray lines).

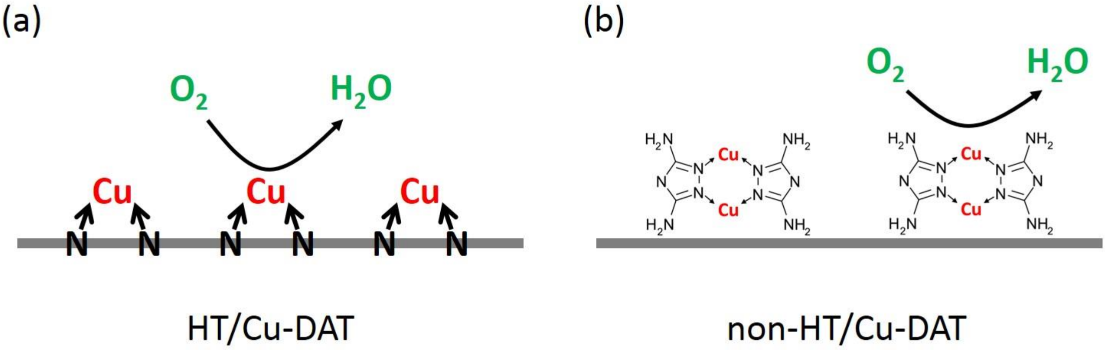

Fig. 9. Schematic illustrations of the active sites for ORR in (a) HT/Cu-DAT and (b) non-HT/Cu-DAT.

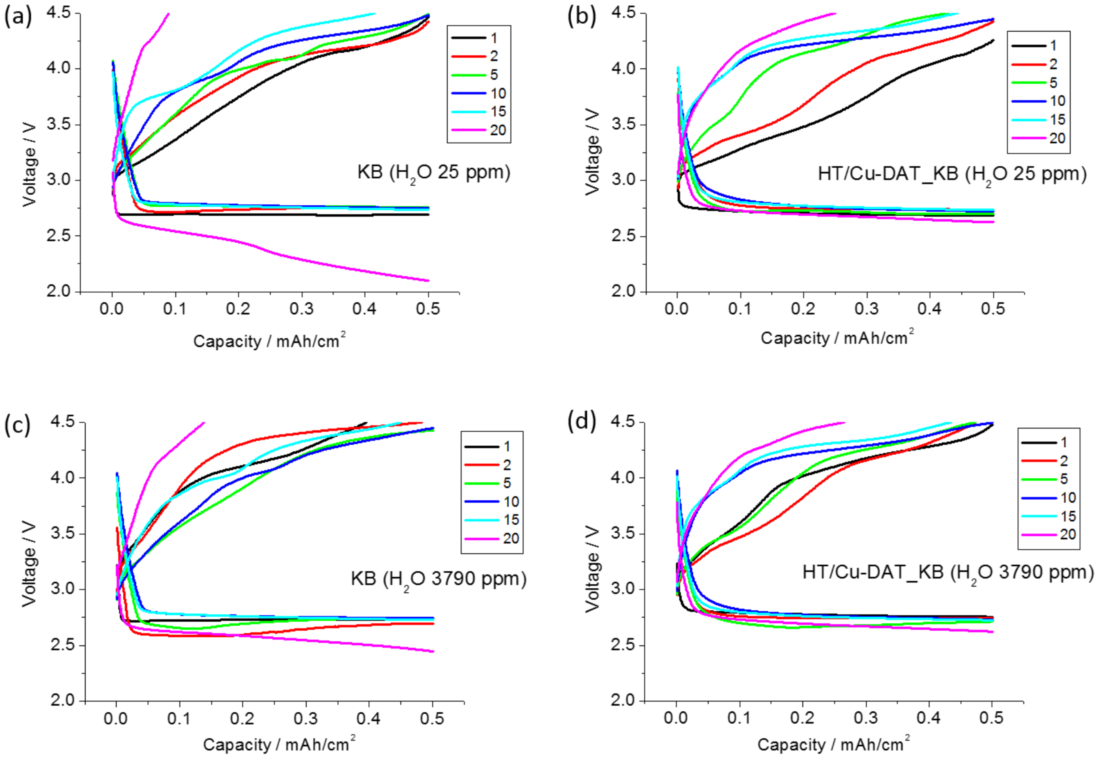

Fig. 10. Discharge-charge profiles for Li-air batteries with (a, c) KB and (b, d) HT/Cu-DAT_KB as a cathode material in the presence of (a, b) 25 ppm and (c, d) 3790 ppm of water in the electrolyte. The cycle tests were conducted at 0.1 mA/cm^2 with 0.5 mAh/cm^2 capacity limitation. 2.0 V and 4.5 V were set as a cut-off voltage for the discharge and the charge, respectively.

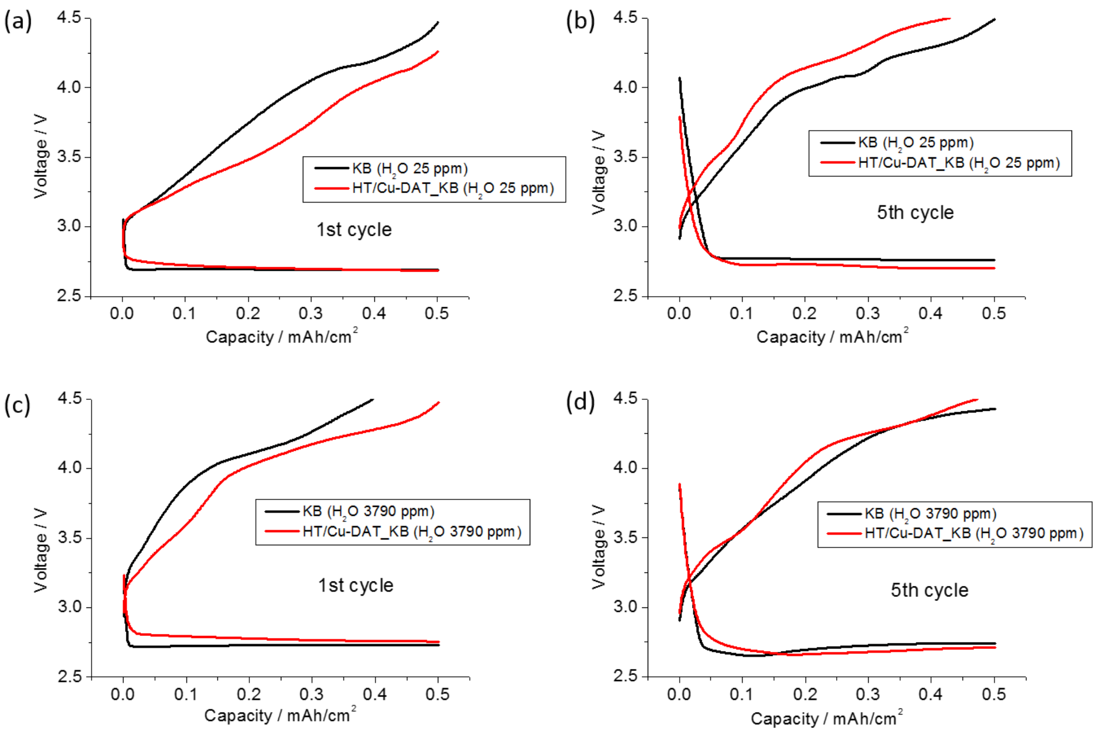

Fig. 11. Comparison of discharge-charge curves for Li-air batteries in the presence and absence of HT/Cu-DAT_KB catalyst. The curves were obtained at (a, c) the 1st cycle and (b, d) the 5th cycle in the electrolyte containing (a, b) 25 ppm and (c, d) 3790 ppm of water. The cycle tests were conducted at 0.1 mA/cm^2 with 0.5 mAh/cm^2 capacity limitation. 2.0 V and 4.5 V were set as a cut-off voltage for the discharge and the charge, respectively.

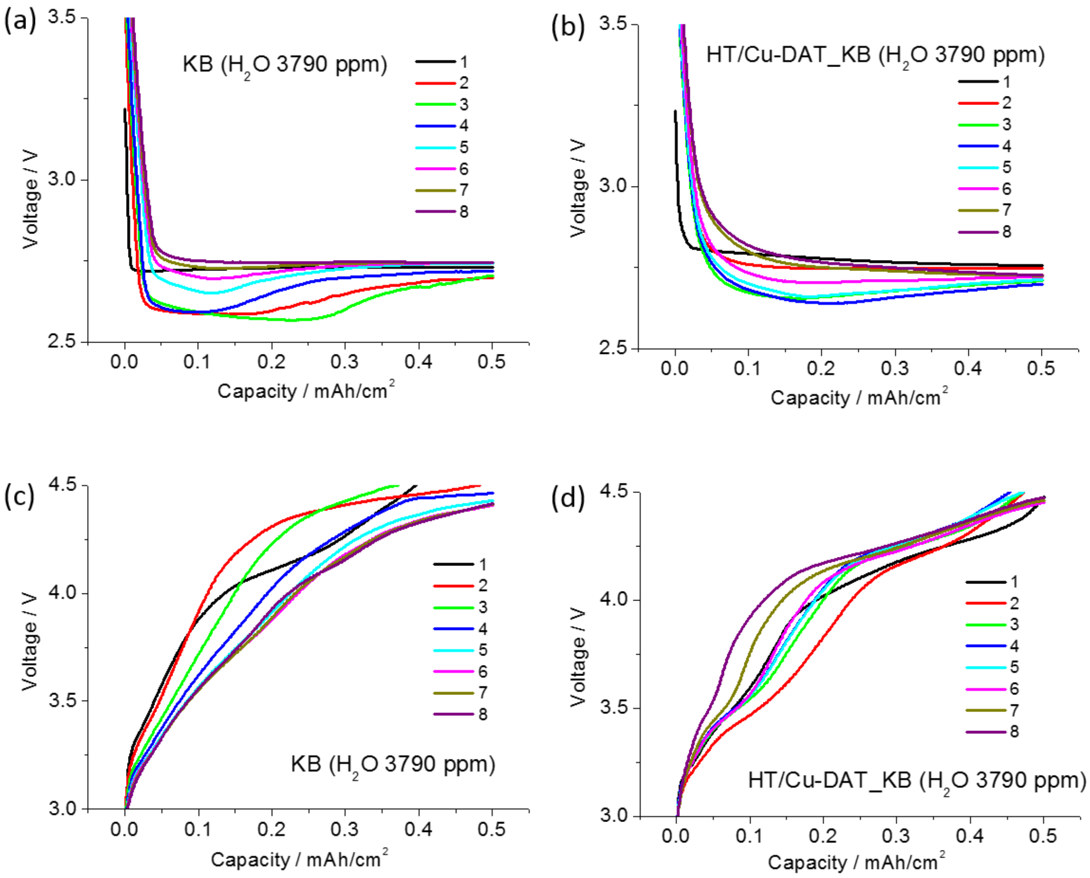

Fig. 12. (a, b) Discharge and (c, d) charge curves obtained from 1st to 8th cycle for Li-air batteries with (a, c) KB and (b, d) HT/Cu-DAT_KB as a cathode material in the presence of 3790 ppm of water in the electrolyte. The cycle tests were conducted at 0.1 mA/cm^2 with 0.5 mAh/cm^2 capacity limitation. 2.0 V and 4.5 V were set as a cut-off voltage for the discharge and the charge, respectively.

	Cu/C	N/C
HT/Cu-DAT	0.012	0.085
non-HT/Cu-DAT	0.0032	0.033

Table 1. Cu/C and N/C ratios for HT/Cu-DAT and non-HT/Cu-DAT before performing 1000 CV cycles calculated from XPS spectra.

(a)

	pyridine N	N in triazole ring / pyrrole N	amine N	graphite N	N oxide
HT/Cu-DAT	56	20	9	12	3

(b)

	N in triazole ring	amine N
non-HT/Cu-DAT	81	19

Table 2. Relative ratios of various nitrogen components in (a) HT/Cu-DAT and (b) non-HT/Cu-DAT calculated from decomposed N-1s XPS spectra.

2.2.4. Conclusion

A novel Cu-based ORR electrocatalyst (HT/Cu-DAT) was successfully synthesized by the short-duration heat treatment of 3,5-diamino-1,2,4-triazole in the presence of r-GOs. The resultant hybrid material exhibited high stability and the best ORR activity in neutral solutions among the Cu-based electrocatalysts reported to date. XPS and EXAFS analyses revealed that Cu atoms coordinated by N atoms were introduced into the *sp*2-networks of graphene via the heat treatment, leading to the improved stability of HT/Cu-DAT. We speculate that (1) the heat treatment was stopped before the complete breakage of active sites, thereby preserving the ORR activity of non-HT/Cu-DAT, and (2) the ORR catalytic activity can be further improved by the selection of an appropriate precursor. Further studies are required for clarifying the molecular structure of the active sites of HT/Cu-DAT.

In addition, the synthesized catalyst was employed as a cathode material in aprotic Li-air batteries. The decrease in the discharge voltage and the charge overvoltage was observed in the coexistence of the catalyst and water in the first few cycle. However, these characteristics did not significantly improve the cycle life. More sophisticated design of the electrocatalyst (e.g. accelerating the cleavage and formation of O=O bonds of molecular oxygen by introducing the active sites composed of multinuclear metal centers) is highly required to effectively use the contaminant water for the operation of Li-air batteries.

References

[1] J. Lu, L. Li, J. Park, Y. Sun, F. Wu, K. Amine, *Chem. Rev.*, **2014**, *114*, 5611.

[2] M. H. Cho, J. Trottier, C. Gagnon, P. Hovington, D. Clement, A. Vijh, C. S. Kim, A. Guerfi, R. Black, L. Nazar, K. Zaghib, *J. Power Sources*, **2014**, *268*, 565.

[3] Z. Guo, X. Dong, Y. Wang, Y. Xia, *Chem. Commun.*, **2015**, *51*, 676.

[4] Z. Guo, X. Dong, S. Yuan, Y. Wang, Y. Xia, *J Power Sources*, **2014**, *264*, 1.

[5] G. Wang, L. Huang, S. Liu, J. Xie, S. Zhang, P. Zhu, G. Cao, X. Zhao, *ACS Appl. Mater. Interfaces*, **2015**, *7*, 23876.

[6] K. U. Schwenke, M. Metzger, T. Restle, M. Piana, H. A. Gasteiger, *J. Electrochem. Soc.*, **2015**, *162*, A573.

[7] N. B. Aetukuri, B. D. McCloskey, J. M. García, L. E. Krupp, V. Viswanathan, A. C. Luntz, *Nat. Chem.*, **2015**, *7*, 50.

[8] Y. Qiao, S. Wu, J. Yi, Y. Sun, S. Guo, S. Yang, P. He, H. Zhou, *Angew. Chem. Int. Ed.*, **2017**, *56*, 4960.

[9] T. Liu, M. Leskes, W. Yu, A. J. Moore, L. Zhou, P. M. Bayley, G. Kim, C. P. Grey, *Science*, **2015**, *350*, 530.

[10] F. Li, S. Wu, D. Li, T. Zhang, P. He, A. Yamada, H. Zhou, *Nat. Commun.*, **2015**, *6*, 8843.

[11] S. Wu, J. Tang, F. Li, X. Liu, H. Zhou, *Chem. Commun.*, **2015**, *51*, 16860.

[12] N. Togasaki, T. Momma, T. Osaka, *J. Power Sources*, **2014**, *261*, 23.

[13] N. Togasaki, T. Momma, T. Osaka, *J. Power Sources*, **2015**, *294*, 588.

[14] B. D. McCloskey, D. S. Bethune, R. M. Shelby, G. Girishkumar, A. C. Luntz, *J. Phys. Chem. Lett.*, **2011**, *2*, 1161.

[15] Z. Peng, S. A. Freunberger, Y. Chen, P. G. Bruce, *Science*, **2012**, *337*, 563.

[16] Y. Okamoto, Y. Kubo, *J. Phys. Chem. C*, **2013**, *117*, 15940.

[17] H. Moon, T. Mandai, R. Tatara, K. Ueno, A. Yamazaki, K. Yoshida, S. Seki, K. Dokko, M. Watanabe, *J. Phys. Chem. C*, **2015**, *119*, 3957.

[18] R. Black, S. H. Oh, J. Lee, T. Yim, B. Adams, L. F. Nazar, *J. Am. Chem. Soc*., **2012**, *134*, 2902.

[19] J. L. Goldman, R. M. Mank, J. H. Young, V. R. Koch, *J. Electrochem. Soc*., **1980**, *127*, 1461.

[20] H. Wang, S. Sunahiro, M. Matsui, P. Zhang, Y. Takeda, O. Yamamoto, N. Imanishi, *ChemElectroChem*, **2015**, *2*, 1144.

[21] J. Qian, W. A. Henderson, W. Xu, P. Bhattacharya, M. Engelhard, O. Borodin, J. Zhang, *Nat. Commun*., **2015**, *6*, 6362.

[22] I. A. Shkrob, T. W. Marin, Y. Zhu, D. P. Abraham, *J. Phys. Chem. C*, **2014**, *118*, 19661.

[23] H. Han, S. Zhou, D. Zhang, S. Feng, L. Li, K. Liu, W. Feng, J. Nie, H. Li, X. Huang, M. Armand, Z. Zhou, *J. Power Sources*, **2011**, *196*, 3623.

[24] T. Osaka, T. Momma, T. Tajima, Y. Matsumoto, *J. Electrochem. Soc*., **1995**, *142*, 1057.

[25] T. Osaka, T. Momma, Y. Matsumoto, Y. Uchida, *J. Electrochem. Soc*., **1997**, *144*, 1709.

[26] T. Momma, H. Nara, S. Yamagami, C. Tatsumi, T. Osaka, *J. Power Sources*, **2011**, *196*, 6483.

[27] J. Qian, W. Xu, P. Bhattacharya, M. Engelhard, W. A. Henderson, Y. Zhang, J. Zhang, *Nano Energy*, **2015**, *15*, 135.

[28] J. K. S. Goodman, P. A. Kohl, *J. Electrochem. Soc*., **2014**, *161*, D418.

[29] B. Scharifker, G. Hills, *Electrochim. Acta*, **1983**, *28*, 879.

[30] J. K. Stark, Y. Ding, P. A. Kohl, *J. Electrochem. Soc*., **2013**, *160*, D337.

[31] A. Pei, G. Zheng, F. Shi, Y. Li, Y. Cui, *Nano Lett*., **2017**, *17*, 1132.

[32] S. Shiraishi, K. Kanamura, Z. Takehara, *Langmuir*, **1997**, *13*, 3542.

[33] S. Shiraishi, K. Kanamura, Z. Takehara, *J. Electrochem. Soc*., **1999**, *146*, 1633.

[34] N. Togasaki, T. Momma, T. Osaka, *J. Power Sources*, **2016**, *307*, 98.

[35] J. Shui, J. S. Okasinski, P. Kenesei, H. A. Dobbs, D. Zhao, J. D. Almer, D. Liu, *Nat. Commun*., **2013**, *4*, 2255.

[36] S. H. Lee, R. A. DeMayo, K. J. Takeuchi, E. S. Takeuchi, A. C. Marschilok, *J. Electrochem. Soc*., **2015**, *162*, A69.

[37] S. Tsujimura, Y. Kamitaka, K. Kano, *Fuel Cells*, **2007**, *7*, 463.

[38] N. Mano, V. Soukharev, A. Heller, *J. Phys. Chem. B*, **2006**, *110*, 11180.

[39] N. Mano, J.L. Fernandez, Y. Kim, W. Shin, A.J. Bard, A. Heller, *J. Am. Chem. Soc*., **2003**, *125*, 15290.

[40] E.I. Solomon, D.E. Heppner, E.M. Johnston, J.W. Ginsbach, J. Cirera, M. Qayyum, M.T. Kieber-Emmons, C.H. Kjaergaard, R.G. Hadt, L. Tian, *Chem. Rev*., **2014**, *114*, 3659.

[41] E.I. Solomon, J.W. Ginsbach, D.E. Heppner, M.T. Kieber-Emmons, C.H. Kjaergaard, P.J. Smeets, L. Tian, J.S. Woertink, *Faraday Discuss*., **2011**, *148*, 11.

[42] M.A. Thorseth, C.E. Tornow, E.C.M. Tse, A.A. Gewirth, *Chem. Rev*., **2013**, *257*, 130.

[43] M.S. Thorum, J. Yadav, A.A. Gewirth, *Angew. Chem. Int. Ed*., **2009**, *48*, 165.

[44] I.O. Matos, T.L. Ferreira, T.R.L.C. Paixao, A.S. Lima, M. Bertotti, W.A. Alves, *Electrochim. Acta*, **2010**, *55*, 5223.

[45] S. Kim, J.W. Ginsbach, A.I. Billah, M.A. Siegler, C.D. Moore, E.I. Solomon, K.D. Karlin, *J. Am. Chem. Soc*., **2014**, *136*, 8063.

[46] S. Fukuzumi, K.D. Karlin, *Coord. Chem. Rev*., **2013**, *257*, 187.

[47] C.C.L. McCrory, A. Devadoss, X. Ottenwaelder, R.D. Lowe, T.D.P. Stack, C.E.D. Chidsey, *J. Am. Chem. Soc*., **2011**, *133*, 3696.

[48] M. Asahi, S. Yamazaki, S. Itoh, T. Ioroi, *Dalton Trans*., **2014**, *43*, 10705.

[49] M. Kato, K. Kimijima, M. Shibata, H. Notsu, K. Ogino, K. Inokuma, N. Ohta, H. Uehara, Y. Uemura, N. Oyaizu, T. Ohba, S. Takakusagi, K. Asakura, I. Yagi, *Phys. Chem. Chem. Phys*., **2015**,

17, 8638.

[50] K. Kamiya, H. Koshikawa, H. Kiuchi, Y. Harada, M. Oshima, K. Hashimoto, S. Nakanishi, *ChemElectroChem*, **2014**, *1*, 877.

[51] K. Kamiya, K. Hashimoto, S. Nakanishi, *Chem. Commun.*, **2012**, *48*, 10213.

[52] K. Kamiya, K. Hashimoto, S. Nakanishi, *ChemElectroChem*, **2014**, *1*, 858.

[53] L.W. Liao, M.F. Li, J. Kang, D. Chen, Y. Chen, S. Ye, *J. Electroanal. Chem.*, **2013**, *688*, 207.

[54] H.R. Byon, J. Suntivich, E.J. Crumlin, Y. Shao-Horn, *Phys. Chem. Chem. Phys.*, **2011**, *13*, 21437.

[55] H.R. Byon, J. Suntivich, Y. Shao-Horn, *Chem. Mater.*, **2011**, *23*, 3421.

[56] H. Liang, W. Wei, Z. Wu, X. Feng, K. Mullen, *J. Am. Chem. Soc.*, **2013**, *135*, 16002.

[57] Q. He, X. Yang, R. He, A. Bueno-López, H. Miller, X. Ren, W. Yang, B.E. Koel, *J. Power Sources*, **2012**, *213*, 169.

[58] X. Qing, J. Shi, C. Ma, M. Fan, Z. Bai, Z. Chen, J. Qiao, J. Zhang, *J. Power Sources*, **2014**, *266*, 88.

[59] G. Wu, C.M. Johnston, N.H. Mack, K. Artyushkova, M. Ferrandon, M. Nelson, J.S. Lezama-Pacheco, S.D. Conradson, K.L. More, D.J. Myers, P. Zelenay, *J. Mater. Chem.*, **2011**, *21*, 11392.

[60] W. Li, A. Yu, D.C. Higgins, B.G. Llanos, Z. Chen, *J. Am. Chem. Soc.*, **2010**, *132*, 17056.

[61] N. Vasimalai, S.A. John, *J. Mater. Chem. A*, **2013**, *1*, 4475.

[62] P. Kannan, S.A. John, *Nanotechnology*, **2008**, *19*, 085602.

[63] M. Tourabi, K. Nohair, M. Traisnel, C. Jama, F. Bentiss, *Corros. Sci.*, **2013**, *75*, 123.

[64] B. Wrzosek, J. Bukowska, *J. Phys. Chem. C*, **2007**, *111*, 17397.

[65] M. Lefevre, E. Proietti, F. Jaouen, J. Dodelet, *Science*, **2009**, *324*, 71.

[66] Z. Shi, H. Liu, K. Lee, E. Dy, J. Chlistunoff, M. Blair, P. Zelenay, J. Zhang, Z. Liu, *J. Phys. Chem. C*, **2011**, *115*, 16672.

Chapter 3

Analysis of dynamic changes of charge transfer resistance at Li/solid electrolyte interfaces during Li deposition-dissolution reactions

3.1. Introduction

The studies explained in 1.4.3 have provided potential strategies to reduce the charge-transfer resistance of the Li/LLZ interface (R_{int}) toward the successful operation of all-solid-state batteries; however, there is still limited information of regarding how R_{int} dynamically changes during repetitive Li deposition/dissolution cycles. Alternating current (AC) impedance spectroscopy is a nondestructive method used to examine the time transient of the resistance in an electrolyte and at an electrode/electrolyte interface. The AC impedance technique has been recently applied to study Li/LLZ interfaces *in situ* during repetitive Li deposition/dissolution cycles [1-4]. In these reports, the increase in R_{int} measured using symmetrical Li/LLZ/Li cells was interpreted to be derived from the deterioration of the physical contact between Li and LLZ due to void formation during Li dissolution on one electrode. However, for the two-electrode system, the information from two Li/LLZ interfaces were indivisibly included in the impedance spectra. Therefore, the rise in R_{int} thus measured cannot, in principle, be assigned to either Li deposition or dissolution, despite the significant importance of knowing which reaction should be controlled more precisely to realize high-rate and long-life batteries. To address this issue, AC impedance spectroscopy with a three-electrode setup, in which the interface between a working electrode and electrolyte can be examined independently from the other interface between a counter electrode and the electrolyte, is necessary. In the present work, we attempted to individually trace the dynamic change in R_{int} at a Li/LLZ interface during Li deposition and dissolution reactions through the use of the three-electrode AC impedance technique.

3.2. Experimental

3.2.1. Preparation of LLZ powder and pellets

LLZ powder was prepared by the conventional solid-state method [5, 6]. Lithium hydroxide monohydrate (Kanto Chemical Co., Inc., 98.0%), Lanthanum hydroxide (Kojundo Chemical Laboratory Co., Ltd., 99.99%), Zirconium oxide (Tosoh Co.) were mixed in a molar ratio of 7.7:3:2 with 10% excess Li source to compensate for the loss of Li during calcination. The mixture was ball-milled in hexane at 400 rpm intermittently for 2 h with zirconia balls (5 mm diameter) in a planetary ball-mill (Pulverisette 6, Fritsch). The mixed powder was calcined in an alumina crucible at 900 °C for 15 h in air, and then the calcined powder was mixed with γ-aluminum oxide (Kojundo Chemical Laboratory Co., Ltd., 99.99%) according to the nominal formula of $Al_{0.25}Li_{6.25}La_3Zr_2O_{12}$ by planetary ball-milling in the same way. The obtained powder was sieved to below 710 μm and pressed into a pellet of 15 mm diameter under a pressure of 20 MPa for 5 min. The pellets were covered by protective mother powder with the same composition in an alumina crucible, and sintered at 900 °C for 3 h and then at 1200 °C for 24 h in air. X-ray diffraction (XRD) measurement of the powder sample obtained by fracturing the pellet after sintering confirmed that LLZ with a cubic structure was successfully prepared (Fig. 1(a)). After sintering, the pellets were polished to a thickness of 800 μm in air, and dried at 110 °C overnight under vacuum to remove the residual water. The surface was then finally polished with emery paper (#4000) in an argon-filled glove box with a water content of less than 1 ppm to ensure the removal of the resistive Li_2CO_3 layer formed on the surface [7]. Although some micropores due to Li evaporation during sintering were observed using field-emission scanning electron microscopy (SEM), the grains with the size of several hundreds of μm were well grown with intimate connections between them (Fig. 1(b)). The relative density of the LLZ pellet was calculated to be 94% by dividing the bulk density by the theoretical density (5.1 g/cm^3), which was in the range of the reported values (90–99%). These results indicated that a well-sintered and dense LLZ pellet was obtained. The Li-ion conductivity of the LLZ pellet was measured following a well-established protocol [5], and then calculated to be 1.2×10^{-4} S/cm (Fig. 1(c)), which is in the range of previously reported values [1, 5, 8-11].

3.2.2. Characterization of LLZ

XRD (D8 ADVANCE, Bruker) patterns were recorded with a step size of 0.015° and a collection time of 1 s at 40 kV and 40 mA over the 2θ angular range between 10° and 70°. SEM (JSM-7800F, JEOL) was used to observe the cross-section of a LLZ pellet. The sample was transferred from the glove box to the SEM instrument in a sealed vessel filled with argon gas. Measurements were conducted at an acceleration voltage of 5 kV under an ambient pressure of less than 10^{-4} Pa.

3.2.3. Cell assembly and electrochemical measurements

A three-electrode cell was assembled using metallic-Li foil (3 mm diameter, 400 μm thick, Honjo Metal Co., Ltd.) as both working electrode (W.E.) and counter electrode (C.E.), and a metallic-Li ring (outer diameter = 10 mm, inner diameter = 8 mm, Honjo Metal Co., Ltd.) was used as a reference electrode (R.E.), as shown in Fig. 2. The surface of the metallic-Li electrodes was polished with emery paper (#4000) to remove the passivation layer formed on the surface. Assembled cells were heated at 100 °C for 4 h in air before electrochemical measurements.

Galvanostatic Li dissolution/deposition and AC impedance measurements were conducted at 25 °C using a potentio-galvanostat equipped with an impedance analyzer (VMP3, BioLogic Science Instruments). AC impedance spectra were collected with an amplitude of 15 mV in the frequency range from 1 MHz to 100 Hz. For measurement of the Li-ion conductivity, a symmetrical Au/LLZ/Au cell, in which Au was sputtered on both surfaces of the LLZ pellet as ion blocking electrodes, was also utilized.

3.3. Results and discussion

The dynamic changes in the charge transfer resistance at the Li/LLZ interface during Li dissolution/deposition cycles were investigated using the three-electrode AC impedance technique to individually clarify the influence of Li dissolution and deposition on the resistance. In this experiment, Li was repeatedly dissolved and deposited for 1 h at 50 μA/cm^2, and AC impedance measurement was conducted every 10 min during the cycle test. Fig. 3 shows representative Nyquist plots obtained during the test. An equivalent circuit used for fitting the plots was composed of two series of the parallel combination of resistance and constant phase element (CPE) as shown in the inset of Fig. 3. The subscript LLZ and int means the contribution from LLZ solid electrolyte and Li (W.E.)/LLZ interface, respectively. Fig. 4(a) and (b) show the time courses of the W.E. potential and R_{int}, respectively. The overpotential increased during Li dissolution, whereas it continued to decrease during Li deposition (Fig. 4(a)). R_{int} increased and decreased during Li dissolution and deposition, respectively (Fig. 4(b) and Table 1), which is in good agreement with the trends for the overpotential. However, R_{int} did not return to the initial value after one cycle of dissolution/deposition, indicating that the change in R_{int} during dissolution is larger than that during deposition. The degree of R_{int} change during Li dissolution and deposition grew larger with cycle number and the cell short-circuited in less than 10 cycles. It should be noted that R_{int} decreased only slightly (Fig. 5(a)) when the cell was kept at the open-circuit potential after Li dissolution. In addition, unlike the case of Fig. 4(b), R_{int} exhibited almost no decrease when the Li deposition was performed without previous dissolution (Fig. 5(b)). These results demonstrated that the decrease in R_{int} shown in Fig. 4(b) is characteristic of Li deposition followed by Li dissolution.

The changes in R_{int} during Li dissolution and deposition in the case of a four-fold increase in the amount of dissolved or deposited Li (corresponding to 1 μm thickness of Li) were also investigated. The overpotential and R_{int} increased monotonically during Li dissolution. However, during subsequent Li deposition, the resistance rapidly decreased below the initial value, which implied that Li dendrites were grown to a significant extent. The cell was actually short-circuited within a short time (Fig. 6).

Next, the effect of the current density on the change in R_{int} was investigated next (Fig. 7). In these experiments, the amount of dissolved or deposited Li metal was fixed to be the same by controlling the duration of dissolution/deposition, and R_{int} was measured every time before switching polarization. R_{int} increased and decreased during Li dissolution and deposition, respectively, which was qualitatively similar to the results shown in Fig. 4. However, the extent of the change in the resistance during both dissolution and deposition was larger for higher current density.

As described above, R_{int} was demonstrated to increase and decrease during Li dissolution and deposition, respectively, using the three-electrode AC impedance technique. Previous AC impedance studies using a two-electrode system interpreted that R_{int} increases during cycling due to the formation of voids at the metal/solid-electrolyte interfaces during metal dissolution [1-4, 12–14]. Actually, the formation of voids was confirmed when the tightly adhered metal/solid-electrolyte interface was constructed by vacuum evaporation of Li onto LLZ surface [3]. In addition, the change in R_{int} caused by chemical reaction between Li and LLZ should be negligible because LLZ is chemically stable against Li metal [8, 15–22]. Therefore, it is reasonable to interpret that the increase in the R_{int} shown in Figs. 4 and 5 and 7 also originates from the voids formed during Li dissolution, although the voids newly generated during the dissolution cannot be distinguished from those existing in the as-prepared interface by SEM due to the intrinsic roughness of the Li foil and LLZ. The voids thus formed during the dissolution could then be partially filled during subsequent Li deposition, resulting in a reduction of R_{int} as schematically shown in Fig. 8.

Time courses of the overpotential and R_{int} shown in Fig. 4 can be well explained by this model. First, let us consider the time courses during Li dissolution. As Li dissolution progresses, the size and/or the density of the voids formed at the Li/LLZ interface is inevitably increased. Therefore, the physical contact area at the Li and LLZ interfaces decreases, which in turn increases the effective current density and thus the overpotential during galvanostatic Li dissolution. Besides, R_{int} also increased because R_{int} is inversely proportional to the contact area between Li and LLZ. The physical contact area can be further reduced at larger overpotential because a higher density of metal nuclei are generally formed during Li deposition [23–27], so that a larger number of voids are formed during subsequent Li dissolution. R_{int} was noted to increase more largely at higher current density, despite the same flowing charge, as shown in Fig. 7.

On the other hand, when the polarization was switched, the voids formed during the Li dissolution can only be partially filled via the subsequent Li deposition process. The contact area of the Li/LLZ interface is smaller in the beginning; therefore, a larger overpotential is required for Li deposition to proceed. However, with the progress of Li deposition, the contact area is gradually increased and thereby R_{int} can be smaller. Therefore, the overpotential is decreased in association with the decrease in R_{int}. This model was verified by the experimental results shown in Fig. 5(a) and (b), in which it was shown that the increased resistance after Li dissolution did not decrease unless Li deposition was performed subsequently, and that the resistance and the overpotential were constant when Li deposition was conducted without prior Li dissolution.

Fig. 4 shows that R_{int} did not return to the initial value after one cycle of dissolution/deposition, which suggests that voids were gradually accumulated at the interface as the cycle proceeded. This is a problem from the viewpoint of obtaining stable cycle characteristics because the voids inevitably induce non-uniformity of the flux of Li^+ ions at the interface, which leads to the growth of Li dendrites. Indeed, when the amount of dissolution was increased, the short-circuit immediately occurred during the subsequent Li deposition process, as shown in Fig. 6. Based on the findings obtained in this research, a strategy to prevent the formation of voids at the interface during Li dissolution is particularly important.

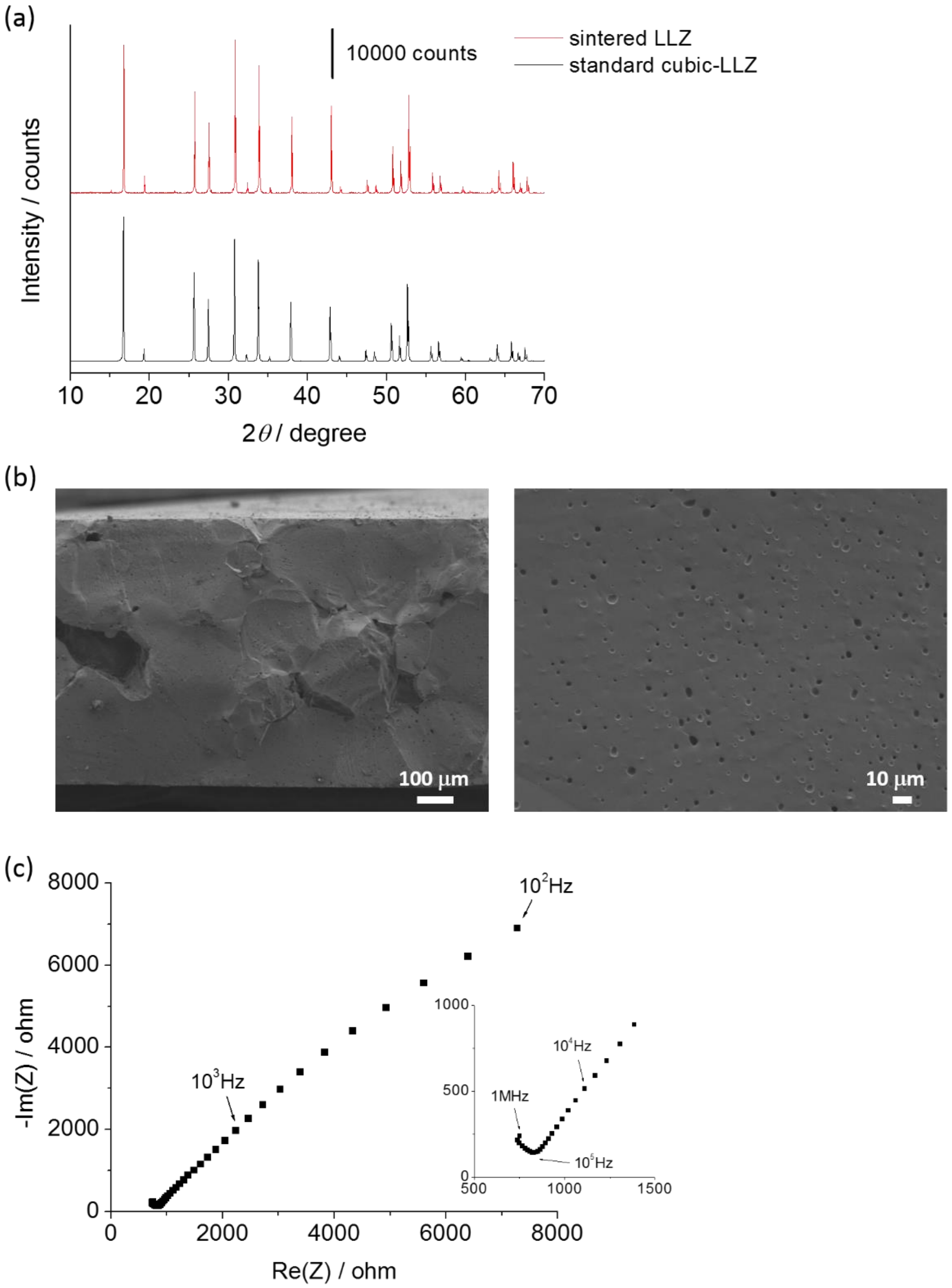

Fig. 1. (a) XRD patterns for sintered LLZ and standard cubic-LLZ. (b) Cross-sectional SEM images of a LLZ pellet taken at different magnification. (c) Nyquist plot of a symmetrical Au/LLZ/Au cell. The inset shows the magnified plot.

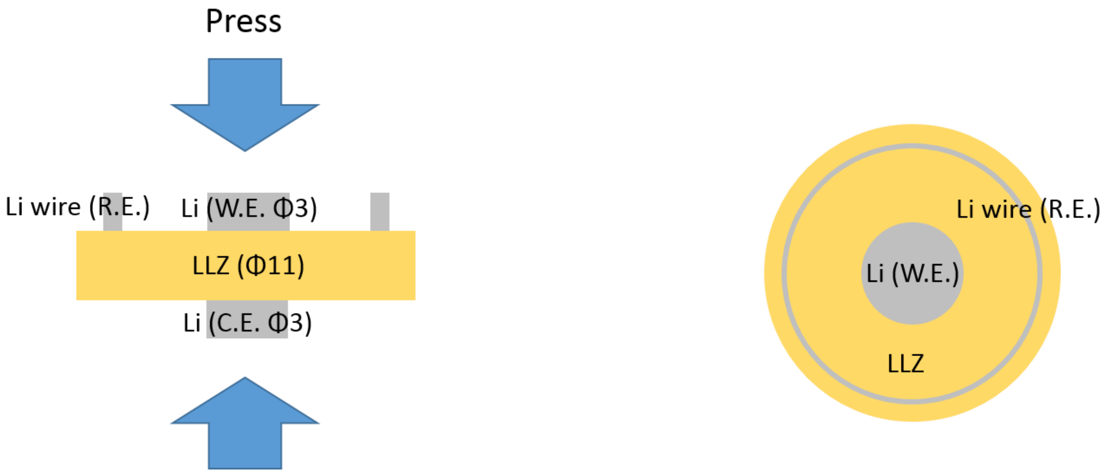

Fig. 2. Schematic illustration of a three-electrode cell used in this work; the cross-sectional view and the top view.

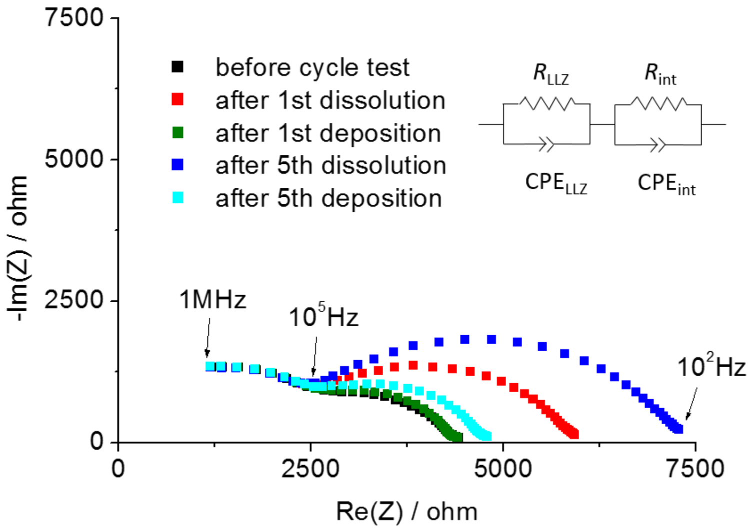

Fig. 3. Nyquist plots for a Li (W.E.)/Li (R.E.)/LLZ/Li (C.E.) three-electrode cell obtained before and during a galvanostatic cycle test at 50 μA/cm^2. The inset shows the equivalent circuit used for the estimation of R_{int}.

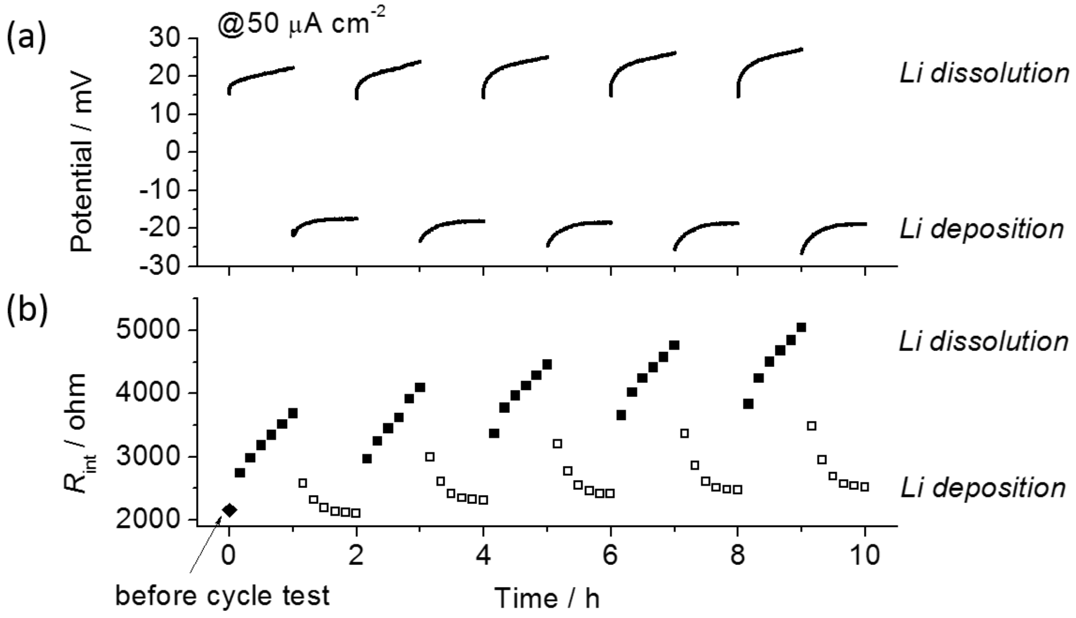

Fig. 4. (a) W.E. potential and (b) charge transfer resistance at the Li (W.E.)/LLZ interface as a function of time when Li metal corresponding to the thickness of 250 nm was dissolved and deposited at 50 μA/cm^2 in a three-electrode cell. The resistance measured during Li deposition and dissolution are plotted as open and closed squares, respectively.

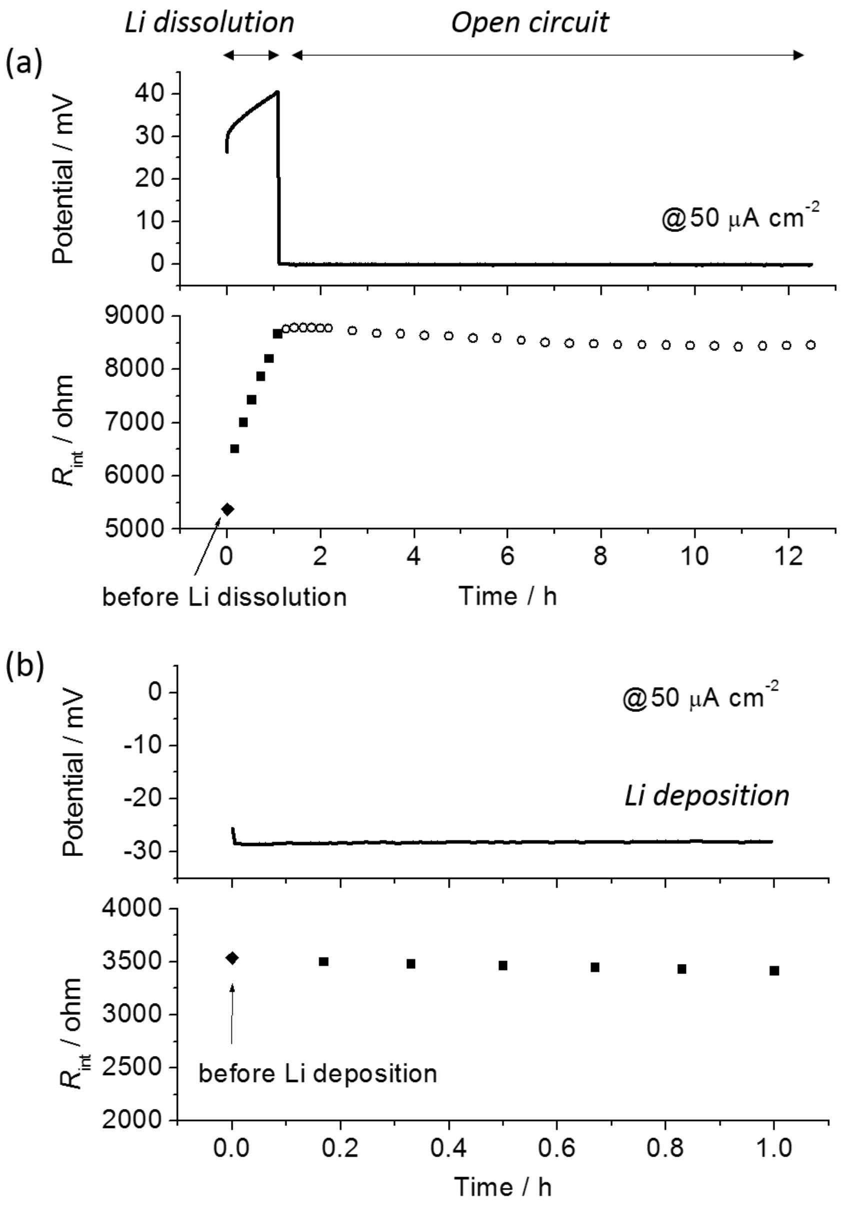

Fig. 5. W.E. potential and charge transfer resistance at the Li (W.E.)/LLZ interface as a function of time (a) when Li was dissolved at 50 μA/cm^2 for 1 h and the cell was then kept at the open-circuit potential, and (b) when Li was deposited at 50 μA/cm^2 for 1 h without Li dissolution beforehand. The resistance measured during Li dissolution/deposition and at the open-circuit potential are plotted as closed squares and open circles, respectively.

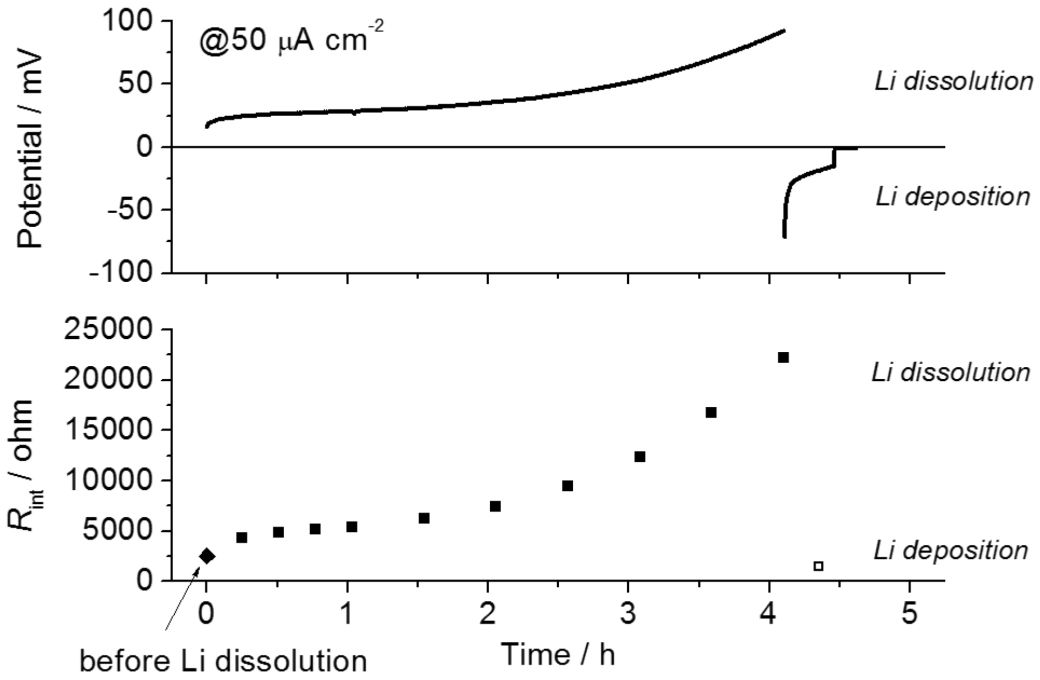

Fig. 6. W.E. potential and charge transfer resistance at the Li (W.E.)/LLZ interface as a function of time when Li metal corresponding to the thickness of 1 μm was dissolved and deposited at 50 μA/cm^2 in a three-electrode cell. The resistance measured during Li deposition and dissolution are plotted as open and closed squares, respectively.

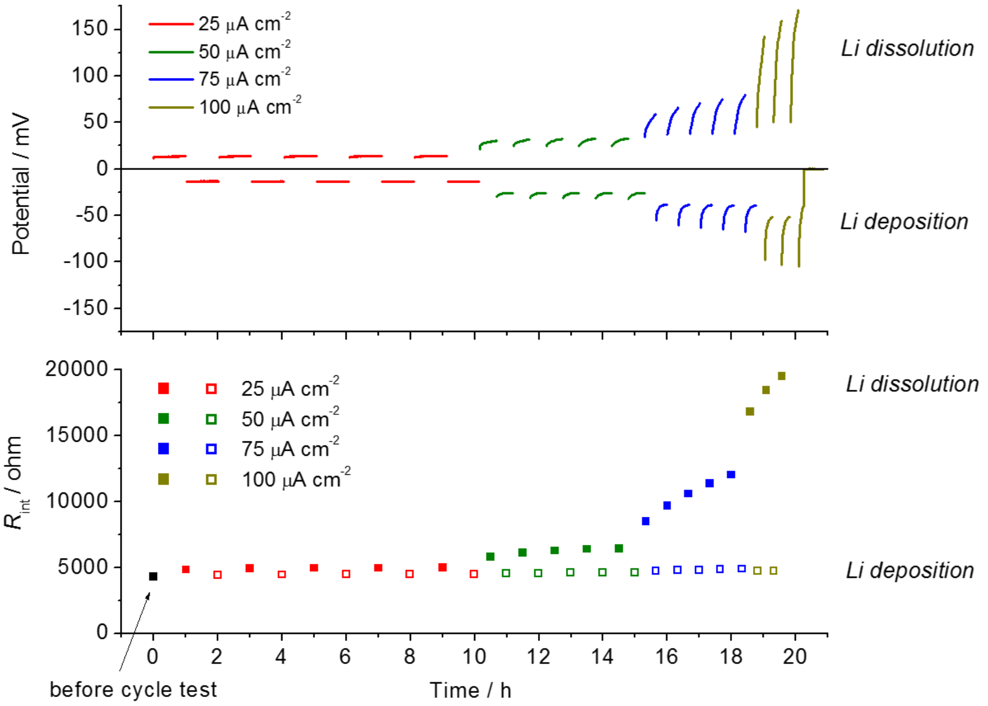

Fig. 7. W.E. potential and charge transfer resistance at the Li (W.E.)/LLZ interface as a function of time when Li metal corresponding to a thickness of 125 nm was dissolved and deposited at 25, 50, 75, 100 µA/cm^2. The resistance measured after Li deposition and dissolution are plotted as open and closed squares, respectively.

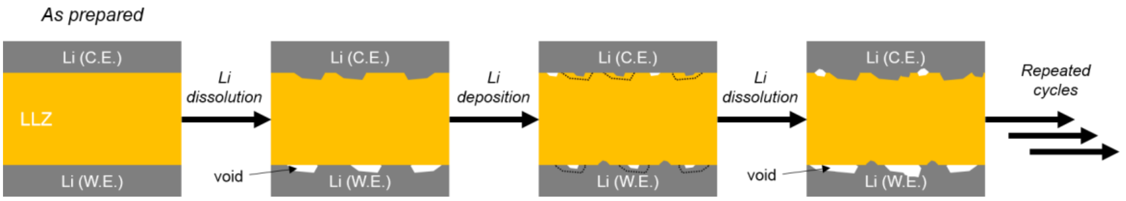

Fig. 8. Schematic illustration of the dynamic changes at the Li/LLZ interface during repeated Li dissolution/deposition cycles.

	R_{LLZ} / ohm	C_{LLZ} / F *	R_{int} / ohm	C_{int} / F *
Before cycle test	2227	1.35×10^{-10}	2106	2.77×10^{-9}
After 1st dissolution	2234	1.34×10^{-10}	3688	3.38×10^{-9}
After 1st deposition	2274	1.33×10^{-10}	2105	2.83×10^{-9}
After 5th dissolution	2249	1.33×10^{-10}	5042	3.79×10^{-9}
After 5th deposition	2252	1.34×10^{-10}	2516	2.81×10^{-9}

* Capacitance was calculated based on the equation: $C = T_{\mathrm{CPE}}^{1/p} \times R^{(1-p)/p}$, where T_{CPE} and p are the constant phase element (CPE) constant and the CPE index, respectively .

Table 1. Fitting parameters of a Li (W.E.)/Li (R.E.)/LLZ/Li (C.E.) three-electrode cell obtained before and during a galvanostatic cycle test at 50 μA/cm^2. The equivalent circuit and Nyquist plots were shown in Fig. 3.

3.4. Conclusion

In the present study, the three-electrode AC impedance technique was employed in an attempt to trace the dynamic changes in the charge transfer resistance at the Li/LLZ interface during Li dissolution and deposition. R_{int} increased and decreased during Li dissolution and deposition, respectively, and the increase during dissolution was not completely offset during the subsequent deposition process. Importantly, R_{int} was almost constant when Li deposition proceeded without prior Li dissolution, which suggests that the formation of voids at the Li/LLZ interface during Li dissolution is a critical factor that influences R_{int}. Based on the results obtained through the present work, we strongly encourage the development of a strategy to prevent the formation of voids at the Li/LLZ interface, particularly during Li dissolution, toward the real application of a Li metal anode in all-solid-state secondary batteries.

References

[1] M. Botros, R. Djenadic, O. Clemens, M. Möller, H. Hahn, *J. Power Sources*, **2016**, *309*, 108.

[2] R.H. Basappa, T. Ito, H. Yamada, *J. Electrochem. Soc*., **2017**, *164*, A666.

[3] F. Yonemoto, A. Nishimura, M. Motoyama, N. Tsuchimine, S. Kobayashi, Y. Iriyama, *J. Power Sources*, **2017**, *343*, 207.

[4] C. Wang, Y. Gong, B. Liu, K. Fu, Y. Yao, E. Hitz, Y. Li, J. Dai, S. Xu, W. Luo, E.D. Wachsman, L. Hu, *Nano Lett*., **2017**, *17*, 565.

[5] M. Kotobuki, K. Kanamura, Y. Sato, T. Yoshida, *J. Power Sources*, **2011**, *196*, 7750.

[6] M. Shoji, H. Munakata, K. Kanamura, *Front. Energy Res*., **2016**, *4*, 32.

[7] L. Cheng, E.J. Crumlin, W. Chen, R. Qiao, H. Hou, S.F. Lux, V. Zorba, R. Russo, R. Kostecki, Z. Liu, K. Persson, W. Yang, J. Cabana, T. Richardson, G. Chen, M. Doeff, *Phys. Chem. Chem. Phys*., **2014**, *16*, 18294.

[8] R. Murugan, V. Thangadurai, W. Weppner, *Angew. Chem. Int. Ed*., **2007**, *46*, 7778.

[9] H. Buschmann, S. Berendts, B. Mogwitz, J. Janek, *J. Power Sources*, **2012**, *206*, 236.

[10] L. Cheng, W. Chen, M. Kunz, K. Persson, N. Tamura, G. Chen, M. Doeff, *ACS Appl. Mater. Interfaces*, **2015**, *7*, 2073.

[11] E. Rangasamy, J. Wolfenstine, J. Sakamoto, *Solid State Ionics*, **2012**, *206*, 28.

[12] T.R. Jow, C.C. Liang, *J. Electrochem. Soc*., **1983**, *130*, 737.

[13] T.R. Jow, C.C. Liang, *Solid State Ionics*, **1983**, *9–10*, 695.

[14] J. Janek, *Solid State Ionics*, **2000**, *131*, 129.

[15] W.D. Richards, L.J. Miara, Y. Wang, J.C. Kim, G. Ceder, *Chem. Mater*., **2016**, *28*, 266.

[16] Y. Zhu, X. He, Y. Mo, *ACS Appl. Mater. Interfaces*, **2015**, *7*, 23685.

[17] K. Kerman, A. Luntz, V. Viswanathan, Y.-M. Chiang, Z. Chen, *J. Electrochem. Soc*., **2017**, *164*, A1731.

[18] A.C. Luntz, J. Voss, K. Reuter, *J. Phys. Chem. Lett.*, **2015**, *6*, 4599.

[19] S. Ramakumar, C. Deviannapoorani, L. Dhivya, L.S. Shankar, R. Murugan, *Prog. Mater. Sci.*, **2017**, *88*, 325.

[20] C. Ma, Y. Cheng, K. Yin, J. Luo, A. Sharafi, J. Sakamoto, J. Li, K.L. More, N.J. Dudney, M. Chi, *Nano Lett.*, **2016**, *16*, 7030.

[21] F. Han, Y. Zhu, X. He, Y. Mo, C. Wang, *Adv. Energy Mater.*, **2016**, *6*, 1501590.

[22] M. Nakayama, M. Kotobuki, H. Munakata, M. Nogami, K. Kanamura, *Phys. Chem. Chem. Phys.*, **2014**, *14*, 10008.

[23] B. Scharifker, G. Hills, *Electrochim. Acta*, **1983**, *28*, 879.

[24] A. Pei, G. Zheng, F. Shi, Y. Li, Y. Cui, *Nano Lett.*, **2017**, *17*, 1132.

[25] D. Grujicic, B. Pesic, *Electrochim. Acta*, **2002**, *47*, 2901.

[26] B. Im, S. Kim, *Electrochim. Acta*, **2014**, *130*, 52.

[27] A. Radisic, P.-M. Vereecken, P.-C. Searson, F.-M. Ross, *Surf. Sci.*, **2006**, *600*, 1817.

Chapter 4

Control of charge transfer resistance at Li/solid electrolyte interfaces during Li deposition-dissolution reactions

4.1. Introduction

As described in chapter 1, high Li/LLZ interfacial resistance (R_{int}) is one of the crucial problems to be solved for the commercialization of Li metal secondary batteries using LLZ as a electrolyte. In recent years, several kinds of a metal layer which can form alloy with Li have been introduced at the interface as a buffer layer to reduce R_{int} [1-7]. The introduction of these Li-alloy layers is effective to decrease R_{int}, and the improvement of Li/LLZ interfacial contact through the alloying of Li with the inserted second metal is suggested to be the origin of the decreased resistance. However, there is still limited information regarding the functions of the buffer layer during Li deposition and dissolution reactions and their dynamic change with the progress of the cycle.

As described in chapter 3, the author succeeded in individually tracing the dynamic change in R_{int} during Li deposition and dissolution reactions through the use of the three-electrode alternative current (AC) impedance technique. It was revealed that the increase in R_{int} during Li dissolution, associated with the formation of voids at the interface, is a critical factor influencing R_{int}. Therefore, in the present work, the author attempted to examine the functions of the introduced Au layer, which can form alloys with Li, during Li deposition-dissolution reactions by applying the established three-electrode impedance method to a Li/Au-deposited LLZ interface.

4.2. Experimental

4.2.1. Preparation of LLZ powder and Au or Li deposited-LLZ pellets

The preparation of LLZ powder and pellets were conducted by the same process described in the experimental section in chapter 3. After the surface of the pellet was polished with emery paper (#4000) in an argon-filled glove box, Au metal layer (3 mm diameter) was deposited on both sides of the pellet by sputtering (SC-701MkII, Sanyu Electron Co., Ltd.) at the flowing current of 8 mA for 10 min. Scanning electron microscopic (SEM) and energy dispersive X-ray spectroscopic (EDS) analysis for the Au-deposited LLZ demonstrated that the thickness of Au layer deposited on the LLZ is around 80 nm (Fig. 1). About 5 μm-thickness of Li metal layer (5 mm diameter) was also deposited on both sides of the pellet by vacuum evaporation, using the homemade equipment in Rechargeable Battery Materials Group in National Institute for Materials Science.

4.2.2. Characterization

SEM (JSM-7800F, JEOL) was used to observe the cross-section of a LLZ pellet or a Li-LLZ composite. EDS (X-Max^N, Oxford) equipped with the SEM was also used to conduct elemental analysis. Cross-section polisher (CP; IB-09020CP, JEOL) was used to prepare a sample for EDS analysis. The sample was transferred from the glove box to the SEM or CP instrument in a sealed vessel filled with argon gas. Measurements were conducted at an acceleration voltage of 5 kV (for SEM observation) or 15 kV (for EDS analysis) under an ambient pressure of less than 10^{-4} Pa.

4.2.3. Cell assembly and electrochemical measurements

A three-electrode cell was assembled in the same configuration of electrodes as described in the experimental section in chapter 3. The diameter of a working electrode and a counter electrode was increased to 5 mm when Li-deposited LLZ was used. The cell pressure was controlled to ca. 0.7 MPa or ca. 7 MPa by using two kinds of springs. After the cell assembly, electrochemical measurement was conducted according to the scheme shown in Scheme 1. Galvanostatic Li dissolution/deposition and AC impedance measurements were conducted at 25 °C using a potentio-galvanostat equipped with an impedance analyzer (VMP3, BioLogic Science Instruments). AC impedance spectra were collected with an amplitude of 15 mV in the frequency range from 1 MHz to 100 mHz. In a one-hour cycle test, AC impedance measurement was conducted every 10 min during Li dissolution or deposition reaction.

4.3. Results and discussion

The open circuit potential and R_{int} as a function of cell storage time were examined to obtain information about the composition of the buffer layer. When the measurement was started, the W.E. potential was around 40 mV (vs. Li/Li$^+$). Then it decreased to around 0 V in less than one hour, and kept almost the same in the following 20 h (Fig. 2(a)). R_{int} also declined as a function of the time especially in the early stage of the measurement, in which the W.E. drastically decreased (Figs. 2(a) and (b)). In EDS mapping of the W.E./LLZ interface, Au layer clearly appeared at the interface for the image obtained 1 min-after the cell assembly (Fig. 3(a) and 4(a)), whereas the Au layer could not be observed when the cell storage time was extended to 1 h (Fig. 3(b) and 4(b)). These results indicate that the interface preferable for Li$^+$ transfer was formed through the diffusion of Au metal into the bulk of a Li metal electrode when Li foil was attached on a deposited-Au layer under the cell pressure. After the open circuit potential and R_{int} became stable after one day, the measurement was stopped and the cell was subjected to the heat treatment at 100 °C for 4 h. R_{int} measured after the heat treatment was about half the value obtained in the end of the one day-measurement, which is suggested to be originated from the improved physical contact at the W.E./LLZ interface due to the increased softness of Li metal during the heat treatment. Local distribution of Au at the interface was not detected after the heat treatment, that is, the concentration of Au at the interface decreased below the detection limit (1 atom%) (Fig. 3(c) and 4(c)). Although the diffusion of Au into Li was observed, the deposited Au metal is supposed to remain at the interface at the concentration below 1 atom%. Indeed, the atomic ratio of Au/Li was calculated to be about 0.02% based on the thickness of Au and Li initially introduced. According to the Li-Au phase diagram, Li metal dissolves less than 0.5 atom% of Au and forms a solid solution at room temperature. Thus it is reasonable that Li-Au solid solution with Au concentration of < 0.5 atom% should be formed in the whole electrode (Fig. 5). The influence of the properties of the Li-Au solid solution on the electrochemical performance will be discussed later.

The dynamic change of R_{int} during Li dissolution and deposition reactions was next investigated. Fig. 6 shows representative Nyquist plots obtained before and during the cycle test. Figs. 7(a) and (b) show the time courses of the W.E. potential and R_{int} obtained for a cell using a LLZ and a Au-deposited LLZ, respectively. R_{int} before the cycle test was decreased from 165 Ω cm^2 to 95 Ω cm^2 by depositing Au. With respect to the cell without Au deposition, R_{int} respectively increased and decreased during Li dissolution and deposition as described in chapter 3. The cell with Au deposition exhibited qualitatively the same R_{int} change; however, the degree of R_{int} change was suppressed from $\Delta 30$ Ω cm^2 to $\Delta 10$ Ω cm^2. In addition, the increment of R_{int} with increasing the cycle number was also inhibited by depositing Au. As described in chapter 3, the increase in R_{int} during Li dissolution can be associated with the formation and growth of voids at the interface [7-13]. Thus it was suggested that the formation and growth of voids were mitigated by the insertion of a Au buffer layer.

Now the next question is the origin of the decrease in R_{int}, namely the suppression of voids formation and growth, during the cycles when a Au buffer layer is introduced. R_{int} is, in general, determined by two factors: electrical contact area at the interface and the charge-transfer resistance per unit area of the contact region. To investigate the contribution from the former factor, Li instead of Au was deposited on both sides of a LLZ pellet because the electrode fabrication by a deposition method is known to be effective to increase the electrode/substrate (e.g. solid electrolyte) interfacial contact area [9]. Then the 1 h Li dissolution-deposition cycle test was conducted. Representative Nyquist plots obtained before and during the cycle test, and the time courses of the W.E. potential and R_{int} during the cycle test were shown in Fig. 8. As expected, R_{int} before cycle test was decreased from 165 Ω cm^2 to 30 Ω cm^2, and its change during the cycle was also suppressed from Δ30 Ω cm^2 to Δ5 Ω cm^2 by inserting the Li metal buffer layer (please compare Figs. 6(a) and 7(a) vs. Fig. 8). It should be noted that these tendencies were also observed when comparing the Li-deposited case (Fig. 8) with the Au-deposited one (Figs. 6(b) and 7(b)) although the difference became smaller (R_{int} before the cycle: 95 Ω cm^2 → 30 Ω cm^2 / R_{int} change during the cycle: Δ10 Ω cm^2 → Δ5 Ω cm^2). The significance of this difference is still controversial because both the affinity for LLZ and the employed deposition method are different between Au and Li. However, it can be said from these data that the increase in the W.E./LLZ interfacial contact area by inserting Au using the deposition method is one dominant origin of the decreased R_{int} (Fig. 2, 6 and 7). The detailed mechanism is as follows (Fig. 9). Attaching Li foil on the deposited Au, which has more intimate contact with LLZ, results in the improved interfacial contact between a W.E. and LLZ via the reaction between Li and Au. Once the intimate contact is formed, the effective current density during the cycle also becomes smaller, resulting in the decrement of R_{int} through the suppression of voids formation.

At the same time, it is suggested from the results described below that the physicochemical properties of Li-Au solid solution as well as the quality of the interfacial contact affect R_{int} before and during the cycle. In Nyquist plots obtained for the cell with deposited Au (Fig. 6(b)), another semicircle was observed in the low frequency region (< 20 Hz), which can be related to electrochemical Li-Au alloying based on the consistency of the frequency range and the order of capacitance (~ 10^{-3} F) for that semicircle with those reported in previous studies [1, 5]. The resistance related to the Li-Au alloying ($R_{\text{Li-Au}}$) estimated using the equivalent circuit (the inset in Fig. 6) was plotted against the cycle time in Fig. 7(b). $R_{\text{Li-Au}}$ decreased during Li dissolution and increased during Li deposition, suggesting that the physicochemical properties of Li-Au solid solution (e.g. composition ratio) change associated with Li dissolution and deposition reactions.

Finally, the influence of the physicochemical properties of Li-Au solid solution on the electrochemical performance was examined. Since the applied pressure is known to be one of the crucial factors affecting the properties of solid solution, the same cycle test was conducted when the cell pressure was decreased to one tenth (0.7 MPa). Representative Nyquist plots were shown in Fig. 10. $R_{\text{Li-Au}}$ was observed, but its value before the cycle and after Li dissolution were much higher than those obtained under the higher cell pressure (7 MPa). The time course of the W.E. potential and R_{int} was shown in Fig. 11. Both the W.E. potential and R_{int} exhibited the higher value during the first Li dissolution and in the end of Li dissolution for the following cycles. When the duration of Li dissolution and deposition was gradually extended, the W.E. potential and R_{int} started to increase drastically during dissolution when the dissolution period approached that for the preceding Li deposition (Fig. 12). These results demonstrated that only the Li metal deposited in the preceding process can be dissolved with the lower overpotential and R_{int}. Importantly, these phenomena derived from the decreased cell pressure was specific to the cell using Au-deposited LLZ, indicating the physicochemical properties of Li-Au solid solution is also an important factor determining the electrochemical performance. Therefore, it is possible that the formation of Li-Au solid solution is another key factor of the decrease in R_{int} change during the cycle. The detailed mechanism is still under investigation; however, three origins can be proposed at present: (1) the improved wettability of the Li electrode against LLZ by dissolving Au [1, 14], (2) the increased number of Li deposition sites by the formation of the three-phase boundary among Li, Au and LLZ [15] and (3) the change in the mechanical properties (e.g. stiffness) of the electrode/LLZ interface by dissolving Au, which is analogous to that in the stiffness of steel by controlling the carbon content up to 5%.

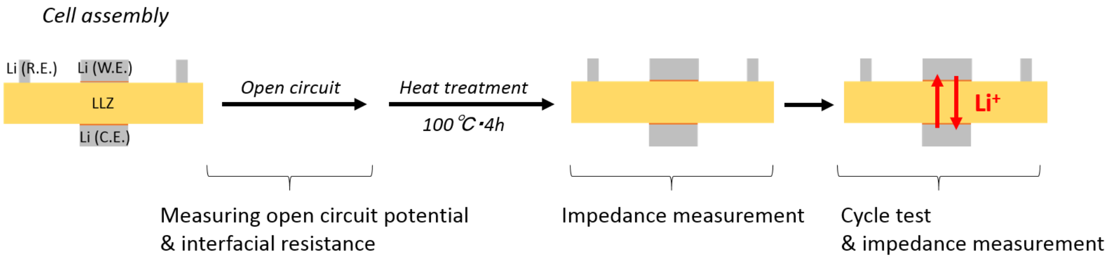

Scheme 1. The protocol of electrochemical measurements for the cell using Au-deposited LLZ.

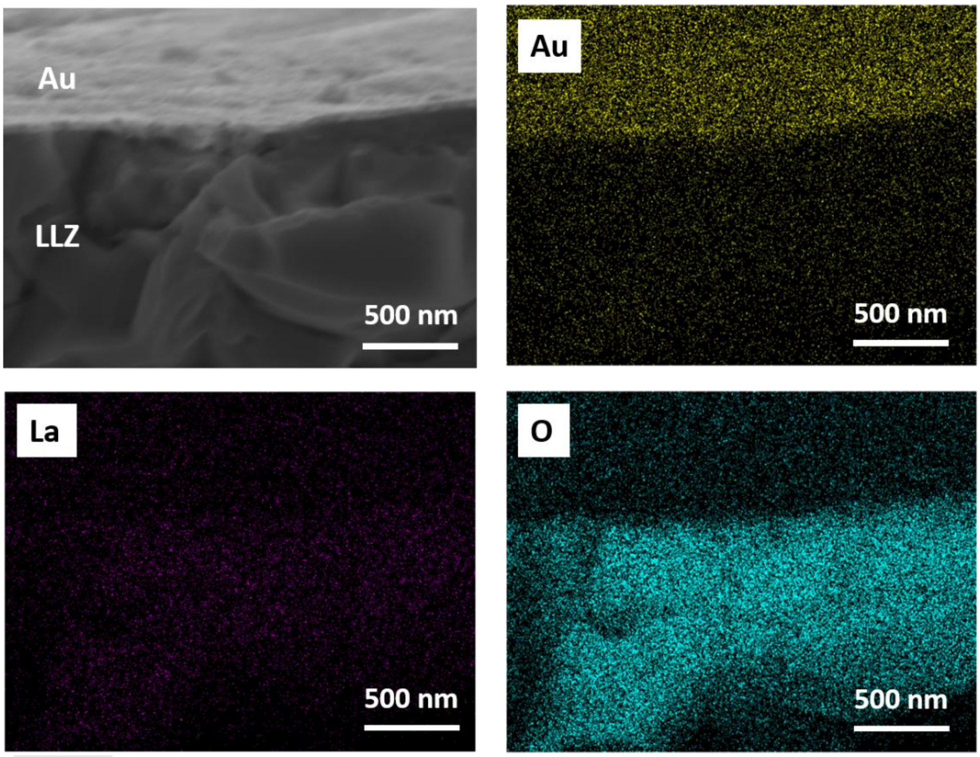

Fig. 1. SEM images and corresponding EDS mapping of Au, La and O for the cross section of Au-deposited LLZ.

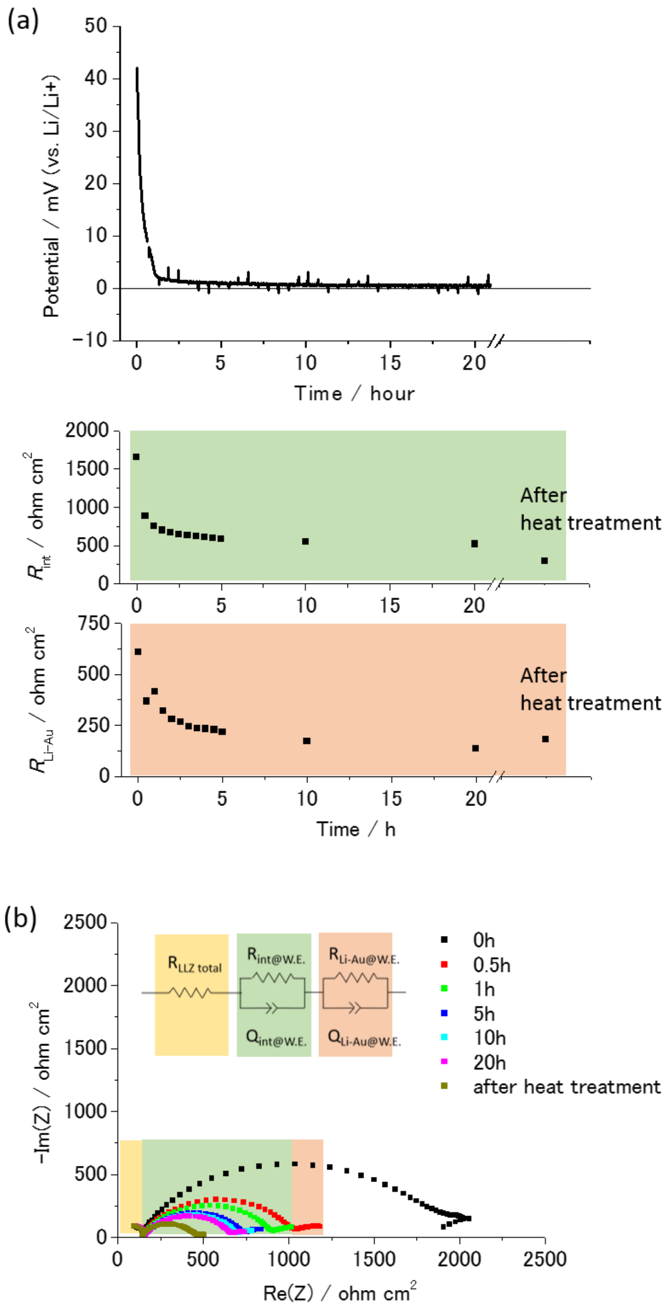

Fig. 2. (a) The open-circuit potential of a Li(W.E.)/Li(R.E.)/Au-deposited LLZ/Li(C.E.) cell under 7 MPa pressure, and the value of R_{int} and $R_{\text{Li-Au}}$ as a function of time when the measurement was started just after the cell assembly without heat treatment. (b) Nyquist plots for the same cell during the measurement of the open-circuit potential and after the subsequent heat treatment.

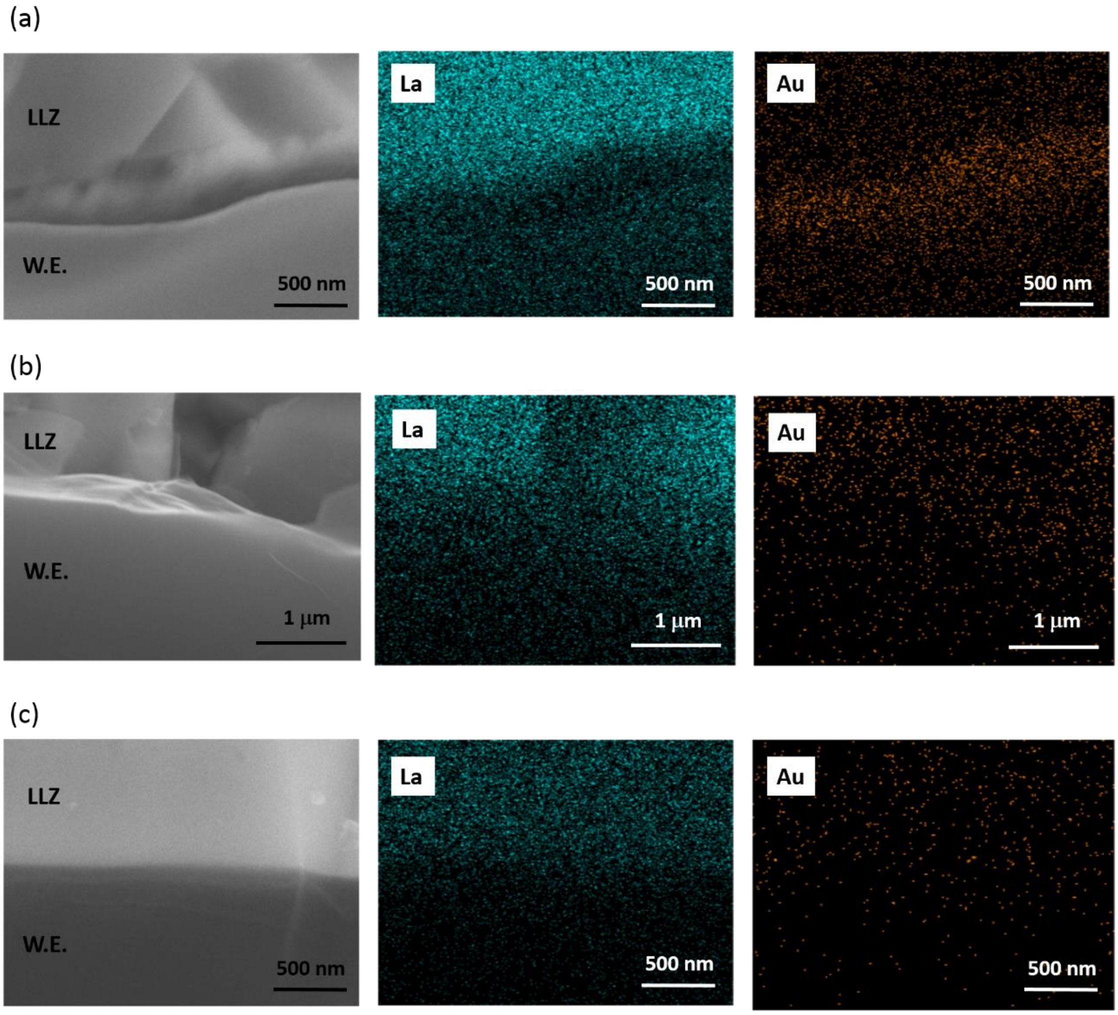

Fig. 3. SEM images and corresponding EDS mapping of La and Au for the W.E./Au-deposited LLZ interfaces fabricated under 7 MPa pressure obtained (a) 1 min-after the cell assembly without heat treatment, (b) 1 h-after the cell assembly without heat treatment and (c) a few days-after the cell assembly with heat treatment.

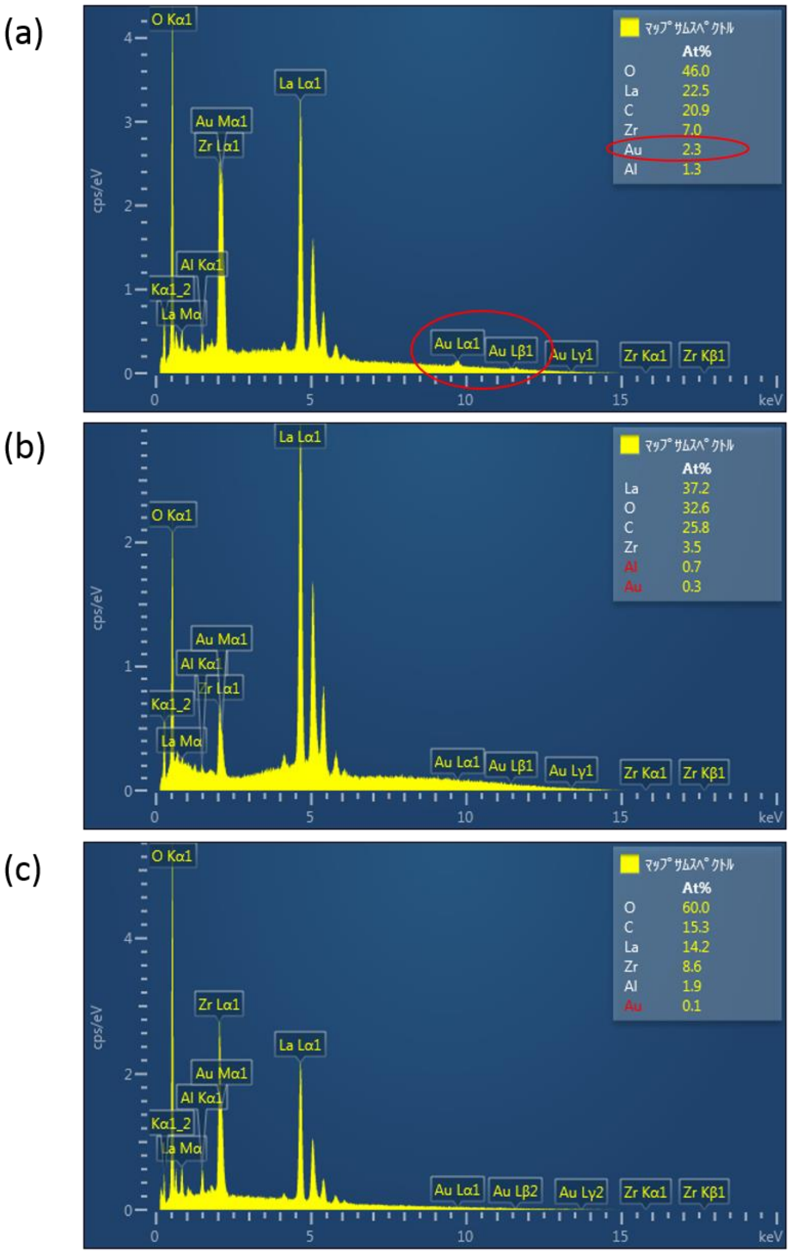

Fig. 4. EDS spectra and the corresponding atomic composition obtained for the SEM images shown in Fig. 3. (a)-(c) corresponds to (a)-(c) in Fig. 3.

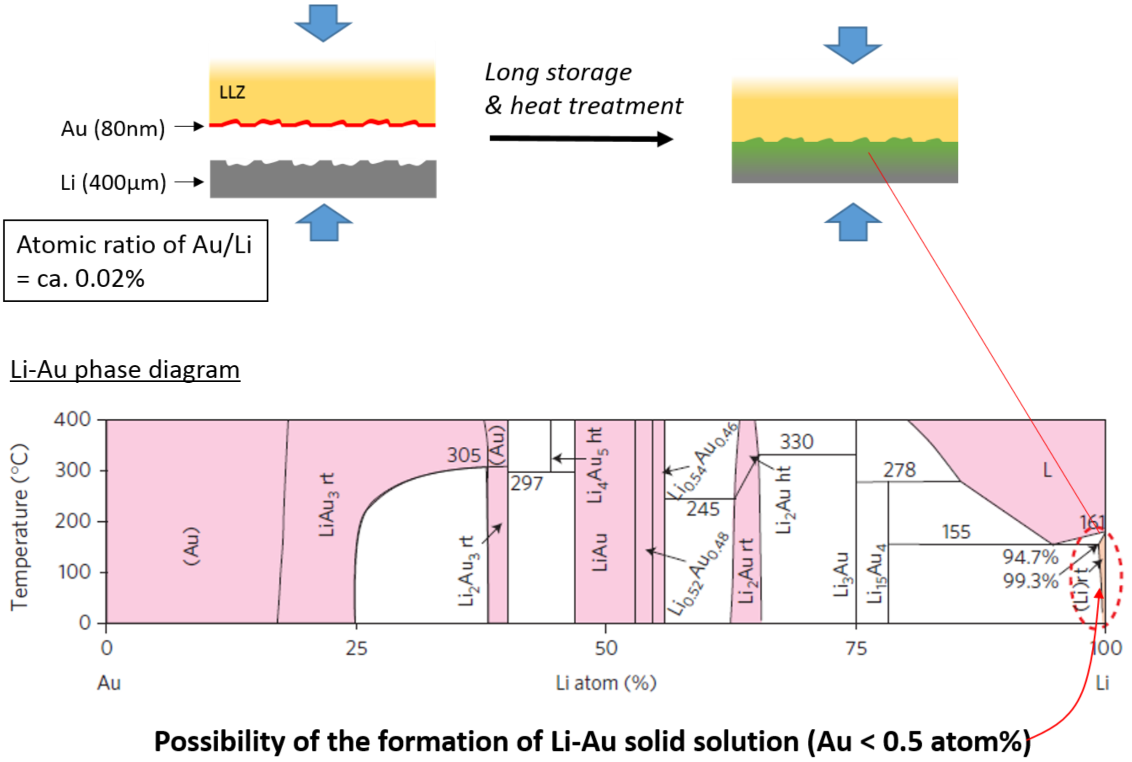

Fig. 5. Schematic illustration of the formation of Li-Au solid solution. The Li-Au phase diagram was adapted by permission from ref. 16, Copyright 2016, Nature.

(a) w/o Au (cell pressure: 7 MPa)

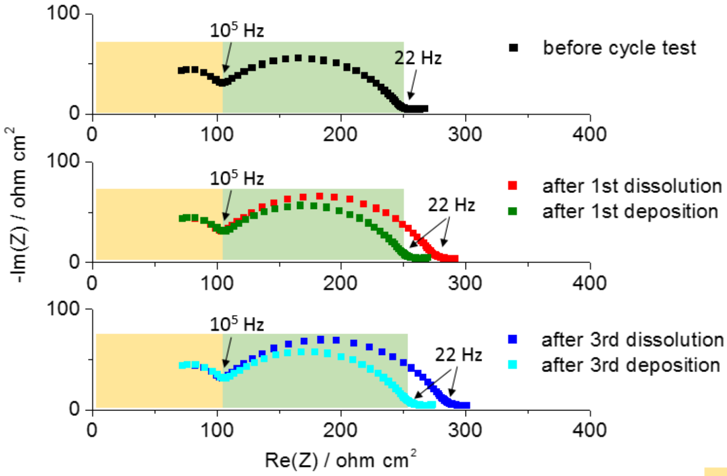

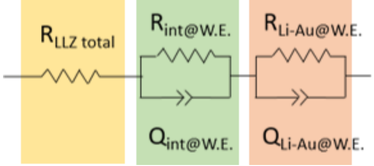

(b) w Au (cell pressure: 7 MPa)

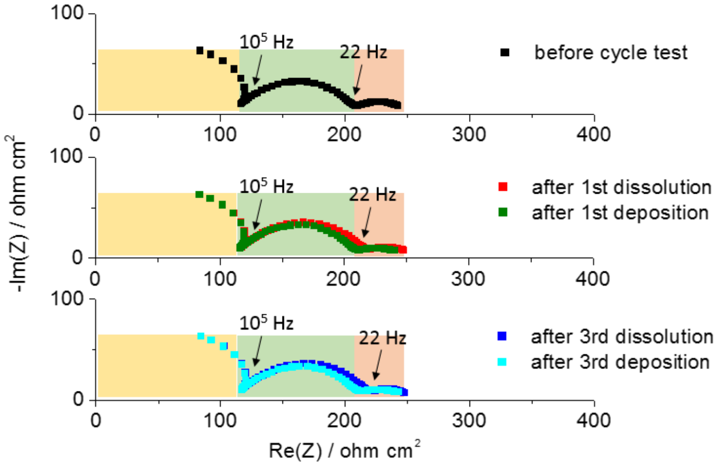

Fig. 6. Nyquist plots for (a) Li(W.E.)/Li(R.E.)/LLZ/Li(C.E.) and (b) Li(W.E.)/Li(R.E.)/Au-deposited LLZ/Li(C.E.) three-electrode cell under 7 MPa pressure obtained before and during a galvanostatic cycle test at 50 μA/cm^2. The equivalent circuit used for the estimation of R_{int} and $R_{\mathrm{Li\text{-}Au}}$ was also shown.

(a) w/o Au (cell pressure: 7 MPa)

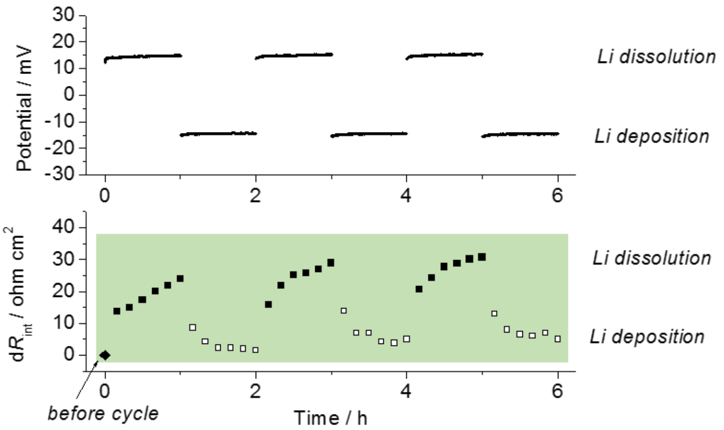

(b) w Au (cell pressure: 7 MPa)

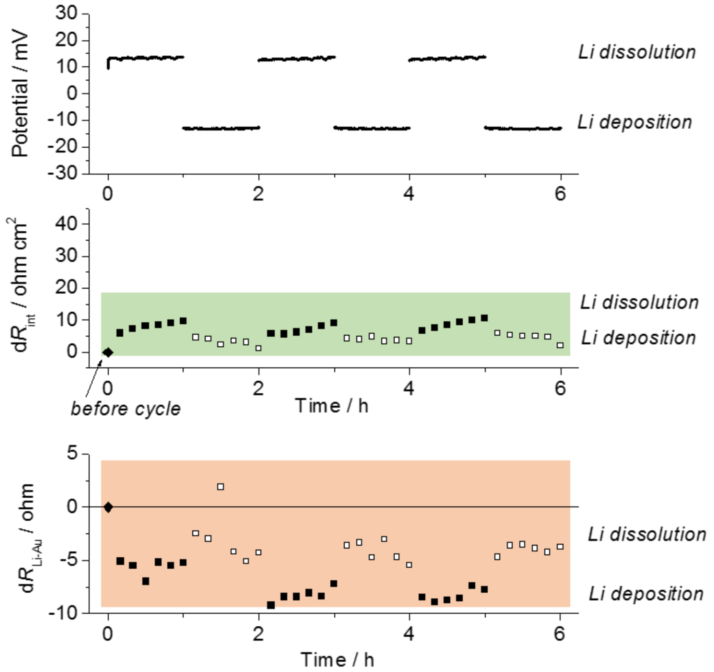

Fig. 7. W.E. potential and the change in R_{int} and $R_{\mathrm{Li\text{-}Au}}$ as a function of time when Li metal corresponding to the thickness of 250 nm was dissolved and deposited at 50 μA/cm^2 for (a) Li(W.E.)/Li(R.E.)/LLZ/Li(C.E.) and (b) Li(W.E.)/Li(R.E.)/Au-deposited LLZ/Li(C.E.) cells under 7 MPa pressure. The resistance measured during Li deposition and dissolution are plotted as open and closed squares, respectively.

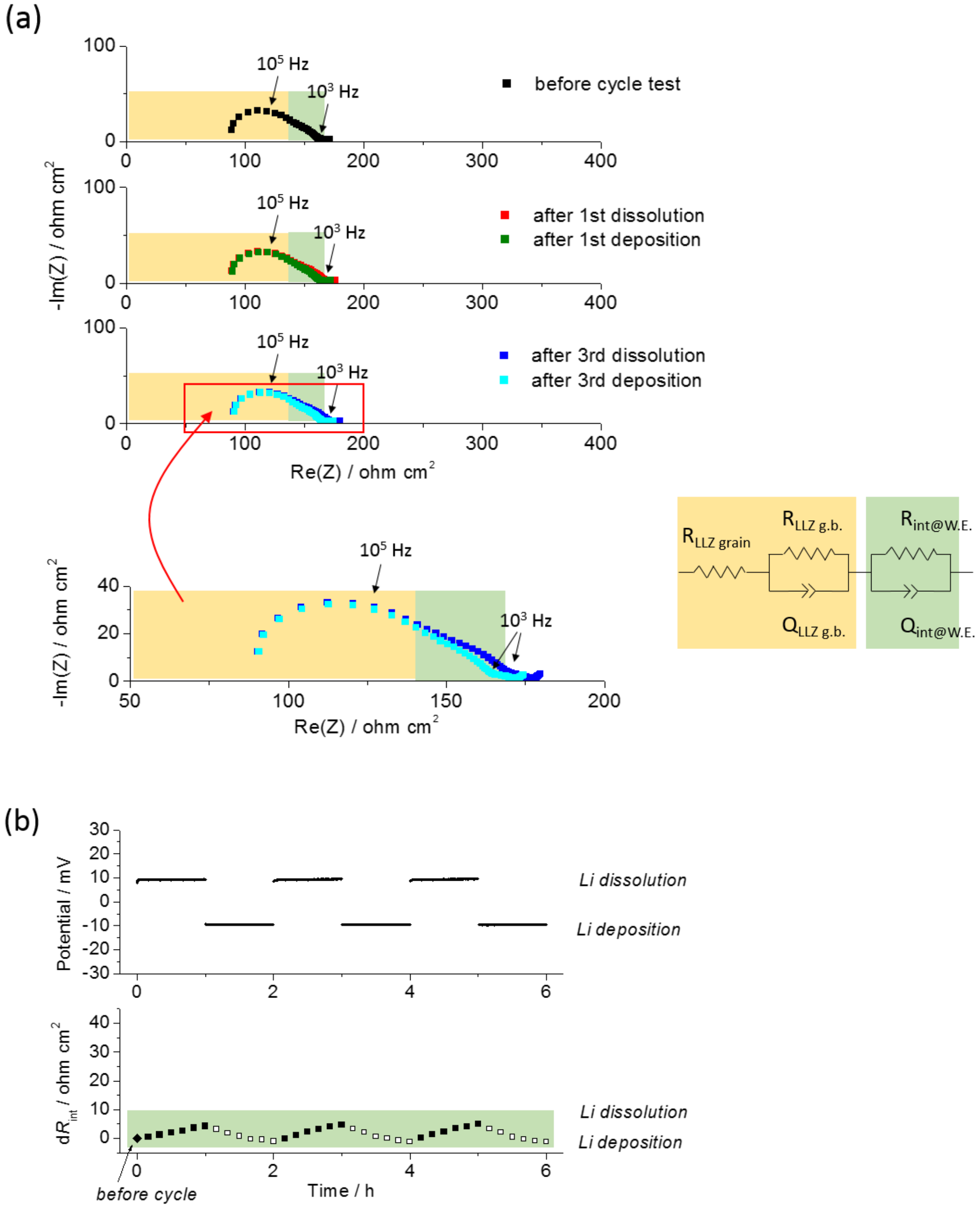

Fig. 8. (a) Nyquist plots for a Li (W.E.)/Li(R.E.)/Li-deposited LLZ/Li(C.E.) three-electrode cell under 7 MPa pressure obtained before and during a galvanostatic cycle test at 50 μA/cm^2. The equivalent circuit was also shown. (b) The time courses of the W.E. potential and R_{int} change for the same cell during the cycle test. The resistance measured during Li deposition and dissolution are plotted as open and closed squares, respectively.

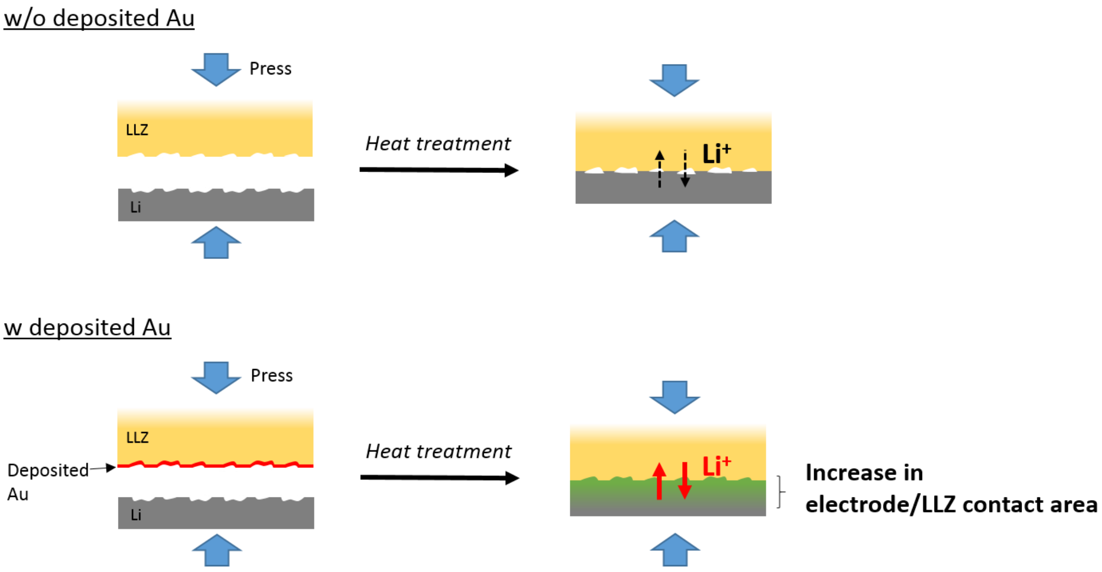

Fig. 9. Schematic illustration of Li deposition-dissolution reactions proceeded at Li/LLZ and Li/Au-deposited LLZ interfaces.

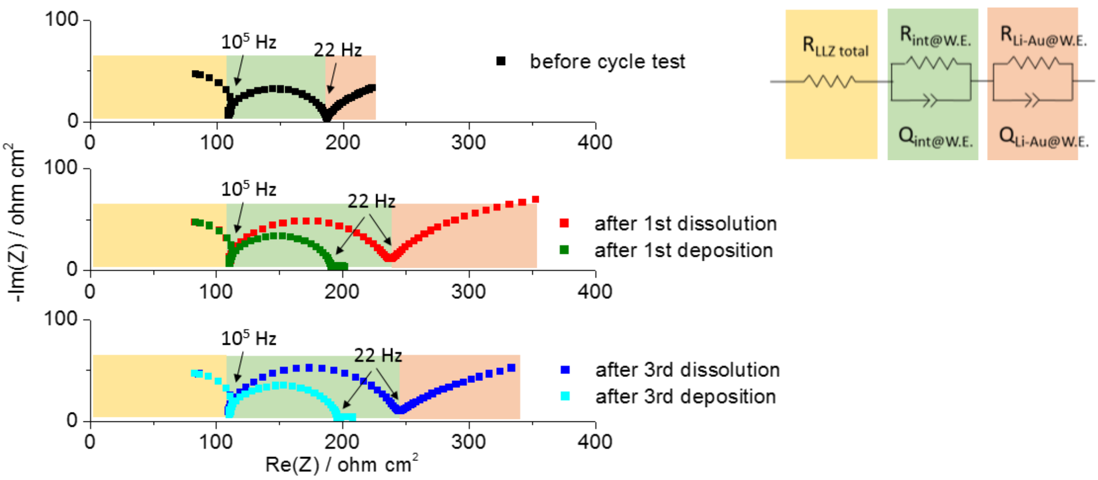

Fig. 10. Nyquist plots for a Li(W.E.)/Li(R.E.)/Au-deposited LLZ/Li(C.E.) cell under 0.7 MPa pressure obtained before and during a galvanostatic cycle test at 50 μA/cm^2. The equivalent circuit was also shown.

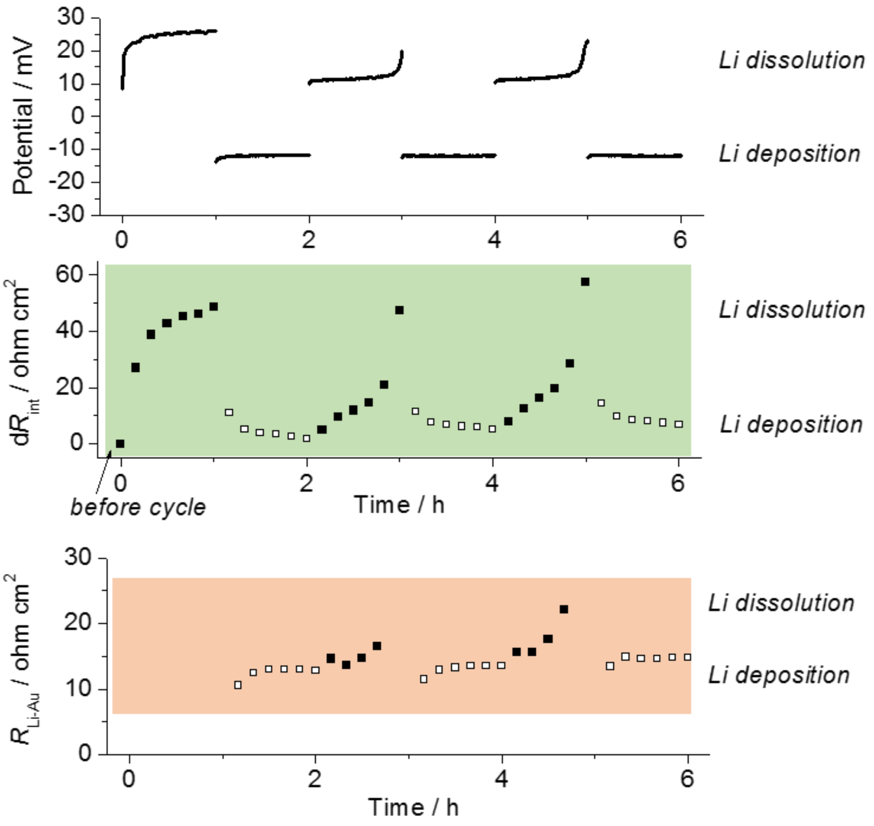

Fig. 11. The time courses of the W.E. potential, R_{int} change and $R_{\mathrm{Li\text{-}Au}}$ for a Li(W.E.)/Li(R.E.)/Au-deposited LLZ/Li(C.E.) cell under 0.7 MPa pressure during a galvanostatic cycle test at 50 μA/cm^2. The resistance measured during Li deposition and dissolution are plotted as open and closed squares, respectively.

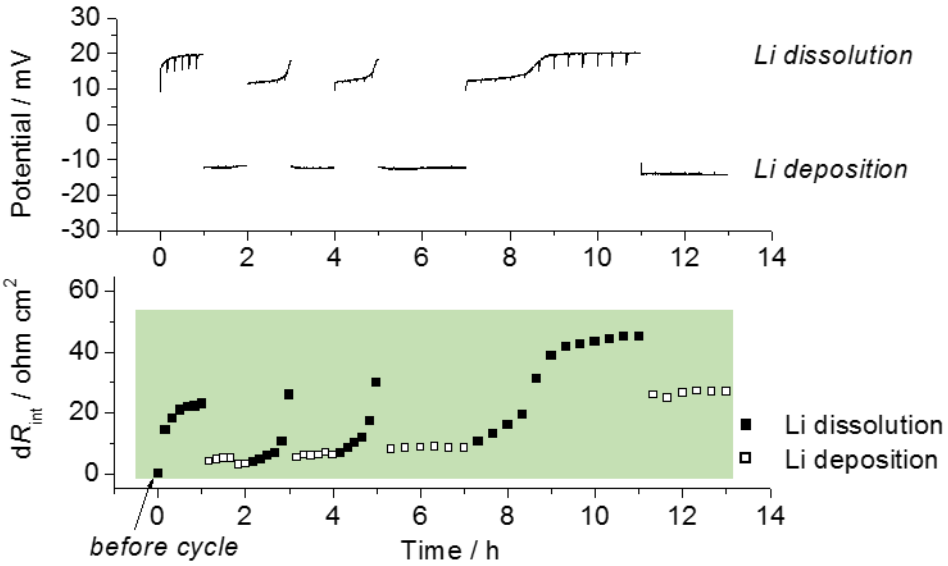

Fig. 12. W.E. potential and the change in R_{int} as a function of time when the amount of Li metal dissolved and deposited at 50 μA/cm^2 was gradually increased for a Li(W.E.)/Li(R.E.)/Au-sputtered LLZ/Li(C.E.) cell under 0.7 MPa pressure. The resistance measured during Li deposition and dissolution are plotted as open and closed squares, respectively.

4.4. Conclusion

In the present study, the function of a Au layer introduced at a Li/LLZ interface during Li deposition-dissolution reactions was investigated by applying the three-electrode AC impedance technique established in chapter 3. R_{int} decreased through the diffusion of deposited Au into Li after the cell assembly, and hence the interface preferable for Li-ion transfer was formed. R_{int} for the cell with deposited Au increased and decreased respectively during Li dissolution and deposition as observed in chapter 3. However, the degree of R_{int} change was suppressed to less than half. This result suggests that the formation and growth of voids were mitigated by introducing the Au buffer layer at the interface. Concerning the origin of the decreased resistance by inserting Au, two factors can be proposed. One is the increase in the interfacial contact area by introducing Au using a deposition method, which was supported by the fact that R_{int} decreased with a similar degree even when Li metal instead of Au metal was deposited at the interface prior to the cycle test. The other is related to the formation of Li-Au solid solution, which is suggested from the fact that the impedance related to electrochemical Li-Au alloying was observed and exhibited charge/discharge dependence. Based on the results obtained through this study, we stress the importance of considering the close correlation between the quality of interfacial contact and the physicochemical properties of the interface when the proper design of the interface is attempted.

References

[1] C.-L. Tsai, V. Roddatis, C. V. Chandran, Q. Ma, S. Uhlenbruck, M. Bram, P. Heitjans, O. Guillon, *ACS Appl. Mater. Interfaces*, **2016**, *8*, 10617.

[2] X. Han, Y. Gong, K. K. Fu, X. He, G. T. Hitz, J. Dai, A. Pearse, B. Liu, H. Wang, G. Rubloff, Y. Mo, V. Thangadurai, E. D. Wachsman, L. Hu, *Nat. Mater*., **2017**, *16*, 572.

[3] W. Luo, Y. Gong, Y. Zhu, K. K. Fu, J. Dai, S. D. Lacey, C. Wang, B. Liu, X. Han, Y. Mo, E. D. Wachsman, L. Hu, *J. Am. Chem. Soc*., **2016**, *138*, 12258.

[4] W. Luo, Y. Gong, Y. Zhu, Y. Li, Y. Yao, Y. Zhang, K. K. Fu, G. Pastel, C.-F. Lin, Y. Mo, E. D. Wachsman, L. Hu, *Adv. Mater*., **2017**, *29*, 1606042.

[5] J. Wakasugi, H. Munakata, K. Kanamura, *J. Electrochem. Soc*., **2017**, *164*, A1022.

[6] K. K. Fu, Y. Gong, B. Liu, Y. Zhu, S. Xu, Y. Yao, W. Luo, C. Wang, S. D. Lacey, J. Dai, Y. Chen, Y. Mo, E. Wachsman, L. Hu, *Sci. Adv*., **2017**, *3*, e1601659.

[7] C. Wang, Y. Gong, B. Liu, K. Fu, Y. Yao, E. Hitz, Y. Li, J. Dai, S. Xu, W. Luo, E. D. Wachsman, L. Hu, *Nano Lett*., **2017**, *17*, 565.

[8] M. Botros, R. Djenadic, O. Clemens, M. Möller, H. Hahn, *J. Power Sources*, **2016**, *309*, 108.

[9] R. H. Basappa, T. Ito, H. Yamada, *J. Electrochem. Soc*., **2017**, *164*, A666.

[10] F. Yonemoto, A. Nishimura, M. Motoyama, N. Tsuchimine, S. Kobayashi, Y. Iriyama, *J. Power Sources*, **2017**, *343*, 207.

[11] T. R. Jow, C. C. Liang, *J. Electrochem. Soc*., **1983**, *130*, 737.

[12] T. R. Jow, C. C. Liang, *Solid State Ionics*, **1983**, *9–10*, 695.

[13] J. Janek, *Solid State Ionics*, **2000**, *131*, 129.

[14] C. Wang, H. Xie, L. Zhang, Y. Gong, G. Pastel, J. Dai, B. Liu, E. D. Wachsman, L. Hu, *Adv. Energy Mater.*, **2017**, *7*, 1701963.

[15] A. Kato, A. Hayashi, M. Tatsumisago, *J. Power Sources*, **2016**, *309*, 27.

[16] K. Yan, Z. Lu, H.-W. Lee, F. Xiong, P.-C. Hsu, Y. Li, J. Zhao, S. Chu, Y. Cui, *Nat. Energy*, **2016**, *1*, 16010.

Chapter 5

Conclusion and Perspective

5.1. Conclusion

Li metal secondary batteries, in which Li metal is used as a negative electrode material, have attracted much attention because the utilization of Li metal enables the development of batteries with much higher energy density compared to that of conventional Li-ion batteries. For the real application of these batteries, there are several problems to be solved. The consumption of Li metal by the reactions with electrolyte is especially a crucial problem because it also induces other problems accelerating the cell deterioration such as the increase in Li/electrolyte interfacial resistance and the growth of Li dendrites under the non-uniformity of ionic flux. In this thesis, the author tackled this problem from two aspects. One is the formation of a good passivation layer at Li/electrolyte interfaces especially in the presence of air contaminants, and the other is the replacement of conventional organic electrolytes with inorganic solid-state electrolytes which are stable against Li metal.

In chapter 2, the author investigated the effects of contaminant water on reactions proceeded at negative and positive electrodes in Li-air batteries. In chapter 2-1, the author examined the effects of water concentration (C_{H2O}) on the coulombic efficiency (CE) of Li deposition/dissolution reactions in tetraglyme-based electrolytes. It was demonstrated that the CE increases from approximately 50% to 80% with increasing C_{H2O} to 1000 ppm, but decreases with further increase in C_{H2O}. XPS analyses of the formed Li deposits revealed that the increase in CE at C_{H2O} values of < 1000 ppm is associated with the increase in the composition ratio of Li_2O in the deposits. In contrast, the reduction of the CE at C_{H2O} > 1000 ppm is associated with the formation of resistive LiOH. In addition, SEM analysis of the deposits revealed that large Li-aggregates with the size of several tens of μm are formed when the C_{H2O} exceeds 1000 ppm. Taken together, these results indicate that optimized amount of water is beneficial for reversible Li deposition/dissolution reactions. Based on the results obtained in chapter 2-1, in chapter 2-2, the author also attempted to investigate the possibility of the utilization of water as the additive which facilitates the charge-discharge reactions at an air cathode. Efficient electrocatalysts for oxygen reduction reaction (ORR) in aqueous media constitute a group of materials which can promote the reactions at the cathode in the presence of water. Therefore, first, ORR electrocatalysts with high activity and stability were synthesized by heat treating a mixture of a Cu complex and reduced graphene oxides. The obtained catalyst exhibits the highest ORR performance, i.e., the smallest overpotential, among Cu-based catalysts. The catalyst also possesses high stability during 1000 cycles of cyclic voltammetry due to the anchoring of active Cu-sites into the graphene substrate. In the next step, the catalyst was employed as a cathode material in Li-air batteries. The air cathode maintains the performance even when several thousands ppm of water is added into the electrolyte. However, significant improvement of the charge-discharge performance is not observed in the presence of water. Efficient breakage and reformation of the double bond of molecular oxygen is known to be the crucial process for the effective use of water on the cathode. Thus the more sophisticated design of the electrocatalysts such as the introduction of the catalytic sites composed of multinuclear metal centers will be required.

In chapter 3, the author investigated dynamic changes in the charge-transfer resistance at a Li/$Li_7La_3Zr_2O_{12}$ (LLZ) solid electrolyte interface during Li dissolution-deposition cycles with an alternative current (AC) impedance technique in a three-electrode system. Adoption of the three-electrode system enabled us to examine independently one interface between a working electrode and electrolyte from the other interface between a counter electrode and the electrolyte. It was revealed that the interfacial resistance respectively increases and decreases during Li dissolution and deposition. The resistance does not return to the initial value after one cycle of Li dissolution and deposition, which indicates that the change in resistance during dissolution is larger than that during deposition. Furthermore, the resistance is almost constant when Li deposition proceeds without prior Li dissolution. The respective increase and decrease in the interfacial resistance during Li dissolution and deposition is most likely due to the formation and disappearance of voids at the Li/LLZ interface, and the voids formation during Li dissolution is suggested to be a critical factor that influences the interfacial resistance.

In chapter 4, the author examined the function of a Au layer introduced at the Li/LLZ interface by applying the three-electrode AC impedance technique established in chapter 3. It was demonstrated that the electrode/LLZ interfacial resistance decreases through the diffusion of deposited Au into Li after the cell assembly, and hence the interface preferable for Li-ion transfer is formed. The interfacial resistance for the cell with deposited Au exhibits qualitatively the same change during Li dissolution and deposition as for the cell without the buffer layer. However, the degree of the resistance change is suppressed to less than half. This result suggests that the formation and growth of voids are mitigated by introducing the Au buffer layer at the interface. Concerning the origin of the decreased resistance by inserting Au, two factors can be listed. One is the increase in the interfacial contact area by introducing Au using a deposition method. The interfacial resistance before the cycle test and its change during the cycle also decreases with a similar degree when Li instead of Au is deposited on LLZ during the cell assembly. The other factor is related to the formation of Li-Au solid solution. Considering the amount of Au and Li initially introduced and the Li-Au phase diagram, it is reasonable that the Li-Au solid solution containing less than 0.5 atom% of Au constitutes the electrode in a steady state. Indeed, the impedance related to Li-Au alloying is observed and exhibits charge/discharge dependence. Besides, the distinctive cell pressure dependence on the cycle performance associated with the resistance change is observed only when Au is introduced. These results suggest that the physicochemical properties of Li-Au solid solution (e.g. composition ratio) is another key factor determining the interfacial resistance and hence the battery performance. Knowledge obtained in this study also stress the importance of considering the close correlation between the quality of interfacial contact and the physicochemical properties of the interface when the proper design of the interface is attempted.

5.2. Perspective

In this thesis, the author demonstrated that the consumption of Li metal by side reactions with electrolyte is suppressed in the presence of optimized amount of water (~ 1000 ppm) in ether-based electrolytes and that it is almost completely prevented by using a solid electrolyte, $Li_7La_3Zr_2O_{12}$ (LLZ), with high stability against Li metal,. In addition, it was also revealed that the Li/LLZ interfacial resistance is decreased during repetitive cycles by making intimate contact between Li and LLZ by sputtering Li or metal which can form alloy with Li onto LLZ. However, preventing the growth of Li dendrites is also a crucial problem to be solved for the commercialization of Li metal secondary batteries. Herein, the author discussed the future prospects of Li metal secondary batteries, proposing the strategies to suppress Li dendritic growth.

As described in chapter 1, there are three principal problems to be solved for the employment of a Li metal electrode: the consumption of Li metal by side reactions with electrolyte, the increasing Li/electrolyte interfacial resistance during the cycle and the cell short-circuit derived from the growth of Li dendrites. Solving the first problem is considered to be the highest priority especially when batteries with much higher energy density and power density are required. In general, side reactions between Li metal and electrolytes increase the Li/electrolyte interfacial resistance. Then the increased interfacial resistance leads to the non-uniformity of Li-ion flux, and hence Li dendrites grow. Therefore reactions of Li metal with electrolytes should be considerably suppressed. With respect to this requirement, the use of solid-state Li-ion conductors instead of conventional organic electrolytes can be strongly recommended. This is because inorganic solid-state Li-ion conductors can be thermodynamically much more stable when contacting with Li metal compared to organic electrolytes or polymers. At present, LLZ employed in this thesis is the most promising solid electrolyte in terms of stability against Li metal.

When conventional organic electrolytes were replaced with inorganic solid-state Li-ion conductors, there still remains two problems: the high Li/electrolyte interfacial resistance and the cell short-circuit due to Li dendritic growth. The former is originated from the inherent rigidity of solid/solid interfaces relative to solid/liquid interfaces. In other words, the interfacial resistance becomes higher because the electrical contact between an electrode and a solid electrolyte cannot be effectively formed due to the roughness inevitably existing on the both surface. Recently, the Li/solid electrolyte interfacial resistance comparable to or even lower than the value for conventional Li/organic electrolyte interfaces (tens of Ω cm^2) has been obtained by tuning the chemical properties of the interface [1, 2]. However, this ideal interfacial state has to be maintained during prolonged cycles. The author demonstrated that the formation of voids at the interface during Li dissolution, which is a critical factor influencing the interfacial resistance, can be suppressed by lowering the effective current density. In addition, a Li metal electrode which has more intimate contact with the solid electrolyte was prepared by sputtering Li on the electrolyte. The current actually flowed per unit area should be decreased, and hence the interfacial resistance was drastically decreased during the cycle. Based on these considerations, the employment of a Li metal powder-solid electrolyte composite with much larger contact area as an anode active material is considered to be one promising solution. Besides, combination of physical and chemical approaches, e.g., making a Li alloy-solid electrolyte composite, can realize the ideal interface. Technical hurdles regarding the synthesis of these composites are expected to be overcome based on the related technology already established [3-10].

Contrary to the expectation, the cell short-circuit due to Li dendritic growth cannot be prevented even by the use of inorganic solid-state electrolytes. It is known that Li dendrites preferably grow along grain boundaries in the electrolyte or by infiltrating defects on the electrolyte surface. Several studies also reported that there is a critical current density above which

Li dendrites start to grow. However, the reliability of the critical current density calculated using the geometric electrode area is controversial. Li is likely to be dissolved from the intimate contact area locally existing at the interface and thus the effective current density should be considerably higher than the applied current density. Indeed, the author demonstrated that the three-electrode Li/Li/LLZ/Li cell short-circuited during Li deposition on the W.E. when the increased amount of Li was dissolved beforehand, associated with the larger increase of the interfacial resistance. This result indicates that Li dendrites preferably grow when Li-ion fluxes were more concentrated on the decreased interfacial area even under the same applied current density. Therefore the strategies to increase the effective contact area between Li and solid electrolyte described in the previous paragraph are also useful to suppress the growth of Li dendrites. In addition, for solving the problem related to Li dendrites, grain boundaries and crystalline inhomogeneity have to be eliminated by developing a novel synthesis method of a solid electrolyte, such as the synthesis of thin film of monocrystalline solid electrolyte [11-13].

References

[1] X. Han, Y. Gong, K. K. Fu, X. He, G. T. Hitz, J. Dai, A. Pearse, B. Liu, H. Wang, G. Rubloff, Y. Mo, V. Thangadurai, E. D. Wachsman, L. Hu, *Nat. Mater*., **2017**, *16*, 572.

[2] A. Sharafi, E. Kazyak, A. L. Davis, S. Yu, T. Thompson, D. J. Siegel, N. P. Dasgupta, J. Sakamoto, *Chem. Mater*., **2017**, *29*, 7961.

[3] J. Heine, S. Krüger, C. Hartnig, U. Wietelmann, M. Winter, P. Bieker, *Adv. Energy Mater*., **2014**, *4*, 1300815.

[4] Y.-S. Lee, J. H. Lee, J.-A. Choi, W. Y. Yoon, D.-W. Kim, *Adv. Funct. Mater*., **2013**, *23*, 1019.

[5] K. Fu, Y. Gong, G. T. Hitz, D. W. McOwen, Y. Li, S. Xu, Y. Wen, L. Zhang, C. Wang, G. Pastel, J. Dai, B. Liu, H. Xie, Y. Yao, E. D. Wachsman, L. Hu, *Energy Environ. Sci*., **2017**, *10*, 1568.

[6] J. Broek, S. Afyon, J. L. M. Rupp, *Adv. Energy Mater.*, **2016**, *6*, 1600736.

[7] J. Zheng, M. Tang, Y.-Y. Hu, *Angew. Chem. Int. Ed*., **2016**, *55*, 12538.

[8] H. Wakayama, H. Yonekura, Y. Kawai, *Chem. Mater*., **2016**, *28*, 4453.

[9] M. Kotobuki, K. Kanamura, Y. Sato, T. Yoshida, *J. Power Sources*, **2011**, *196*, 7750.

[10] T. Yang, Z. D. Gordon, Y. Li, C. K. Chan, *J. Phys. Chem. C*, **2015**, *119*, 14947.

[11] E. Kazyak, K.-H. Chen, K. N. Wood, A. L. Davis, T. Thompson, A. R. Bielinski, A. J. Sanchez, X. Wang, C. Wang, J. Sakamoto, N. P. Dasgupta, *Chem. Mater*., **2017**, *29*, 3785.

[12] Y. Suzuki, K. Kami, K. Watanabe, A. Watanabe, N. Saito, T. Ohnishi, K. Takada, R. Sudo, N. Imanishi, *Solid State Ionics*, **2015**, *278*, 172.

[13] E. Yi, W. Wang, J. Kieffer, R. M. Laine, *J. Power Sources*, **2017**, *352*, 156.

List of Publications

[1] K. Kamiya, **H. Koshikawa**, H. Kiuchi, Y. Harada, M. Oshima, K. Hashimoto, S. Nakanishi

"Iron–Nitrogen Coordination in Modified Graphene Catalyzes a Four-Electron-Transfer Oxygen Reduction Reaction" *ChemElectroChem*, **2014**, *1*, 877.

[2] **H. Koshikawa**, S. Nakanishi, K. Hashimoto, K. Kamiya

"Heat-treated 3, 5-diamino-1, 2, 4-triazole/graphene hybrid functions as an oxygen reduction electrocatalyst with high activity and stability" *Electrochim. Acta*, **2015**, *180*. 173.

[3] **H. Koshikawa**, S. Matsuda, K. Kamiya, Y. Kubo, K. Uosaki, K. Hashimoto, S. Nakanishi

"Effects of contaminant water on coulombic efficiency of lithium deposition/dissolution reactions in tetraglyme-based electrolytes" *J. Power Sources*, **2017**, *350*, 73.

[4] **H. Koshikawa**, S. Matsuda, K. Kamiya, M. Miyayama, Y. Kubo, K. Uosaki, K. Hashimoto, S. Nakanishi

"Dynamic changes of charge-transfer resistance at Li metal/$Li_7La_3Zr_2O_{12}$ interfaces during electrochemical Li dissolution/deposition cycles" *J. Power Sources*, **2018**, *376*, 147.

[5] **H. Koshikawa**, S. Matsuda, K. Kamiya, M. Miyayama, Y. Kubo, K. Uosaki, K. Hashimoto, S. Nakanishi

"Electrochemical impedance analysis of the function of the Au layer at Li metal/$Li_7La_3Zr_2O_{12}$ interfaces during Li dissolution/deposition cycles" *in preparation.*

Other Publication

[1] **<u>H. Koshikawa</u>**, S. Nakanishi, K. Hashimoto, K. Kamiya

“Catalytic methane combustion over iron/nitrogen-doped silicon carbide”

RSC Adv., **2016**, *6*, 85559.

Acknowledgement

This thesis deals with the studies conducted by the author under the supervision of Professor Dr. Kazuhito Hashimoto and Professor Dr. Masaru Miyayama at The University of Tokyo from April 2012 to March 2018.

First of all, the author would like to express his sincere thanks to Professor Dr. Kazuhito Hashimoto and Professor Dr. Masaru Miyayama for their invaluable guidance and constant encouragement throughout the course of this research.

The author is deeply grateful to Professor Dr. Shuji Nakanishi for his insightful advice and fruitful discussion.

Grateful acknowledgement is also made to Assistant Professor Dr. Kazuhide Kamiya and Dr. Shoichi Matsuda for their considerable knowledge regarding these studies as well as fruitful discussion.

It is a great pleasure to express the author's gratitude to Professor Dr. Kohei Uosaki and Dr. Yoshimi Kubo at National Institute for Materials Science (NIMS) for fruitful discussion about fundamental electrochemistry in secondary batteries.

The author really appreciate to Mr. Hideshi Ooka and Mr. Kazuyuki Iwase for their friendship.

The author is grateful to all the other members of Professor Hashimoto's laboratory as well as members of Professor Uosaki's group at NIMS for their kind help.

The financial support from JSPS, Research Fellowship of the Japan Society for the Promotion of Science for Young Scientists was indispensable, and the author sincerely appreciates.

Finally, the author would like to express his special thanks to my family and friends, who always supported and encouraged me to complete this work.

February, 2018

Hiroyuki Koshikawa